FATIGUE LIFE EVALUATION OF THE DIEFENBAKER BRIDGE USING STRUCTURAL HEALTH MONITORING

A Thesis Submitted to the
College of Graduate and Postdoctoral Studies
In Partial Fulfillment of the Requirements
For the Degree of Master of Science
In the Department of Civil, Geological, and Environmental Engineering
University of Saskatchewan
Saskatoon

By
Christopher James Morgan

PERMISSION TO USE

In presenting this thesis in partial fulfillment of the requirements for a Postgraduate degree from the University of Saskatchewan, I agree that the Libraries of this University may make it freely available for inspection. I further agree that permission for copying of this thesis/dissertation in any manner, in whole or in part, for scholarly purposes may be granted by the professor or professors who supervised my thesis/dissertation work or, in their absence, by the Head of the Department or the Dean of the College in which my thesis work was done. It is understood that any copying or publication or use of this thesis/dissertation or parts thereof for financial gain shall not be allowed without my written permission. It is also understood that due recognition shall be given to me and to the University of Saskatchewan in any scholarly use which may be made of any material in my thesis/dissertation.

Requests for permission to copy or to make other uses of materials in this thesis/dissertation in whole or part should be addressed to:

Head of the Department of Civil, Geological, and Environmental Engineering
57 Campus Drive
University of Saskatchewan
Saskatoon, Saskatchewan, S7N 5A9, Canada
OR
Dean
College of Graduate and Postdoctoral Studies
University of Saskatchewan
116 Thorvaldson Building, 110 Science Place
Saskatoon, Saskatchewan S7N 5C9 Canada

ABSTRACT

As bridge infrastructure continues to age, public agencies must reliably determine which structures can remain in service, and which structures require rehabilitation or replacement. Structural fatigue is a common problem for many aging steel structures and its evaluation is one that carries a high level of uncertainty. Structural health monitoring is one technique that infrastructure owners can employ to reduce this uncertainty, thereby allowing them to make the necessary investment with confidence.

Structural fatigue occurs when steel components of a bridge are subjected to stress cycles, with most details able to withstand only a limited number of cycles. The challenge in determining the remaining fatigue life of a bridge is the uncertainty in stress cycle history and in-situ structural behaviour. The Canadian Highway Bridge Design Code (CSA S6-14) does not address fatigue life evaluation directly, which creates an even larger challenge for engineers. Structural health monitoring is a technique that engineers and owners can use to reduce this uncertainty because it helps to reveal actual stress levels and cycle counts.

Structural health monitoring was used to inform the numerical determination of the remaining fatigue life of Diefenbaker Bridge's bracing connections to the girder webs. The Diefenbaker Bridge is located in Prince Albert, Saskatchewan, Canada. The 304 meter long, seven span bridge consists of two separate fracture critical superstructures, each comprising a cast-in-place concrete deck supported by two welded steel I-beams. The separate superstructures share a cast-in-place concrete substructure. Given the age of this bridge, and its history of frequent rehabilitation, an understanding of the remaining fatigue life was of critical importance to its owner since asset management plans depended on the outcome.

To perform the evaluation, the structure was instrumented with strain gauges, accelerometers, and a weather station. Data was collected for six months and was used to characterize in-situ bridge behaviour (i.e., lateral load distribution, degree of composite action, and dynamic load influence) and to evaluate the bridge's remaining fatigue life using various methods of fatigue life evaluation, including deterministic methods (including the method outlined in AASHTO), and a probabilistic method. Lastly, fatigue damage was characterized to determine what stress magnitudes contribute the most damage, and which connections are the most heavily loaded. In addition, fatigue damage was computed per girder on a daily and monthly basis.

This research demonstrated that costly improvements to the lateral bracing's connection to the girder webs on Diefenbaker Bridge are not required, and that, under the most conservative scenario, 52 years of fatigue life remain. A strong correlation between the deterministic and AASTHO methods of fatigue life evaluation was found, with the probabilistic method providing a consistently longer remaining fatigue life. By characterizing the fatigue damage accumulated during the monitoring period, identification of which details are the most heavily loaded, on both a daily, and monthly basis, was established. From the six months of data acquired, it was found that the northbound barrier lane is the most heavily loaded lane on the bridge, Wednesday is the most heavily loaded day of the week, and May is the most heavily loaded month. In addition to this, unexpected full composite action and no dynamic load influence was found to exist on the bridge under service conditions.

ACKNOWLEDGEMENTS

Enormous gratitude goes to my parents, Mark and Sandi Morgan. They've understood whole heartedly that this research has been a top priority for me and have generously fixed my toilets, my freezer, my lights, my kitchen sink, returned my recycling, and provided countless meals. They did all of this so that I could focus on this research and not worry about the smaller things in life. I'd like to thank my sister, Jenn Frank, for always listening regardless of whether she understood the content. Thanks to my brother, Chris Frank, and my two nephews, Aidan and Austin, for always making me smile, and giving me a much-needed sanity break to reflect on what is truly important. To my Grandpa, Harold Dunlop, for understanding when I burrowed myself in the research and lost all contact with the outside world. The drive-by honks always brought a smile to my face.

Next, I need to acknowledge my friends for sticking with Masters Chris. I realize I talked endlessly about my research, and they painfully listened for as long as I could talk about it. Because of them, my research may have taken a couple months longer, but my 20's weren't spent entirely in a library.

I was very fortunate to have a great advisory committee who provided valuable feedback and challenged me to develop a better thesis. My two advisors, Dr. Bruce Sparling and Dr. Leon Wegner, were a rock-solid sounding board for me when I needed it, and really pushed me to understand, at a fundamental level, what I was doing at every stage of the research.

Lastly, I'd like to thank the Ministry of Highways and Infrastructure and the City of Prince Albert for understanding the value in this research project, and for believing in me and the research team. Their support through both the project, and the research, has been instrumental to its success.

DEDICATION

To the family I was born into, and the family I have gained along the way.

TABLE OF CONTENTS

LIST OF TABLES

LIST OF FIGURES

LIST OF SYMBOLS

a	=	Present age of bridge
β	=	Reliability index
C	=	Stress cycles per truck passage
c_d	=	Cycles per truck passage
D	=	Palmgren-Miner's Damage Accumulation Index
D_j	=	Contribution of cycles n_j to Palmgren-Miner's Damage Accumulation Index
$D_{tot}(t)$	=	Total accumulated damage at year t
Δ	=	Palmgren-Miner's Critical Damage Index
Δ_f	=	Measured effective stress range; or calculated stress range
$(\Delta_f)_{eff}$	=	Effective stress range
δ_Δ	=	Coefficient of variation of Δ
f	=	Correction factor
F_{sr}	=	Fatigue resistance
F_{srt}	=	Constant amplitude fatigue threshold stress range
F_{s1}	=	Correction factor
F_{s2}	=	Corection factor
F_{s3}	=	Correction factor
γ	=	Fatigue constant
g	=	Estimated annual traffic growth rate
g_d	=	Lateral girder distribution
$g(F)$	=	Uncertainty model for the fatigue limit state function
h_d	=	Multiple presence factor
i_d	=	Impact factor
k	=	Number of different stress ranges
k	=	Current age of bridge
K	=	Fatigue detail constant
λ_Δ	=	Parameter for the lognormal distribution of Δ
M	=	Fatigue life
M_d	=	Moment range caused by the fatigue truck
M_i	=	Moment at location i

$\mu_{d(k)}$ = Mean damage in year k

$\mu_{d(1)}$ = Mean damage in first year of service

$N_b(t)$ = Number of cycles at bridge in year t, corresponding to a stress range, S_r

N_c = Specified number of design cycles

$N_{f,j}$ = Number of cycles until failure at the j^{th} stress range

$N_i(S_{ri})$ = Number of equivalent cycles at the index stress range

n_j = Number of cycles measured at the j^{th} stress range

N_m = Total number of cycles measured during the monitoring period

N_{yk} = Current traffic volume

P_f = Probability of failure

r = Annual increase in traffic volume

R^2 = Correlation coefficient

R_R = Resistance factor

R_s = Combined reliability factor

R_S = Partial load factor

R_{sa} = Partial load factor for analysis

R_{st} = Partial load factor for truck weight

R_{s0} = Base reliability factor

S_j = Average stress range for bin j

S_r = Stress range

S_{re} = Effective stress range

S_{ri} = Index stress range

$S_{r,j}$ = Stress range being measured

t = Year evaluated

T_a = Estimated lifetime average daily truck volume

x_Δ = Median value of Δ

Y = Remaining Fatigue life

z_x = Section modulus

ζ_Δ = Parameter for the lognormal distribution of Δ

LIST OF ABBREVIATIONS

AADT	Annual Average Daily Traffic
AADTT	Annual Average Daily Truck Traffic
ASCE	American Society of Civil Engineers
AASHTO	American Association of State Highway and Transportation Officials
BDI	Bridge Diagnostics Incorporated
CAFL	Constant Amplitude Fatigue Limit
CIF	Constraint Induced Fracture
FEM	Finite Element Model
FFT	Fast Fourier Transfrom
LEFM	Linear Elastic Fracture Mechanics
LRFD	Load and Resistance Factor Design
MHI	Ministry of Highways and Infrastructure
NB	Northbound
NCHRP	National Cooperative Highway Research Program
No.	Number
OSIM	Ontario Structure Inspection Manual
POI	Point of Interest
R^2	Correlation Coefficient
SB	Southbound
SHM	Structural Health Monitoring
TDMS	Technical Data Management System

CHAPTER 1. INTRODUCTION

1.1 Background

The Diefenbaker Bridge over the North Saskatchewan River is a vital river crossing that connects the southern region of Saskatchewan with the north. Located in Prince Albert, Saskatchewan, Canada, as shown in Figure 1.1, its importance to the provincial economy is well documented, making every decision regarding its maintenance highly important (Stantec, 2015). An evaluation and assessment of the bridge that was completed in November of 2016 (ISL, 2016) indicated that the fatigue life remaining on the bridge was nearly exhausted. Given the social, political, and economic impacts of this assessment, and the inherent uncertainty involved in the analysis, it was recommended that a structural health monitoring (SHM) system be implemented.

Figure 1.1 - Location of Bridge in Prince Albert, Saskatchewan (Google, 2019)

Structural health monitoring is becoming an increasingly justifiable method for reliably assessing the structural condition of a bridge. A tailored SHM system enables a better understanding of the in-situ loading and response characteristics of the bridge and, therefore, a more accurate assessment of the historical and ongoing fatigue effects. This understanding enables the owner to manage future maintenance costs because upgrading the fatigue critical details unnecessarily could result in a large expenditure being incurred before it is warranted.

The Diefenbaker Bridge, shown in Figure 1.2, was constructed in 1959 to carry traffic on Highway No. 2 over the North Saskatchewan River.

Figure 1.2 - Overview of the Diefenbaker Bridge

The seven-span bridge consists of two separate fracture critical superstructures, each comprising a cast-in-place concrete deck supported by two welded steel I-beams. It is considered fracture critical because of the non-redundant nature of the twin-girder design that would theoretically result in collapse if the flange of a longitudinal girder were to fail. The separate superstructures share cast-in-place concrete abutments and piers and have a total length of 304 meters.

The Diefenbaker Bridge has had a controversial history, having undergone different levels of repair in 1988, 2003, 2011, 2012, and 2016. The southbound bridge experienced a near-full-depth fracture of one of its girders in 2011 (Stantec, 2015). The failure was documented as one of the largest in-service fractures ever to have occurred on a fracture critical structure in Canada. The girder was repaired by splicing in a new welded “T” section of girder, which was followed

by live load testing to ensure that the repair was functioning as intended. Considering the nature of the fracture and the minimal amount of redundancy built into the superstructure, the bridge girders were retrofitted with stress relief holes to prevent future constraint-induced fractures (Ellis et al., 2013).

In 2015, a management plan (Stantec, 2015) was prepared that outlined the condition of the bridge, its estimated service life, maintenance needs, rehabilitation planning, and budget projections. This information was presented with the assumption that a fatigue analysis and revised load rating would not prevent the bridge from achieving a 120 year service life prediction. As a result of the 2015 program, recommendations were made for completing over $235,000 worth of maintenance work between 2016 and 2017. In addition, $2.28 million of work is planned in 2023 to rehabilitate the deck and expansion joints.

Given the extent of investment that was required in the near future, as well as the levels of damage and deterioration experienced throughout the bridge's history, the owner elected to perform an in-depth bridge assessment and evaluation of the superstructure, as shown in Figure 1.3, to get a deeper understanding of the bridge and potential issues that could affect its service life. In 2016, ISL Engineering completed an assessment and determined that the fatigue life of the bracing's connection to the girder web was nearly exhausted (ISL, 2016).

Figure 1.3 – View of the underside of the bridge superstructure, showing the girders and bracing configuration

Fatigue is a primary cause of mechanical failures of steel structures, including bridges. According to ASCE's Committee on Fatigue and Fracture Reliability, 80% to 90% of failures in metallic structures are related to fatigue (Ye, 2014). Fatigue has been researched extensively since the 1940's, but the fatigue process on bridge structures is unique due to the variable amplitude loading that occurs and the unique in-situ behaviour of every structure. There have been several bridges that have been instrumented for the purpose of fatigue evaluation, but the details in question are often instrumented such that the stress level and number of cycles can be inferred directly from the strain data. This approach was not taken in the case of the Diefenbaker Bridge, because the detail that was investigated was subjected to stress that was induced from not only the flexural action of the girder, but also due to secondary forces from both the transverse and lateral bracing. This complicated the data acquisition and the fatigue evaluation because the stress/strain contributions from each element had to be considered. Furthermore, in most of the published research, data acquisition has been limited to a few weeks.

1.2 Objectives

The overall objective of this research was to develop a more refined fatigue life assessment of the lateral bracing's connection to the girder web using structural health monitoring. With the overall objective in mind, the specific objectives of the research project were:

- To evaluate and compare the fatigue life of the bracing's connection to the girder web using a deterministic method, the method outlined in the American Association of State Highway and Transportation Official's Manual for Bridge Evaluation (AASHTO), and a probabilistic method;
- To characterize the fatigue damage accumulated per girder on a daily and monthly basis to reveal in-situ loading and response trends;
- To characterize the response of the structure in terms of the dynamic influence, degree of composite action, and lateral load distribution using the data collected over the monitoring period; and
- To evaluate the effectiveness of the selected instrumentation plan and make recommendations for future study.

With these primary objectives accomplished, future engineers and owners will be better prepared to perform more accurate fatigue life evaluations if presented with a similar problem. Infrastructure will continue to age, and the fatigue life of steel bridges will continue to expire.

Having evaluated the different methodologies for fatigue evaluation using real data, this research will serve as a starting point for the fatigue analysis of any steel structures that preliminary analysis has deemed to be close to the end of its fatigue life.

1.3 Scope of Research

The Diefenbaker Bridge, located in Prince Albert, Canada, was selected to be the subject of this study. Descriptions of the structural features of the Diefenbaker Bridge are provided in Chapter Three. The ultimate objective of this research was to produce a refined fatigue life evaluation of the bracing's connection to the girder web. To accomplish this goal, there were three primary components: development and implementation of a structural health monitoring plan that acquired true-to-life data, finite element modeling to understand the complex stress state at the detail, and numerical modelling of the remaining fatigue life using three different approaches. As a secondary objective, characterization of the fatigue damage was completed to identify trends in daily and monthly fatigue damage, as well as loading trends across bridge components.

The structural health monitoring component consisted of developing an instrumentation plan, installation of the sensors, and data collection for six months. Details on the structural health monitoring plan are provided in Chapter Three. Two primary types of data were collected: calibration data, and rainflow data. Calibration data was collected for the purposes of identifying in-situ behaviour of the bridge such as degree of composite action, lateral load distribution, and dynamic load influence. Rainflow data was collected to identify the number of cycles, and magnitude, of stress ranges present on the structure.

Finite element modelling was completed to understand the three-dimensional stress state at the gusset plate's weld termination on the girder web. Since the stress at this point is a product of several sources (i.e., lateral bracing, transverse bracing, girder), the finite element models were used to isolate the contributions from each source. The finite element models were calibrated such that the response in the field closely matched the response in the model. Information on the modelling, and resulting stress states, can be found in Chapter Four.

Lastly, the fatigue damage on the structure was explored. Numerical modelling of the remaining fatigue life was calculated using three different approaches: a deterministic approach, AASHTO's approach, and a probabilistic approach. Furthermore, the fatigue damage was characterized on element basis (i.e. which girder is most heavily loaded, which direction of

travel, etc.), as well as on a daily, and monthly basis. The results from this analysis can be found in Chapter 4.

1.4 Organization of Thesis

This thesis is organized into five chapters, with additional information provided in the appendices, as shown in Figure 1.4. Chapter One introduces the Diefenbaker Bridge and its history and presents the primary objectives and scope of the research project. Chapter Two introduces pertinent background material by reviewing existing literature. The process of fatigue is explained, as well as the methods used to characterize and evaluate fatigue life. The literature review focuses on the application of SHM and how it applies to fatigue evaluation on bridges. The SHM plan is presented in Chapter Three. The rationale behind the selected instrumentation and the data acquisition system are explained. Chapter Four presents the methodology employed to perform the analyses, and the resulting outcomes. In-situ lateral load distribution, dynamic influence, and the degree of composite action are investigated. Remaining fatigue life is calculated using a deterministic method, AASHTO's approach (AASHTO, 2011), and a probabilistic method, and the results are compared. Variations in the measured response on a daily, and monthly basis are compared and loading trends are identified. Lastly, the conclusions and recommendations for future work are provided in Chapter Five.

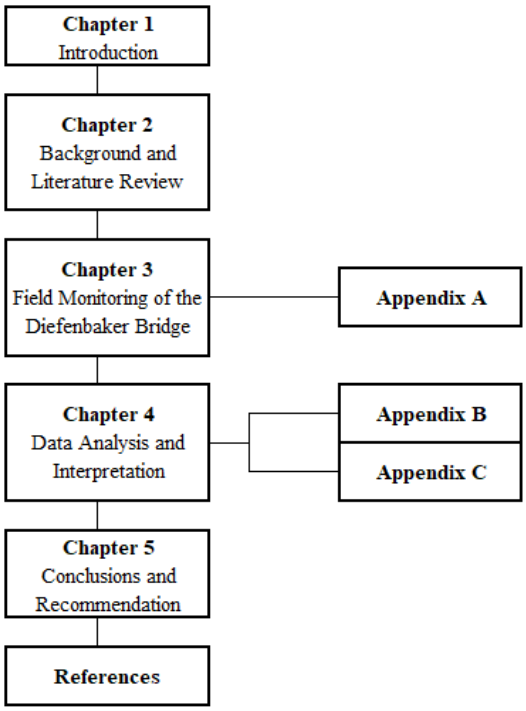

Figure 1.4 - Information flow diagram for the Thesis layout

CHAPTER 2. BACKGROUND AND LITERATURE REVIEW

2.1 Definition of Fatigue

Fatigue in bridges is the localized and progressive accumulation of damage due to the repetitive loading from vehicles. It has been studied extensively since the 1940's, yet still remains as one of the primary failure mechanisms of steel structures (Ye, 2014). This is because, while the cyclic stresses in bridges are often well below the yield strength of the steel, stress concentrations from defects or microcracks in the material can lead to crack growth (Barsom and Rolfe, 1999). Initial defects in the material can stem from several sources, including: the manufacturing process, cutting, straightening, shearing, irregularities in mill scale, inclusions, or mechanical notches due to handling (Fisher et al., 1998). Flaws can also be introduced when bolted, riveted, or where welded connections are present. Welded connections are particularly prone to fatigue due to the presence of residual stresses caused by differential heating and/or cooling, partial penetration, lack of fusion, and micro flaws at the weld toe (Fisher et al., 1998). In welded steel bridges, the primary variables used to evaluate the fatigue performance are the magnitude of the stress range, the number of cycles at each stress range, and the geometry of the detail (Fisher et al., 1974). Changes in geometry also affect fatigue behaviour because these changes can result in stress concentrations (Barsom and Rolfe, 1999). Fasl (2013) provided an effective illustration of the effects of geometry using the details shown in Figure 2.1; the detail with no change in geometry will have the best fatigue behaviour (i.e., Figure 2.1 (a)), while the detail with the most sudden change in geometry will have the worst fatigue behaviour (i.e., Figure 2.1 (c)).

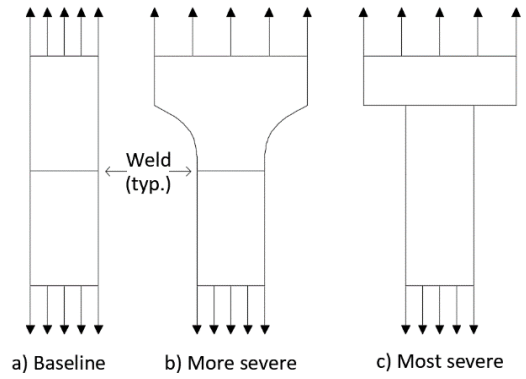

Figure 2.1 - Illustration of how geometry affects fatigue behaviour (adapted from Fasl, 2013)

2.2 Characterizing Fatigue Resistance

There are two approaches employed for fatigue damage evaluation of bridges: a stress-based approach that uses the well-known stress-cycle relationship, and a fracture mechanics approach that explores crack initiation and propagation due to a stress field at the crack tip (Ye, 2014).

2.2.1 Stress-Based Approach

In the stress-based approach, a detail's fatigue resistance is determined experimentally by subjecting it to a constant amplitude stress range (S) and counting the number of cycles (N) until it fails. The experiment is then repeated at a different stress range and an S-N curve, similar to that shown in Figure 2.2, is created. It is important to note that stress risers such as discontinuities, imperfections, and residual stress can lead to higher localized stress magnitudes than are typically calculated using engineering mechanics.

Given the scatter in the data that accompanies this type of experiment, a regression analysis is typically used to define the line that best represents the trend in data. The slope of the resulting trend line on a log-log scale for most metals typically ranges from -2 to -4 (MPa/# cycles). The value used for design purposes is typically determined by shifting the mean value line by approximately two standard deviations so that the line corresponds to a 95% confidence interval, or a 5% probability of failure (Keating and Fisher, 1986), as shown in Figure 2.2.

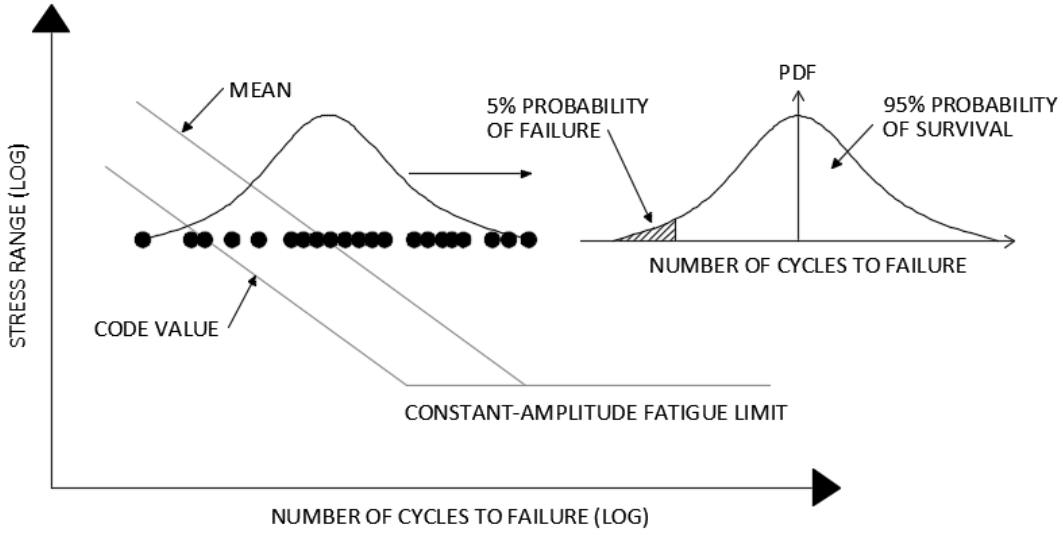

Figure 2.2 –A typical S-N relationship, showing regression lines from a fatigue test (adapted from Keating and Fisher, 1986)

The Canadian Highway Bridge Design Code CSA S6-14 currently uses Equation 2.1 for design (CSA, 2014):

$$F_{SR} = \left(\frac{\gamma}{N_C}\right)^{\frac{1}{3}} \quad 2.1$$

where:

$F_{SR} =$ fatigue resistance (MPa);

$\gamma =$ fatigue constant that depends on the detail category (MPa); and

$N_C =$ specified number of design stress cycles.

This equation is based on the assumption of a slope of -3 MPa/# cycles and a corresponding fatigue constant, as shown in Table 2.1. The fatigue categories are described in Chapter 10 of CSA S6-14 and depend on the geometry of the detail and the direction of applied stress. The fatigue constant and constant amplitude fatigue stress threshold for each category of detail are summarized in Table 2.1.

Table 2.1 - Fatigue detail category characteristics according to CSA S6-14 (CSA, 2014)

Category	Fatigue Constant, ɣ	Constant Amplitude Fatigue Threshold Stress Range, F_{srt} (MPa)
A	8190 x 10^9	165
B	3930 x 10^9	110
B1	2000 x 10^9	83
C	1440 x 10^9	69
C1	1440 x 10^9	83
D	721 x 10^9	48
E	361 x 10^9	31
E1	128 x 10^9	18

Typically, details with Categories C through E1 will govern the design life of a structure. Examples of these categories include details with discontinuities or attachments with a fillet or groove weld parallel and perpendicular to the applied stress.

2.2.1.1 Palmgren-Miner's Rule

Since the stress on bridge structures is variable, a cumulative damage rule is required to relate this variable amplitude stress to the constant amplitude fatigue data from which the specifications were derived. The stress-based approach to fatigue utilizes a relationship between

constant amplitude stress (S) and the number of stress cycles (N). Many specifications have adopted this approach, including AASHTO (2011) and CSA S6-14 (CSA, 2014). The Palmgren-Miner linear damage hypothesis, also called Miner's Rule, relates the variable amplitude loading commonly found on bridge structures, to the S-N relationships derived from the fatigue experiments. Miner's rule is one of the most widely used damaged accumulation rules. The following equations represents Miner's rule (Miner, 1945):

$$\boldsymbol{D_j = \frac{n_j}{N_{f,j}}} \qquad 2.2$$

$$\boldsymbol{D = \sum_{j=1}^{k} D_j} \qquad 2.3$$

where:

$D_j =$ contribution of cycles n_j to Palmgren-Miner's damage accumulation index;

$D =$ Palmgren-Miner's damage accumulation index;

$S_{r,j} =$ stress range being measured;

$n_j =$ number of cycles measured at $S_{r,j}$;

$N_{f,j} =$ number of cycles until failure at $S_{r,j}$; and

$k =$ number of different stress ranges.

According to Palmgren-Miner's Rule, every stress range causes damage, but the damage is only proportional to the number of cycles that causes failure at that stress range. The total damage is the sum of the respective damages; however, this approach does not consider the sequence of loading. For example, if an overload stress range occurs with a low frequency after many cycles at low stress ranges, this condition has been found to increase the fatigue life of the specimen (ASCE, 1982). This effect is not considered with Palmgren-Miner's rule. This rule also does not consider the effect that the average stress may have on the fatigue life, although the average stress has been shown not to have a large effect on the fatigue life (Fisher et al., 1998). Despite the shortcomings, for bridges that are subjected to random loading with few overloads, Palmgren-Miner's rule is generally considered to describe the damage with sufficient reliability.

A primary concern in the application of Palmgren-Miner's rule is how to deal with cycles whose magnitudes are below the constant amplitude fatigue limit (CAFL). Connor and Fisher (2006) proposed omitting all cycles that have a magnitude of less than 25% to 50% of the CAFL. The current European practice is to weigh the lower stress ranges differently (slope of 5 cycles/MPa, rather than 3 cycles/MPa)(ECCS Technical Committee 6, 1985). This European

practice has been shown to be unconservative for various longitudinally welded attachments (Fisher et al., 1998). Swenson and Frank (1984) reported that all cycles contribute to damage. This difference of opinion among the international community is explored in more detail in Section 2.3.

2.2.1.2 Effective Stress Range

Multiple stress ranges can be converted into a single, equivalent stress range using the concept of effective stress. This is done because a bridge component experiences many different stress ranges, making a summation of the damage contributions impractical (Fasl, 2013). The purpose of the effective stress range is also to relate variable amplitude loadings to an equivalent constant amplitude loading. This is done by equating equations 2.1 and 2.3 to create:

$$S_{re} = \left(\frac{\sum n_j \times S_j^3}{N_m}\right)^{1/3} \quad 2.4$$

where:

$S_{re} =$ effective stress range (MPa);

$n_j =$ measured number of cycles in a bin corresponding to S_j;

$S_j =$ average stress range for bin j (MPa); and

$N_m =$ total number of cycles measured during the monitoring period;

This method allows the fatigue lives of different details to be compared using a single stress range. This is useful for infrastructure owners because it allows the identification of problems within a single bridge, or across an entire bridge inventory. However, this method has shortcomings. The effective stress range can be skewed if a large percentage of the cycles are small in magnitude (i.e., the first few bins of a rainflow analysis as described in Section 3.6.3). This means that two different spectra of stress ranges can generate the same amount of damage on a detail, but the effective stress range may be different. This is particularly important because comparing multiple details on a structure is difficult since the effective stress range depends on the number of cycles in each recorded stress range.

2.2.1.3 Index Stress Range

Another useful tool for engineers is the index stress range. The index stress range was developed to compare relative fatigue damage accumulations across different locations on a bridge, or at the same location, but across different time domains (Fasl, 2013). The index stress range is determined by normalizing either the effective stress range or the measured data to the

same stress range. By employing this method, the number of cycles at the selected stress range can be compared directly to determine the relative fatigue damage (i.e. twice as many cycles equates to twice as much damage). This can be done using either an effective stress range or using a histogram of stress ranges. Using the effective stress range method:

$$\boldsymbol{N_i(S_{ri}) = N_m \, x \, \frac{S_{re}^3}{S_{ri}^3}} \qquad 2.5$$

where:

$N_i(S_{ri}) =$ number of equivalent cycles at S_{ri} ;

$S_{ri} =$ index stress range (MPa);

$S_{re} =$ effective stress range (MPa); and

$N_m =$ total number of cycles measured during the monitoring period.

Alternatively, the histogram data can be used directly (if the details being compared are within the same fatigue category):

$$\boldsymbol{N_i(S_{ri}) = \sum n_j \, x \, \frac{S_j^3}{S_{ri}^3}} \qquad 2.6$$

where:

$N_i(S_{ri}) =$ number of equivalent cycles at S_{ri};

$n_j =$ measured number of cycles in the bin corresponding to S_j ;

$S_j =$ average stress for bin j (MPa); and

$S_{ri} =$ index stress range (MPa).

This method can also be applied to details with different fatigue categories; however, for the purposes of this research project, all details considered were in the same category. The index stress range can be set at any magnitude; commonly, though, the range is set to the CAFL of the given detail category. Fasl (2013) demonstrated the merits of the index stress range and validated the conclusion of Connor and Fisher (2006) with respect to the omission of stress ranges with amplitudes up to 50% of the CAFL.

2.2.2 Linear Elastic Fracture Mechanics

Linear-elastic fracture mechanics (LEFM) can be used to characterize fatigue behaviour. While this approach to fatigue evaluation is not used as often as the stress-based approach, it provides valuable insight into the fatigue process. In the stress-based approach, only the number of cycles until failure is calculated. In the LEFM approach, this is taken a step further, with the

initial flaw size and fracture toughness being accounted for in the calculation of a crack propagation rate. The most common LEFM model relates fracture toughness to stress and crack length and uses correlation/correction factors because stress and crack length are not assessed directly (Fisher et al., 1998). These factors can be determined empirically or numerically and can be found in fracture mechanics handbooks such as Barsom and Rolfe (1999). Using this approach, crack growth can be calculated, with three distinct regions becoming apparent:

1. Region 1 (crack initiation) – cracks do not grow or grow at a very slow rate;
2. Region 2 (crack propagation) – crack growth occurs; and
3. Region 3 (failure) – the fracture toughness of the material has been reached and the crack growth rate increases very rapidly until failure occurs.

With this approach, the factors affecting fatigue performance can be evaluated. It was found that increasing the fracture toughness of the material or the critical crack length has very little effect on the fatigue strength. The factor that most influences behaviour is the initial flaw size, as it has the greatest influence on the number of cycles until failure (Fasl, 2013). Since initial flaw size is such an influential factor, the linear elastic fracture mechanics approach is not commonly used because accurately determining this flaw size is very difficult in practice, particularly for bridges.

2.2.3 Cycle Counting Method

There are several different methods for quantifying the number of stress cycles that a structural detail experiences over a given period. ASTM E1049 specifies four primary methods: the level crossing method, peak counting method, simple-range method, and rainflow method (ASTM, 2011). The most common method employed for fatigue analysis is the rainflow counting method. This method is well suited for variable amplitude fatigue analysis since it identifies stress ranges associated with close-loop hysteresis. It also allows for a mean stress to be determined. This information is helpful to identify whether a stress range is compressive or tensile, or both. For example, if stress values are recorded between 20 MPa and 40 MPa, the range would be 20 MPa, and the mean value would be 30 MPa. Figure 2.3 depicts a common variable amplitude stress history, along with the hysteresis graph plotted directly below it. In this figure, four cycles are counted: A-D-I, B-C-B, E-F-E, and G-H-G. These represent one large

cycle, two intermediate cycles, and one small cycle. Each cycle has its own magnitude and mean stress.

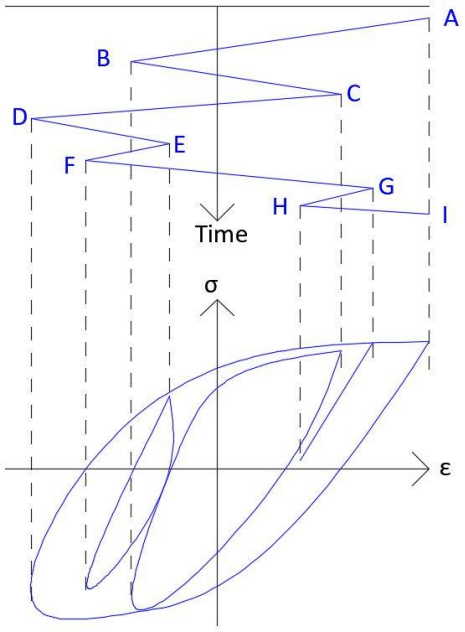

Figure 2.3 – Variable amplitude stress history with associated hysteresis graph demonstrating the rainflow counting method

A simplified rainflow method resolves the stress history into full cycles, whereas the rainflow method will count half cycles. If the simplified rainflow method is used to determine amplitudes of cycles, and the cycles are transformed into an effective stress range, results have been found to match historic S-N curves (Swenson and Frank, 1984).

2.3 Fatigue Resistance of Bridges Under Variable Amplitude Loading

A substantial amount of research into the fatigue behaviour of bridge structures was completed by the National Cooperative Highway Research Program (NCHRP) in the 1970's and the 1980's. Prior to the knowledge acquired from the NCHRP projects, fatigue guidelines in the AASHTO LFRD specifications (AASHTO, 2017) were based on smaller scale specimens under constant amplitude loading. Since the loading on bridges is variable, NCHRP sponsored a number of projects whose intent was to characterize the fatigue resistance of various details used in bridges.

NCHRP Project 12-12 used simulated traffic loading to investigate the effects of variable amplitude loading (Schilling et al. 1978). Researchers found that if the variable data was transformed into an effective stress range, the differences between the constant amplitude data

and the variable amplitude data were statistically insignificant. This is important because it meant that the fatigue life of details subjected to variable amplitude loading could be determined from constant amplitude data. They also found that, while a slope (B) of 2 cycles/MPa fit the data better, Palmgren-Miner's slope (B) of 3 provided a conservative approach and was already accepted by the engineering community.

NCHRP Project 12-15(4) explored fatigue if the majority of cycles were less than the CAFL (Fisher et al.,1983). More specifically, the frequency of stress ranges above the CAFL and the magnitude of the peak stress range, and how these factors affected the fatigue performance of details, was investigated. Three loading scenarios were investigated, as shown in Figure 2.4:

1. Both the effective stress range and the maximum stress range were above the CAFL;
2. The effective stress range was below the CAFL, but the maximum stress range was above the CAFL; and
3. Both the effective stress range and the maximum stress range were below the CAFL.

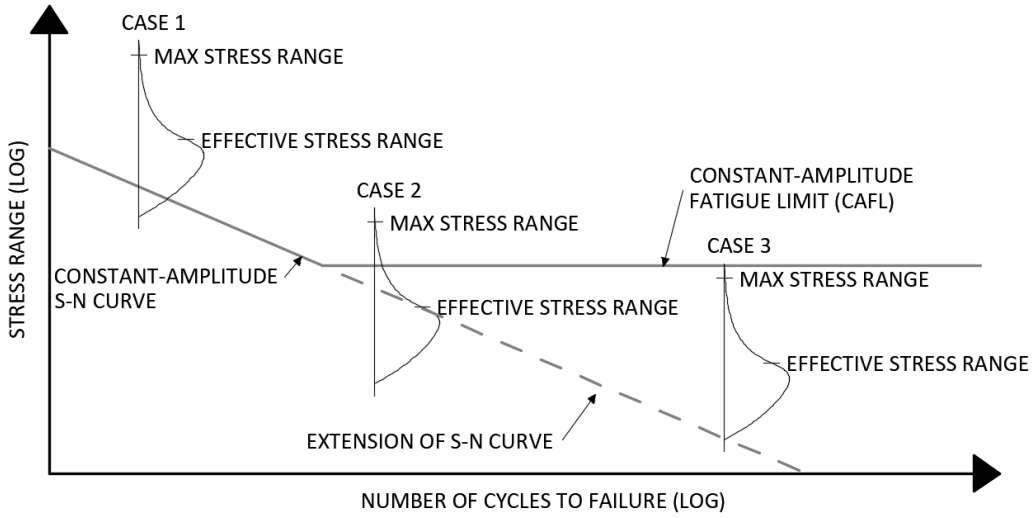

Figure 2.4 - Variable amplitude loading scenarios considered in the NCHRP Project 12-12(5) (adapted from Fisher et al., 1983).

This research revealed a few important phenomena: a) if any portion of the applied stress was above the CAFL, fatigue cracking would occur (i.e., Case 1 and Case 2), and b) if no cycles were observed above the CAFL then fatigue cracking did not occur (i.e., Case 3). It was also found that the fatigue life of the detail could be calculated using a straight-line extension of the S-N curve, which suggests that all stress cycles contributed to damage.

The 1974 AASHTO fatigue specification was based on data from over 800 constant amplitude fatigue tests conducted in NCHRP projects from 1966 through 1972 (Keating and

Fisher, 1986). Since a large number of tests had been performed since 1972, the objective of NCHRP Project 12-15(5) was to review and expand on the current fatigue database (Keating and Fisher, 1986). Data from the United States, Japan, Canada, Germany, and The Office of Research and Experiments of the International Institute of Technology were evaluated and added to the database. This data resulted in another category of fatigue detail being created, and for Fatigue Constants (γ) to be created. These constants, similar to what was shown in Table 2.1, are approximately the same as what is used in CSA S6-14 (CSA, 2014) and AASHTO LFRD specifications (AASHTO, 2017) today.

While the understanding of fatigue performance under variable amplitude loading was increasing, an easily applied procedure for evaluating bridge structures was lacking. The objective of NCHRP Project 12-28(3) was to develop a procedure for both designing and evaluating bridges for fatigue (Moses et al., 1987). In-situ bridge data and past research were used to recommend a fatigue evaluation truck could be expected to produce similar amounts of damage as would be expected from a typical assortment of trucks at a site. The fatigue truck, shown in Figure 2.5, was based on weigh-in-motion data from 30 sites across the United States and 27,000 observed trucks.

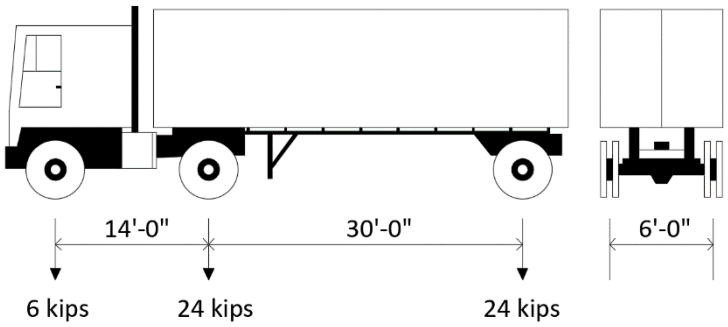

Figure 2.5 - Axle Loading and Spacing of Fatigue Truck (adapted from AASHTO, 2011)

Using this approach, a gross weight of 54 kips can be assumed if site specific data is not available. If site specific data is available, the authors present a method for modifying the fatigue truck. The design stress range (S_{XD}) for fatigue can be calculated using Equation 2.7:

$$S_{XD} = \frac{M_d}{Z_x}\, x\, g_d\, x\, i_d\, x\, h_d\, x\, c_d \qquad 2.7$$

where:

$M_d =$ moment range caused by the fatigue truck;

$z_x =$ section modulus;

$g_d =$ lateral girder distribution factor;

i_d = impact factor ;

h_d = multiple presence factor; and

c_d = cycles per truck passage.

The authors also present a method to modify the girder's section modulus to account for unintended composite action. With the stress range calculated, the remaining fatigue life may be estimated using the straightforward calculation shown as Equation 2.8:

$$\boldsymbol{Y_F = \frac{f \times K \times 10^6}{T_a \times C \times (R_S \times S_r)^3} - a} \qquad 2.8$$

where:

Y_F = remaining fatigue life in years;

K = detail constant (ksi^3);

T_a = estimated lifetime average daily truck volume;

C = stress cycles per truck passage;

S_r = stress range (ksi);

R_S = combined reliability factor = $R_{S0}(F_{S1})(F_{S2})(F_{S3})$;

R_{S0} = base reliability factor (1.35 for redundant members, 1.75 for non-redundant);

F_{S1} = correction if stresses are measured (0.85);

F_{S2} = correction if site-specific truck traffic weighs less than standard fatigue truck;

F_{S3} = correction for a more accurate calculation of the lateral distribution factor;

a = present age of bridge in years; and

f = 1.0 for calculating safe life and 2.0 for calculating mean life.

A safe fatigue life was defined as a 0.1% probability of failure, whereas a mean life represented a 50% probability of failure.

In 2011, AASHTO released an updated version of the above method in the Manual for Bridge Evaluation, 3rd edition (AASHTO, 2011). This method was similar in concept but utilized new formulas and new values for several parameters that better aligned with the AASHTO LFRD Specifications (2017). The revised formula for calculating the remaining fatigue life was:

$$\mathbf{Y = \frac{R_R \times A}{365 \times n \times (AADT)_{SL} \times (R_S \times S_R)^3}} \qquad 2.9$$

where:

Y = remaining fatigue life in years;

R_R = resistance factor (Table 2.3);

A = detail constant $(ksi)^3$ (Table 2.1);

n = stress cycles per truck passage;

$\mathrm{AADT_{SL}}$ = average number of trucks per day in a single lane averaged over the entire fatigue life;

S_R = stress range (ksi); and

R_S = partial load factor (Table 2.2).

This method does not distinguish between redundant and non-redundant details, but provides three levels of safety for the fatigue life by varying the partial load and resistance factors:

1. Minimum life (a design fatigue life defined at two standard deviations away from the mean fatigue resistance);
2. Evaluation life (design fatigue life defined at one standard deviation away from the mean fatigue resistance); and the
3. Mean life.

2.4 Structural Health Monitoring of Existing Bridges for Fatigue Evaluation

As structures continue to age, fatigue life evaluation is becoming increasingly common. AASHTO's Manual for Bridge Evaluation (2011) is often used in combination with a structural analysis for this purpose. However, this approach requires several assumptions to be made by the engineer that leads to a large degree of uncertainty. The primary uncertainties are:

- What vehicle is used to create the stress range;
- How many times does this vehicle cross the structure, and how many times has it crossed the structure historically;
- How is load distributed between girders, and is one direction loaded more heavily than the other;
- What degree of composite action exists; and
- What is the dynamic influence of the moving load?

Because of these assumptions, field monitoring is often recommended to reduce the degree of uncertainty in the analysis. While instrumentation can reduce the uncertainty in the analysis, it does not completely remove it. Three areas of uncertainty remain: the location of sensors, the quality of the data, and the interpretation of the data. Zhou (2006) recommended that bridges be

modelled first to help optimize the location of sensors because it not always obvious where the critical location will be.

Connor and Fisher (2006) recommend that at least four weeks of data be obtained since loading can change from day to day, and week to week. This also allows a reasonable amount of time to identify the maximum stress range. However, Connor and Fisher (2006) also note that these stress ranges do not often occur, and as such, do not significantly contribute to fatigue damage.

Interpretation of the data is very important when it comes to fatigue evaluation. Of primary concern is determining which cycles to include in the analysis. All instrumentation will have electromechanical noise, which can sometimes be interpreted as small magnitude stress ranges that do not actually contribute to damage. Electromechanical noise can be limited to less than 10 microstrain in most data acquisition systems, with some able to limit noise to between 2-5 microstrain (Connor and Fisher, 2006). In addition to ignoring these cycles, many practitioners will truncate their data up to as much as 25%-50% of the CAFL for each fatigue category (Connor and Fisher, 2006; Zhou, 2006). Truncating this information is done because the effective stress range is very sensitive to the number of cycles within each bin. It is not uncommon for the majority of cycles to be found in the smaller amplitude bins due to wind, smaller vehicles, and electromagnetic noise. This results in an artificially small effective stress range if these data are considered, that will, if used in conjunction with the AASHTO Guide for Bridge Evaluation (1990), lead to an infinite fatigue life. The most recent version of this manual (2018), uses the maximum stress range as a metric for infinite fatigue life that is consistent with the long-term fatigue tests studied by Fisher et al. (1983).

Connor and Fisher (2006) take truncation one step further by suggesting that vehicles less than 20 kips could be neglected from the fatigue analysis because they were not included in the load spectrum used to develop the AASHTO LRFD Specifications (2017). In other words, this implies that vehicles less than 20 kips only cause a small amount of damage. This is consistent with research done on the Patroon Island Bridge in New York (Connor and Fisher, 2006).

While most research supports the truncation of lower stress ranges, Swenson and Frank (1984) state that all cycles contribute to the accumulation of fatigue damage. Their research indicated that while, in most bridges, truncating the lower magnitude stress cycles did not affect

the fatigue evaluation, in some bridges, this truncation will produce a unconservative evaluation of the fatigue life.

Lastly, a source of uncertainty during the field monitoring arises from the interpretation of the data. Leander et al. (2010) performed a structural analysis and evaluated a rail bridge in Stockholm based on Swedish Regulations, which resulted in the conclusion that the fatigue life had been exhausted. The analysis found that 40% of the fatigue life was consumed in a single year, despite the structure having been in service for over 50 years with no damage apparent. The discrepancy between reality and theory was attributed to conservative safety margins embedded in the standard being used, improper classification of fatigue details, and an error in the application of Palmgren-Miner's rule. By simply changing the critical fatigue detail category, the estimated damage index reduced from 0.4 per year, to 0.018 each year. The structure was later instrumented, and fatigue damage was ruled out as a concern on that basis. This exemplifies the importance of understanding the process of fatigue data interpretation.

2.5 Methods of Calculating Remaining Fatigue Life

There are two primary methods for calculating the remaining fatigue of a bridge structure: deterministic methods, and probabilistic methods. The deterministic method is most commonly used due to its simplicity, but may not be the most applicable to the evaluation of bridges since it does not account for uncertainty. Probabilistic methods can account for the complexity of the fatigue process and the variability in the cyclic loading that bridges experience. With each method considered, the outcome corresponds to a specific probability of failure, which must be considered if a negative remaining fatigue life is calculated. In each, however, fatigue failure will occur when a crack reaches a critical length causing fracture. In the case of fracture critical structures such as the Diefenbaker Bridge, fracture of a single connection may lead to collapse of the entire structure.

2.5.1 General Considerations for Fatigue Life Evaluation

2.5.1.1 Accounting for Traffic Volume over Time

While the fatigue damage caused during a period of instrumentation can be calculated directly, the fatigue life of a detail is dependent on the accumulation of damage over the structure's service life. Since the load-induced stresses that cause fatigue are primarily caused by vehicular loading, understanding the traffic volume on the bridge over its lifetime is crucial to an accurate calculation of remaining fatigue life. The challenge with this is that traffic volume is

irregular, and can increase or decrease on any given day, or hour, or year, based on local economic conditions, weather, accidents, or a number of other influencing factors. This makes modelling traffic accurately very difficult. Many structures, including the Diefenbaker Bridge, will have Annual Average Daily Traffic (AADT) volumes from more recent studies, and these can be used to validate the selected traffic model.

There are five primary traffic models that are typically selected to characterize fatigue damage on a bridge, as demonstrated in Figure 2.7 (Fasl, 2013):

1. Annual growth at a constant rate;
2. Annual growth with a gradual limit;
3. No growth;
4. Slow growth with a gradual limit; and
5. Quick growth with a gradual limit.

Determining which model best applies to a bridge will be location-specific; however, a bounded traffic volume approach can be employed using multiple models. In the example shown in Figure 2.6, the traffic volume is assumed to be known at year 20, either from field measurements or from traffic count data. Beyond year 20, the volume varies depending on the model chosen.

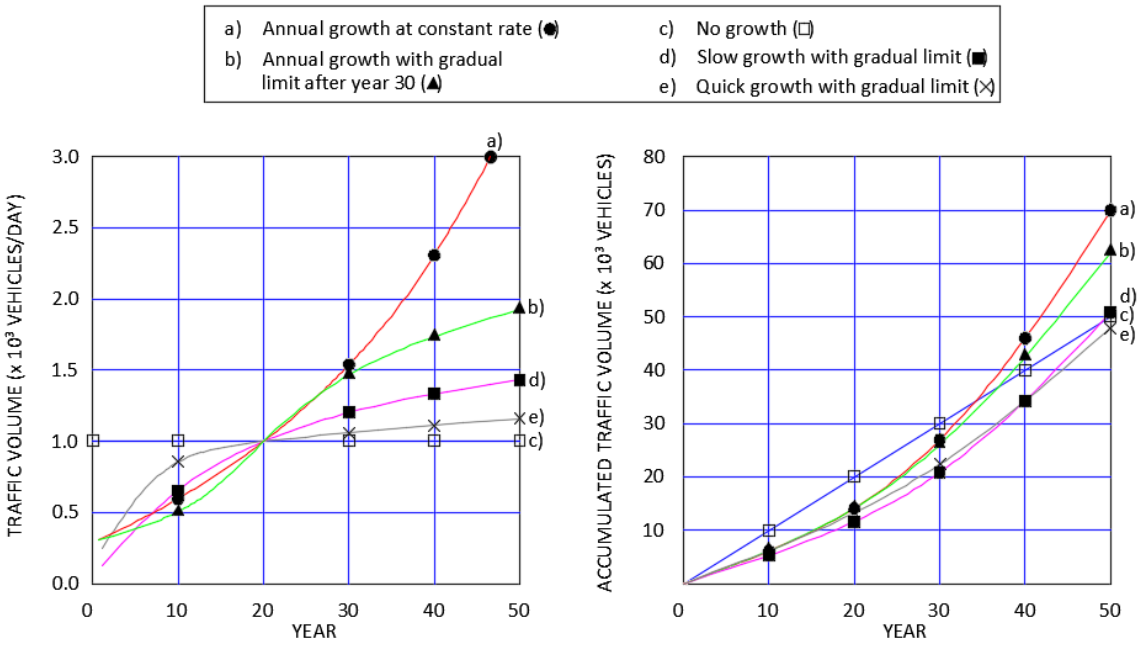

Figure 2.6 - a) Annual traffic volume and b) Accumulated traffic volume for different growth models (adapted from Fasl, 2013).

By evaluating the fatigue life with varying traffic growth rates, a bounded solution can be calculated (i.e., 2% constant traffic growth to 6% constant traffic growth).

Certain traffic models are more useful depending on the method of fatigue evaluation selected. For the deterministic approach, closed form solutions that can be obtained from annual growth or no growth models are advantageous because fatigue life can then be derived. With the gradual limit models, general solutions require iteration. All models can be used with the probabilistic approach because the damage must be calculated each year in order to determine the probability of failure. The AASHTO Manual for Bridge Evaluation recommends a growth rate ranging from 2% to 6%, since a constant traffic volume on a structure is not probable (AASHTO, 2011). However, traffic growth cannot be expected to grow indefinitely and, as such, caution must be exercised if considering periods longer than 30 years. In these scenarios, traffic counts or in-situ monitoring may be required to validate assumptions.

2.5.2 Deterministic Approach

In the deterministic approach to fatigue life evaluation, the damage for a certain monitoring period is used to estimate damage in the past, and to forecast damage in the future. A traffic growth rate is assumed and damage is accumulated over the service life of the bridge until failure occurs. The fatigue life can be calculated using (Fasl, 2013):

$$\mathbf{m} = \frac{\log\left(\frac{\mathbf{r}\times\mathbf{A}}{\mathbf{N_{yk}}\times \mathbf{S_r^3}}\times(\mathbf{1}+\mathbf{r})^{(\mathbf{k}-\mathbf{1})}+\mathbf{1}\right)}{\log(\mathbf{1}+\mathbf{r})} \qquad 2.10$$

where:

m = fatigue life in years;

r = annual increase in traffic volume;

N_{yk} = current traffic volume;

k = current age of the bridge.

S_r = stress range; and

A = detail fatigue constant.

If the mean value for the fatigue constant is used in place of the design value (A), the mean fatigue life can be calculated. The design value will produce a probability of failure of 5% (95% confidence interval), whereas the mean value will correspond to a probability of failure of 50%. Since the stress range and traffic volume correspond to the current year, either the index stress range or effective stress range can be used, along with their corresponding number of cycles.

2.5.3 AASHTO Approach

The AASHTO Manual for Bridge Evaluation (AASHTO, 2011) uses a semi-probabilistic method for calculating the remaining fatigue life that can be applied at three degrees of safety:

1. Minimum – 2% probability of failure (two standard deviations below the mean);
2. Evaluation – 16% probability of failure (one standard deviation below the mean); and
3. Mean – 50% probability of failure.

This method follows Palmgren-Miner's rule such that the stress range can be calculated as:

$$(\Delta \mathbf{f})_{\mathbf{eff}} = \mathbf{R_s} \times \Delta_f \qquad 2.11$$

where:

$R_s =$ stress range estimate partial load factor (Table 2.2);

$\Delta_f =$ measured effective stress range using Palmgren-Miner's rule; or calculated stress based on AASHTO's fatigue truck.

The partial load factor considers two sources of uncertainty:

1. The uncertainty in the analysis; and
2. The uncertainty in the assumed truck weight.

The AASHTO Manual for Bridge Evaluation recommends that the values in Table 2.2 be used for the stress range partial load factor.

Table 2.2 - Stress range estimate partial load factors (AASHTO, 2011)

Fatigue Life Evaluation Methods	**R_s**
Stress range by simplified analysis, and truck weight per AASHTO LRFD Design Article 3.6.1.4	1.00
Stress range by simplified analysis, and truck weight is estimated through weigh-in-motion study	0.95
Stress range by refined analysis, and truck weight is defined by AASHTO LRFD Design Article 3.6.1.4	0.95
Stress by refined analysis, and truck weight by weigh-in-motion study	0.90
Stress range by field-measured strains	0.85
Mean fatigue life (all methods)	1.00

The fatigue life (Y) can then be calculated using Equation 2.12, where R_R is per Table 2.3:

$$\mathbf{Y} = \frac{\mathbf{R_R \times A}}{\mathbf{365 \times n \times (ADTT)_{SL} \times ((\Delta f)_{eff})^3}} \quad 2.12$$

where:

R_R = resistance factor;

n = number of stress cycles per truck passage; and

$(AATT)_{SL}$ = average number of trucks per day in a single lane over the fatigue life.

The $(AATT)_{SL}$ must be calculated as outlined in the commentary of AASHTO's Bridge Evaluation Guidelines. The number of stress cycles is estimated using the AASHTO LRFD Specifications (2010) Table 6.6.1.2.5-3, influence lines, or field measurements. The resistance factor, R_R, may be determined from Table 2.3.

Table 2.3 - Resistance factor (R_R) (AASHTO, 2011)

AASHTO Fatigue	**R_R**		
Category	**Minimum Life**	**Evaluation Life**	**Mean Life**
A	1.0	1.7	2.8
B	1.0	1.4	2.0
B'	1.0	1.5	2.4
C	1.0	1.2	1.3
C'	1.0	1.2	1.3
D	1.0	1.3	1.6
E	1.0	1.3	1.6
E'	1.0	1.6	2.5

This method was evaluated by researchers following its release in NCHRP Project 12-81 (Bowman et al., 2012); as a result, a slightly different equation was proposed. Equation 2.13 follows a deterministic approach, except that it has similar load factors to AASHTO's approach:

$$\mathbf{Y} = \frac{log\left(\frac{\left(\mathbf{R_R \times A \times g(1+g)^{a-1}}\right)}{\mathbf{365 \times n \times \left((\Delta_f)_{eff}\right)^3 \times [(ADTT)_{SL}]_a}} + \mathbf{1}\right)}{\mathbf{log(1+g)}} \quad 2.13$$

where:

a = the present age of the connection in years;

g = the estimated annual traffic volume growth rate in percentage terms; and

$[(\text{ADTT})_{SL}]_a$ = the average number of trucks per day in year a.

The resistance factors were subsequently re-evaluated, and an additional level of evaluation was added as shown in Table 2.4:

1. Minimum (probability of failure of 5%);
2. Evaluation 1 (probability of failure of 16%);
3. Evaluation 2 (probability of failure of 33%); and
4. Mean (probability of failure of 50%).

Table 2.4 - Resistance factor (R_R) for NCHRP 12-81 (Bowman et al. 2012).

AASHTO Fatigue Category	**R_R**			
	Minimum Life	**Evaluation 1 Life**	**Evaluation 2 Life**	**Mean Life**
A	1.0	1.5	2.2	2.9
B	1.0	1.3	1.7	2.0
B’	1.0	1.3	1.6	1.9
C	1.0	1.3	1.7	2.1
C’	1.0	1.3	1.7	2.1
D	1.0	1.3	1.7	2.0
E	1.0	1.2	1.6	1.6
E’	1.0	1.3	1.6	1.9

2.5.4 Probabilistic Approach

Uncertainty in material strength, section dimensions, loading, bridge response, and many other sources, makes estimating the remaining fatigue life of a detail on a bridge very challenging. Structural reliability is a method that can characterize the probability of failure with consideration of the uncertainty involved. This method has been used more recently in a number of different applications. CSA S6-14 (CSA, 2014) and AASHTO’s LRFD specifications (AASHTO, 2017) use structural reliability to develop appropriate load and resistance factors so that a consistent level of safety is maintained. Chung (2004), Orcesi et al. (2010), and Bocchini and Frangopol (2011) used reliability concepts to determine an optimal schedule for bridge inspections. This method involved setting a target reliability and optimizing the inspection interval in terms of the cost of repairs, inspections, and failure. The result was a schedule that

was often irregular, as opposed to the typical two or four-year intervals. Probabilistic methods were used in the fatigue evaluation of a bridge in Michigan by Szerszen et al. (1999). These researchers found that in-situ strains were quite low, which in turn caused a high reliability index and a long remaining fatigue life. Kim et al. (2001) applied a probabilistic model to a railway bridge fatigue evaluation and compared it to a deterministic model. In this study, since the deterministic model only considered a single probability of failure, they could only be compared at that data point. The deterministic approach was found to result in a 10-20% longer fatigue life.

The NCHRP Project 12-28(03) by Moses et al. (1987) developed an approach that provides a consistent level of reliability for typical assortments of bridges under certain conditions. In cases where unique geometry or loading exists, a more general probabilistic method can be applied.

To solve for the remaining fatigue life, a limit state function (g(F)) must be used, as shown in Equation 2.14, which is modelled using a lognormal distribution function:

$$\mathbf{g(F)} = \mathbf{\ln\left(\frac{\Delta \times A}{S_r^3 \times N_b(t)}\right) = \ln(1) = 0} \qquad 2.14$$

where:

$g(F) =$ uncertainty model for the fatigue limit state function;

Δ = Palmgren-Miner's critical damage index (resistance); and

$N_b(t)$ = number of accumulated cycles at bridge in year t corresponding to a stress range S_r (loading).

In this approach, lognormal distributions are used for the random variables (Δ, A, S_r, and $N_b(t)$) and since fatigue damage is characterized by both stress and the number of cycles, these two variables can be combined into a single variable ($d_{tot}(t)$):

$$\mathbf{d_{tot}(t) = S_r^3 \times N_b(t)} \qquad 2.15$$

where:

$d_{tot}(t) =$ total accumulated damage at time t.

Furthermore, Palmgren-Miner's critical damage index (Δ) is assigned as a random variable to account for the uncertainty in using that rule. It can also be modelled using a lognormal distribution with a median value of (x_Δ) of 1.0 and a coefficient of variation (δ_Δ) of 30% (Wirsching, 1984). The lognormal parameters can be calculated using Equation 2.16 and Equation 2.17:

$$\mathbf{\lambda_\Delta = \ln(x_\Delta)} \qquad 2.16$$

$$\zeta_{\Delta} = \sqrt{\ln\left(1 + \delta_{\Delta}^{2}\right)} \quad 2.17$$

where:

$x_{\Delta} =$ median value of Δ; and

$\delta_{\Delta} =$ coefficient of variation of Δ.

The variation in the fatigue constant (A) from Equation 2.14 was determined from test results. The variation in fatigue constant, along with the derived parameters for a lognormal distribution are summarized in AASHTO's Manual for Bridge Evaluation (2011) and shown in Table 2.5.

Table 2.5 - Variation in fatigue constant (A) and derived parameters for a lognormal distribution (Fasl et al., 2013)

AASHTO Fatigue Category	**Fatigue Constant**		**σ_A**	**Parameters for lognormal distribution**	
	A (code value)	**μ_A (mean Value)**		**λ_A**	**ζ_A**
A	$250x10^8$	$698x10^8$	1.66	10.84	0.22
B	$120x10^8$	$235x10^8$	1.40	10.37	0.15
B'	$61x10^8$	$145x10^8$	1.54	10.16	0.19
C	$44x10^8$	$59x10^8$	1.16	9.77	0.06
C'	$44x10^8$	$59x10^8$	1.16	9.77	0.06
D	$22x10^8$	$35x10^8$	1.26	9.54	0.10
E	$11x10^8$	$17x10^8$	1.26	9.24	0.10
E'	$3.9x10^8$	$9.9x10^8$	1.59	8.99	0.20

The cumulative fatigue damage can be calculated using Equation 2.18 (assuming that the annual traffic volume grows geometrically at a constant rate):

$$d_{tot}(t) = \mu_{d(1)} \frac{(1+r)^t - 1}{r} \quad 2.18$$

where:

$\mu_{d(1)} =$ mean damage in first year of service; and

t = year evaluated.

Alternative traffic growth models can be substituted into this equation because the total damage each year has to be calculated. The mean damage from the current year (k) can be

obtained from field measurements, and can be used to calculate the mean damage in the first year of service using Equation 2.19:

$$\mu_{d(1)} = \frac{\mu_{d(k)}}{(1+r)^{k-1}} \quad 2.19$$

where:

$\mu_{d(k)}$ = mean damage in year k; and

k = current year.

Assuming that there is no variability in the fatigue damage, the reliability index (β) can be calculated using Equation 2.20:

$$\beta = \frac{\lambda_\Delta + \lambda_A - \ln(d_{tot}(t))}{\sqrt{\zeta_\Delta + \zeta_A}} \quad 2.20$$

The probability of failure can then be calculated using Equation 2.21:

$$P_f = \phi(-\beta) \quad 2.21$$

where:

ϕ () = standard normal cumulative distribution function.

If the index stress range and associated number of cycles is used, rather than calculating the fatigue damage, the reliability index can be calculated using Equation 2.21. Since the stress range is selected explicitly, there is no variability. Therefore, all variability in the fatigue damage calculation is associated with the cumulative number of cycles ($N_b(t)$). Similar to the above, Equation 2.22 can be used to calculate the reliability index, while Equation 2.23 can be used to calculate the mean number of cycles in the first year of service:

$$\beta = \frac{\lambda_\Delta + \lambda_A - 3 \times \ln(S_{ri}) - \lambda_{Nb(t)}}{\sqrt{\zeta_\Delta{}^2 + \zeta_A{}^2 + \zeta_{Nb(t)}^2}} \quad 2.22$$

$$\mu_{Nb(t)} = \frac{\mu_{Nb(k)}}{(1+r)^{k-1}} \quad 2.23$$

where:

$\lambda_{Nb(t)}$ = parameter for the lognormal distribution for $N_b(t)$;

$\lambda_{Nb(t)} = \ln(\mu_{Nb(t)}) - \frac{\zeta_{Nb(t)}^2}{2}$

$\zeta_{Nb(t)}$ = parameter for the lognormal distribution for $N_b(t)$; and

$\zeta_{Nb(t)} = \sqrt{ln\left(1 + \left(\frac{\mu_{Nb(t)}}{\sigma_{Nb(t)}}\right)^2\right)}$.

The notional probabilities of failure for various reliability indices based on the normal probability curves used in CSA S6-14 are summarized in Table 2.6. If the load and resistance factors in CSA S6-14 are followed during design, a reliability index of 3.5 is achieved. This reliability index is considered adequate for the structure to achieve a 75-year design life.

Table 2.6 - Equivalent probabilities of failure and reliability indexes (CSA, 2014)

Probability of Failure, Pf	**Reliability Index, β**
2.3×10^{-2} or 1:44	2.0
1.2×10^{-2} or 1:81	2.25
6.2×10^{-3} or 1:160	2.50
2.8×10^{-4} or 1:360	2.75
1.4×10^{-4} or 1:740	3.00
5.6×10^{-4} or 1:1,800	3.25
2.3×10^{-4} or 1:4,300	3.50
8.8×10^{-5} or 1:11,000	3.75
3.2×10^{-5} or 1:31,500	4.00
1.1×10^{-5} or 1:93,500	4.25
3.4×10^{-6} or 1:294,000	4.50

2.6 Summary

Structural fatigue is a primary cause of failures in metallic structures. As existing bridge infrastructure ages, the determination of the remaining fatigue life will continue to challenge engineers. There are two primary methods of evaluating fatigue, a stress-based approach, and a linear elastic fracture mechanics approach (Ye, 2014). In the more commonly employed stress-based approach, Palmgren-Miner's rule is used to relate the variable amplitude stress found on bridges to the constant amplitude fatigue data that the specifications were derived from, and a rainflow method of counting stress cycles may be implemented according to ASTM E1049.

To determine stress range magnitudes and load cycles present at fatigue prone details, structural health monitoring is becoming an increasingly common method. This method is becoming more accepted since it reduces the uncertainty associated with code-based structural analysis alone. In addition, it can be used to characterize structural behaviour such as lateral load distribution, dynamic load influence, and degree of composite action.

A substantial amount of research into the fatigue resistance of bridges by the NCHRP in the 1970's and 1980's led to the specifications and evaluation procedures available today. Of the methods available for determining the remaining fatigue life of a structure, three were implemented in Chapter Four:

- Deterministic method – Equation 2.10;
- AASHTO's method – Equation 2.14; and
- Probabilistic method – Equation 2.21.

CHAPTER 3. FIELD MONITORING OF THE DIEFENBAKER BRIDGE

3.1 Geometry and Traffic Estimate

The Diefenbaker Bridge carries both the northbound and southbound lanes of Highway No. 2 over the North Saskatchewan River, in Prince Albert, Saskatchewan, Canada. Constructed in 1959, the bridge consists of two fracture critical superstructures on a shared substructure, as shown in Figure 3.1. Each direction of traffic includes two lanes for a total travelled width of 7.3 meters per superstructure, and each with seven spans for a length of 304.4 meters. The bridge deck, piers and abutments are built with cast-in-place concrete, while the girders are welded steel I-sections.

Figure 3.1 - Overview of Diefenbaker Bridge looking southwest over Prince Albert

The end spans are 35.81 meters in length, with the middle five spans being 46.56 meters; the spans are continuous over the piers. The welded plate girders are transversely stiffened with a 1/2” x 8” (12.7 mm x 203.2 mm) steel plates, and longitudinally stiffened with 3/8” x 4” (9.5 mm x 101.6 mm) steel plates on the exterior faces along their entire length. As shown in Figure 3.2, the lateral bracing consists of ST6 x 13.5 (ST150 x 20.1) steel members, and the transverse

bracing consists of 2 – 5” x 3” x 5/16” (127 mm x 76.2 mm x 7.9 mm) steel angles. The lateral bracing and bottom chords of the transverse bracing are bolted to the 3/8” (9.5 mm) steel gusset plate, and the plate is welded to the girder web with a 3/8” (9.5 mm) fillet weld.

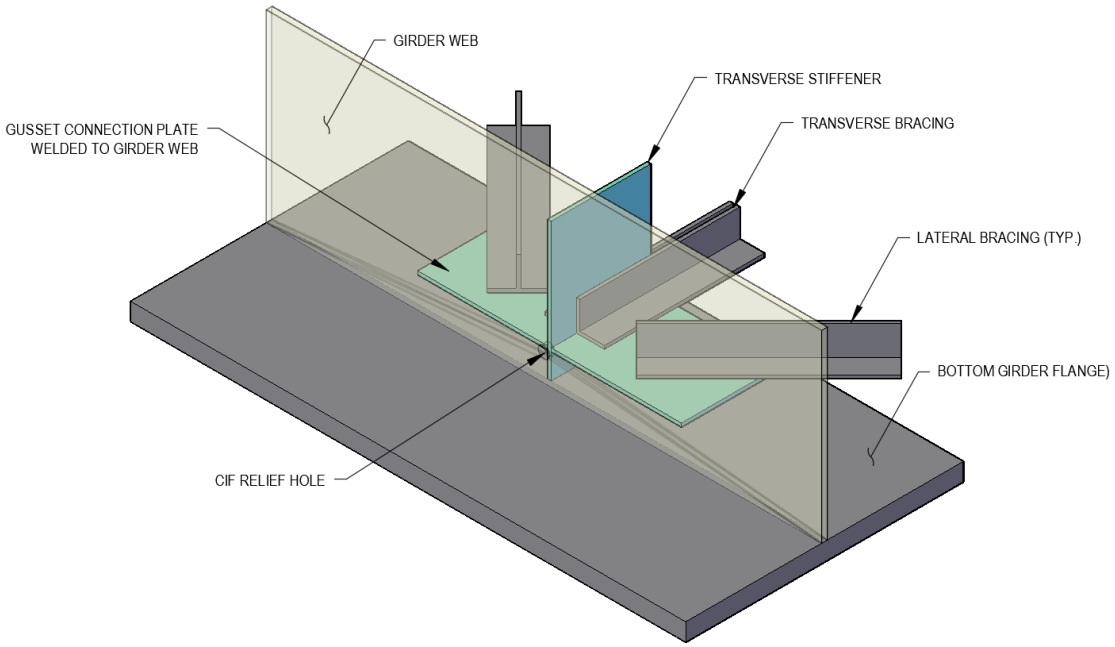

Figure 3.2 - Schematic of the bracing connection

Shear studs were not installed along the top flange of the girders and, as such, no composite action between the deck and the girders was accounted for in the design.

Based on the 2015 bridge inspection data, the AADT for this site is 23,588 vehicles per day (Stantec, 2015). Stantec’s 2013 Prince Albert Area Second Bridge River Crossing Study (Stantec, 2013), confirmed the AADT with an estimate of 22,000 – 24,000 vehicles per day. This report also included an estimate of the fraction of truck traffic at 8%, a crucial piece of data for the fatigue evaluation. Given that the Diefenbaker Bridge is a twinned structure, and that the traffic going northbound does not affect the southbound bridge, and vice versa, the effective AADT for each “bridge” was adjusted by assuming that the northbound traffic equals the southbound traffic. Therefore, the following traffic data was assumed:

- AADT = 11,794 vehicles per direction; and
- 8% Trucks = 944 trucks per direction.

This assumption does not necessarily reflect the true traffic loading in each direction, since it is possible, for example, that the northbound bridge may experience more traffic; however the

southbound bridge may be more heavily loaded. This is a primary uncertainty that in-situ monitoring will help to reduce.

3.2 Condition of Bridge and Characterization of Fatigue Details

From a fatigue perspective, the structural detail being investigated in this research project is the welded connection between the longitudinal girder web and the lateral and transverse bracing connection. This detail was found to have less than five years of remaining fatigue life in the evaluation completed by ISL Engineering in 2016 (ISL, 2016). It is a category E detail according to CSA S6-14 (CSA, 2014) because there is no transition between the gusset plate and the longitudinal girder web (similar to Figure 2.1c). A photograph of this connection can be seen in Figure 3.3, while a schematic is shown in Figure 3.4.

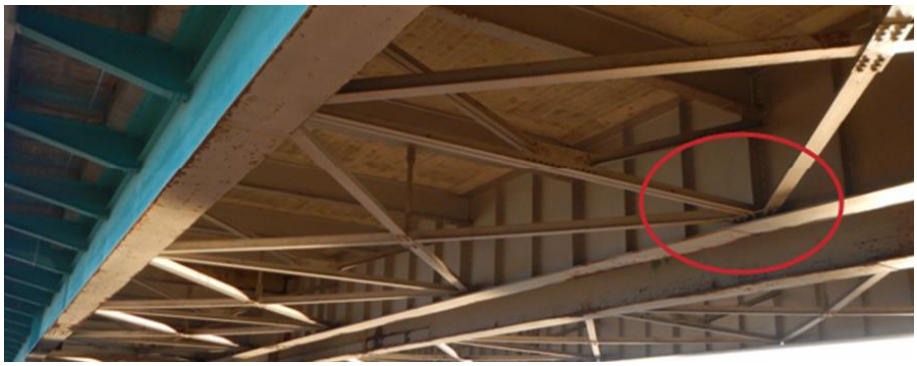

Figure 3.3 - View of superstructure underside showing the fatigue detail being investigated

Because cracks typically initiate in areas of small flaws or imperfections such as bolt holes, welds or changes in cross sections, the termination of the gusset plate weld, as highlighted in Figure 3.5, was determined to be the probable initiation point of a crack. Welds are especially prone to fatigue cracking due to residual stresses remaining in the weld after differential heating and cooling. Flaws can also be introduced when the weld has partial penetration, lack of fusion, and flaws, particularly at the start and stop locations.

Figure 3.4 – Probable crack initiation location on fatigue detail being investigated

During the 2012 Constraint Induced Fracture (CIF) repairs, a 50 mm diameter hole was cored through the weld intersection, and stress risers such as nicks and sharp corners were ground smooth. Since this location was improved through the repairs, this location is no longer considered critical. However, the quality of the weld remains a source of uncertainty in this analysis because an in-depth inspection was not included in the scope of this study. To address this, since the magnetic particle testing of the CIF details revealed no defects on the portion of the welds that were tested (ISL, 2016), it has been assumed for the current study that the weld is intact and free of defects.

Lateral bracing connections to girder webs can be susceptible to distortion-induced fatigue. Distortion-induced fatigue occurs at this detail when out-of-plane web distortions in the gaps between gusset plates occur causing bending stresses. Figure 3.6 shows a schematic of a similar detail with the web distortion exaggerated.

In the case of Diefenbaker Bridge, since the transverse stiffener is connected to the gusset plate and the transverse bracing, and a 50 mm diameter hole core has been drilled through the weld intersection, this detail is much less susceptible to the distortion-induced situation shown in Figure 3.5. While this rigid attachment tends to reduce the magnitude of out-of-plane distortions, it may increase the magnitude of loading because of the increased stiffness of the connection. It is probable that the lateral bracing was designed to interact with the primary girders and, as such, is subjected to the same stress cycles as the girders (NHCRP 335, 1990).

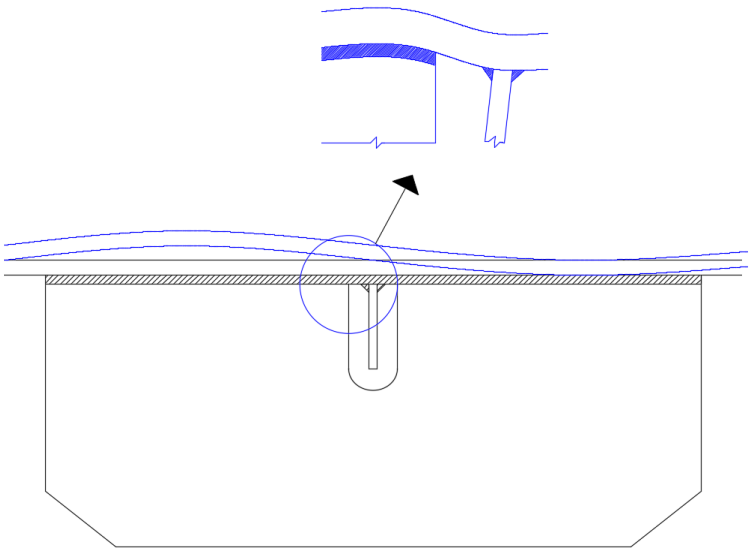

Figure 3.5 - Schematic of typical gusset plate connection detail susceptible to distortion-induced fatigue (adapted from NHCRP 335, 1990)

In situations where distortion-induced fatigue exists, the load-induced fatigue categories in CSA S6-14 are not directly applicable. However, full scale testing on a nearly identical detail to the one being investigated at Diefenbaker Bridge was performed during NCHRP 335 (1990). It was found that the experimental data, which included the effects of both in-plane stresses and out-of-plane stresses, very closely resembled the behaviour of a Category E detail. In fact, despite combined stresses that substantially exceeded the endurance limit for a Category E detail, no cracking was detected on the specimens after a large number of cycles. This result is generally supported by experience with in-service structures, and indicates that the endurance limit may, in fact, be higher than a Category E. For the purposes of this research, however, the detail was conservatively assumed to follow Category E behaviour.

To relate the three-dimensional stress state (as shown in Figure 3.7) to the uniaxial fatigue condition on which the Categories outlined in CSA S6-14 are based, either the maximum distortional energy theorem (i.e., von Mises stress), or the maximum principal stress may be used (Beer et al., 2009). Determining which of these to employ is dependent on the standard being followed, or the specific stress state of the detail. For this analysis, the principle stresses were found to be very similar in magnitude to the von Mises stress. Therefore, the von Mises stress was utilized for the fatigue life evaluation. This theory states that yielding will occur when the distortional strain energy reaches that value which causes yielding in a simple tension test (Beer et al., 2009). The maximum distortional energy theory (i.e., von Mises) applies to ductile, isotropic materials such as steel, that are subjected to complex stress states, and works well with any complex three-dimensional loading condition, regardless of the mix of normal and shear stresses. It has been shown to be a more accurate predictor of the onset of yielding than the maximum shear stress theory proposed by Tresca (Beer et al., 2009). Since the fatigue detail being evaluated is subjected to a complex stress state (as shown in Figure 3.6), the von Mises stress (σ_{vm}) was calculated using Equation 3.1.

$$\boldsymbol{\sigma_{VM}} = \sqrt{\frac{1}{2}\left[\left(\boldsymbol{\sigma_{xx}} - \boldsymbol{\sigma_{yy}}\right)^2 + \left(\boldsymbol{\sigma_{yy}} - \boldsymbol{\sigma_{zz}}\right)^2 + \left(\boldsymbol{\sigma_{zz}} - \boldsymbol{\sigma_{xx}}\right)^2\right] + \mathbf{3}\left(\boldsymbol{\tau_{xy}^2} + \boldsymbol{\tau_{yz}^2} + \boldsymbol{\tau_{zx}^2}\right)} \qquad 3.1$$

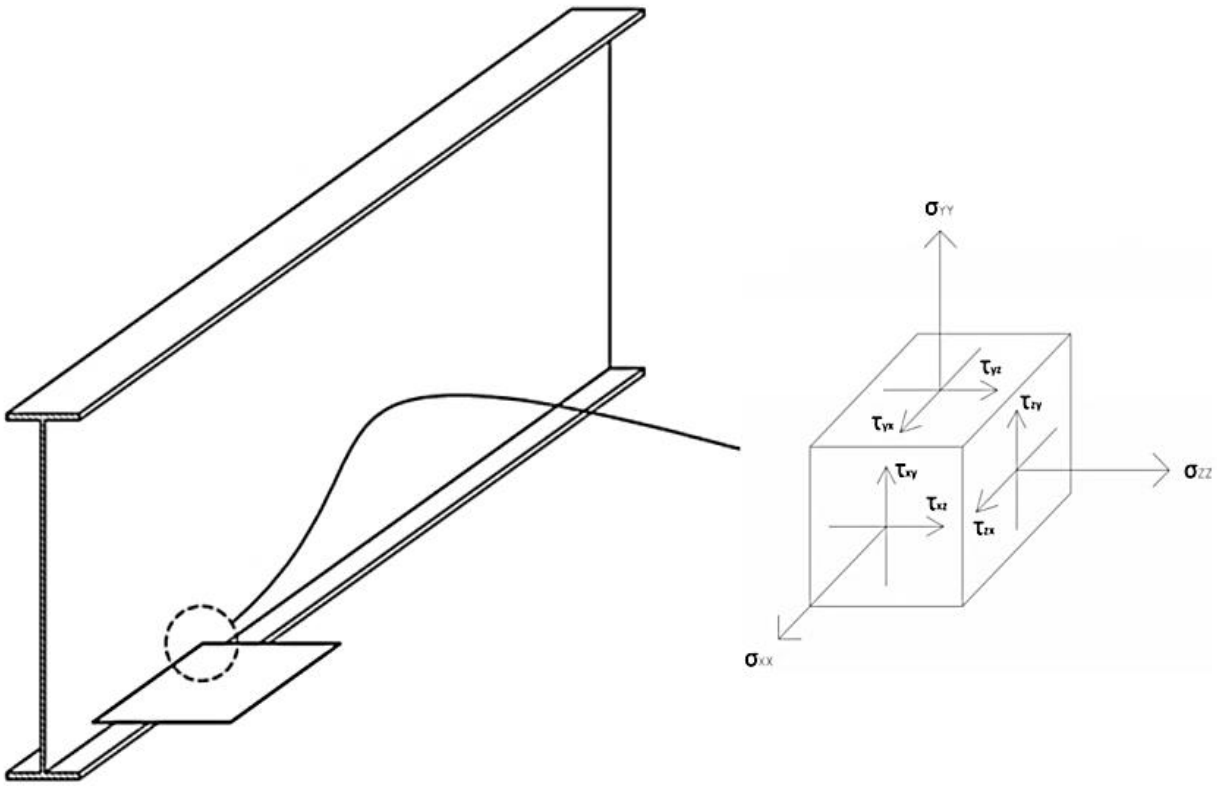

Figure 3.6 - Three-dimensional stress state at point of interest (POI)

3.3 Instrumentation Plan

The primary objective of this monitoring plan was to refine the fatigue life estimate for the horizontal bracing gusset plate connection to the girder web. Given the assumptions made in the 2016 analysis (ISL, 2016), the fatigue life of the detail was deemed to be nearly exhausted, suggesting that costly improvements and repairs were required. By instrumenting the bridge, important data could be collected that could be used to reduce the uncertainty regarding the fatigue-related parameters for the bridge, including:

- Stress Magnitude – by acquiring the actual stresses that are present at the gusset plate, the necessity of weld improvements could be verified. The stress history, and therefore the fatigue life, are highly dependent on the traffic volume and the weight of trucks that cross the bridge. From a historical perspective, this information is very difficult to quantify; however, understanding current loading conditions and their associated stress ranges helped to increase the accuracy of the analysis and reduce the potential for unnecessary repairs and improvements; and

- Stress Distribution and Cycles – in addition to the magnitude of the stresses, the locations of high stress and the number of cycles that occur were established. This narrowed the scope of weld improvements that had to be considered, as the measured data identified which direction, which girders, and which connections were more heavily loaded. This information was also important when determining service life estimates and maintenance plans as it can be used to avoid over-investment in non-essential repairs by allowing a more targeted approach to be taken.

A global approach to stress acquisition was employed so that the structural response across the bridge could be understood on a global scale (i.e., stress distribution along girders). As shown in Figures 3.7, sensors were strategically placed along Span Four, such that equipment and installation effort was minimized without compromising the quality of data required to perform the fatigue analysis. For simplicity, the instrumentation plan can be broken down into two categories: girder instrumentation and connection instrumentation.

A full set of as-built drawings detailing the instrumentation plan can be found in Appendix A. These drawings have more information on the electrical system used and how the equipment in the cabinet was organized. The drawings contain an explanation of the naming conventions used (i.e. G3-S4-A1-TSG means Girder 3-Span 4-Connection A1-Top Strain Gauge, etc.), and have a photograph of each sensor that was installed.

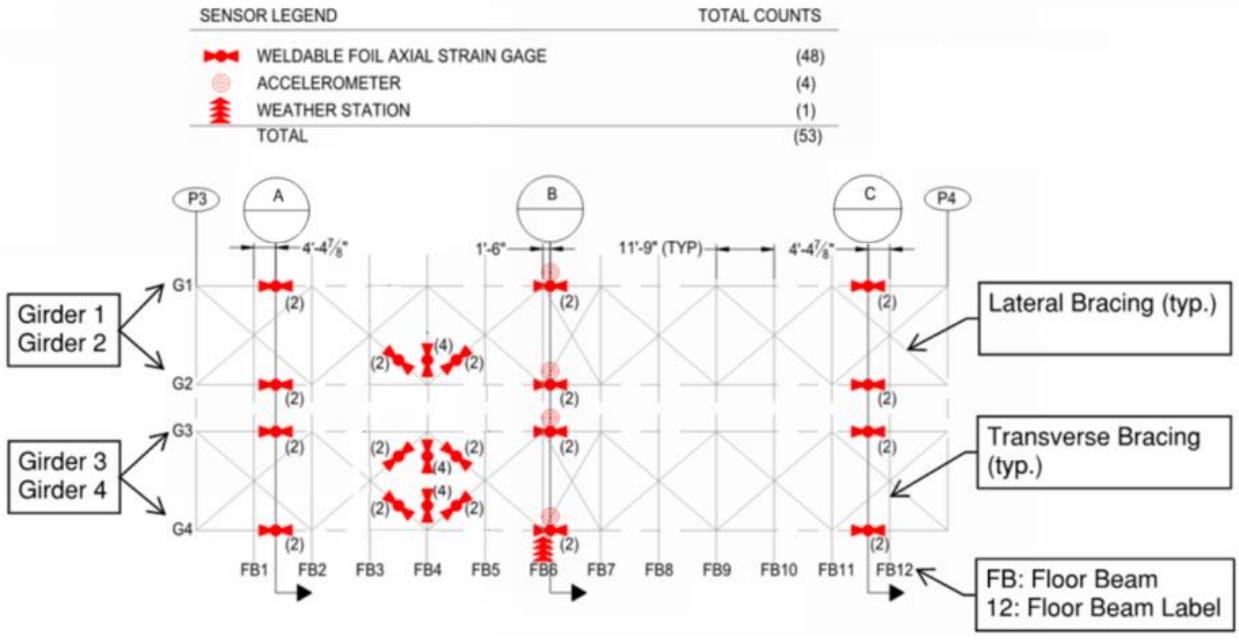

Figure 3.7 - Plan view of span 4, showing the instrumentation layout

3.3.1 Girder Instrumentation

The purpose of the girder instrumentation was to provide insight into the global behaviour of the bridge. Uniaxial strain gauges were installed in the longitudinal direction on the top and bottom of all four girder webs at three cross sections as shown in Figures 3.7 and 3.8.

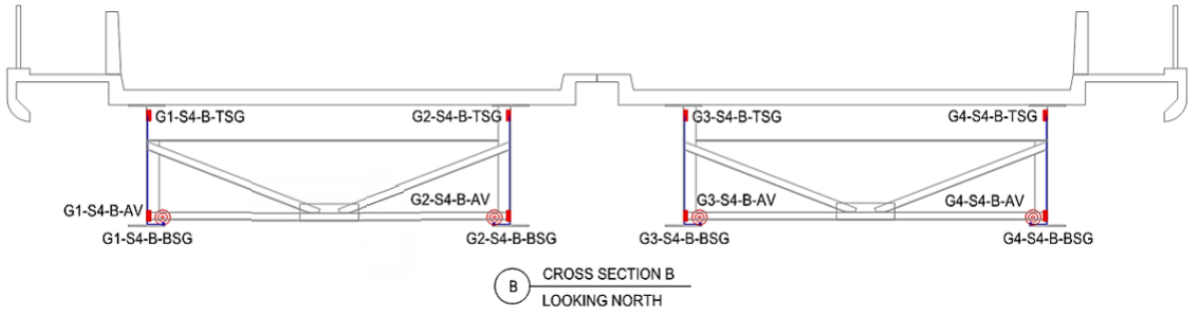

Figure 3.8 - Cross Section B, showing the locations of the strain gauges and accelerometers

These sensors were strategically located away from the anticipated neutral axis of the girder to maximize the strain measurements, and therefore the signal-to-noise ratios. The steel girders were designed without shear connection to the deck, as shown in Figure 3.9. Since there is no mechanical connection between the steel girders and the concrete deck, the structural behaviour was considered to be non-composite for ultimate strength purposes. However, it is recognized that composite action is possible through interface shear friction, particularly under service loads, but it is a conservative approach to neglect this action since it is challenging to quantify without the benefit of instrumentation. With non-composite action, the neutral axis would be expected to fall at the mid-height position of the girder web. The actual location, though, was determined from strain measurements, providing an indication of the actual extent of in-service composite behaviour.

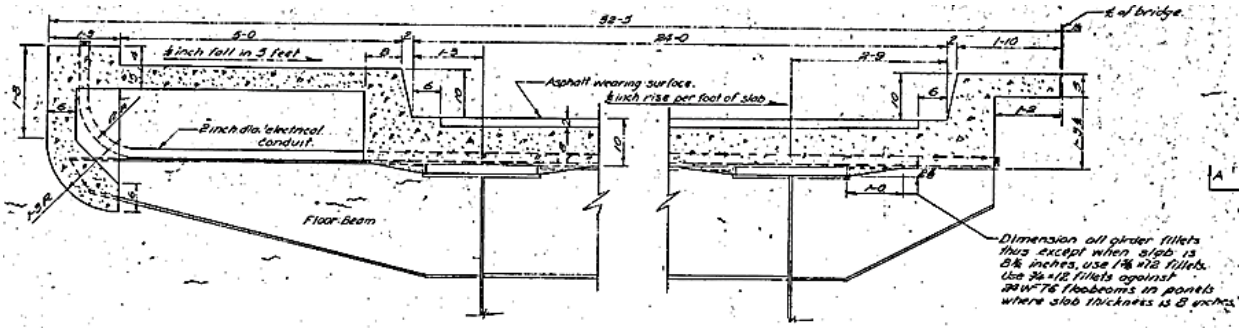

Figure 3.9 - Girder to deck connection (Typ.) taken from as-built drawings (Saskatchewan Ministry of Highways and Infrastructure, 1959)

Cross Sections A and C were located close to Piers Three and Four, respectively, to capture the behaviour within the negative moment regions. Cross Section B was located at midspan of Span Four to capture the behaviour in the positive moment region.

Four uniaxial accelerometers were also placed on each girder at Cross Section B, as shown in Figure 3.10, and oriented to measure vertical acceleration, to identify the span's natural frequency and deflections. Additionally, temperature and humidity gauges were installed so that bridge response could be correlated to atmospheric conditions.

The data collected from these instruments were used to investigate the behaviour of the structure on a global scale. Characteristics such as lateral load distribution, bearing restraint, dynamic load influence, and degree of composite action were investigated.

A photograph of two of the girder strain gauges is shown in Figure 3.10. The gauges were coated with a zinc-rich paint to enhance durability.

Figure 3.10 – Photograph of installed strain gauges on Girder 1 (Typ.)

3.3.2 Connection Instrumentation

The purpose of the connection instrumentation was to acquire actual data on the stress distribution and magnitudes within the structural fatigue detail. Uniaxial strain gauges were installed on the lateral and transverse horizontal bracing members that are connected to the

gusset plate. The gauges were installed at the locations shown in Figure 3.11 to maximize response levels if any bending occurred. The T-sections in this figure are the lateral braces, while the double angle sections are the transverse bracing members. Figure 3.12 shows a typical installation of the strain gauges on the transverse bracing. As shown in Appendix A on Sheet No. 5, the lateral brace and transverse brace gauges were installed 1.95 m and 0.914 m away from the gusset plate, respectively (measured along the member axis).

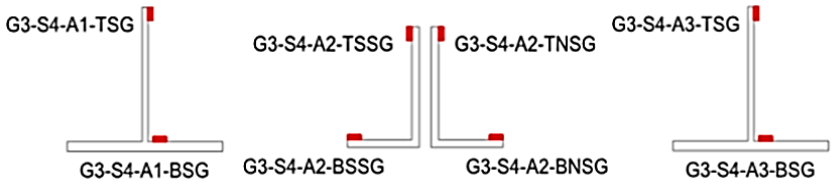

Figure 3.11 – Cross section of the lateral braces (T-sections) and transverse braces (double angles) showing the locations of the strain gauges

The three instrumented connections, as shown in Figure 3.7, were chosen based upon the structural analysis done by ISL Engineering in 2016. The connections on Floor Beam Four of Span Four, were found to exhibit the highest stress ranges, and were therefore taken to be the governing fatigue location on the structure.

Using the strain measurements in the bracing elements, stresses in the gusset plate were calculated, as well as how often stresses of various amplitudes occurred. By basing the fatigue life evaluation on real data, the uncertainty involved in the calculation could be reduced, and a more refined estimate provided. These data could also be used to investigate behaviour on the global scale. For example, by examining the force amplitudes in the lateral bracing, bearing restraint at Piers Three and Four could be inferred; in addition, any secondary effects, or out-of-plane distortions, could be identified.

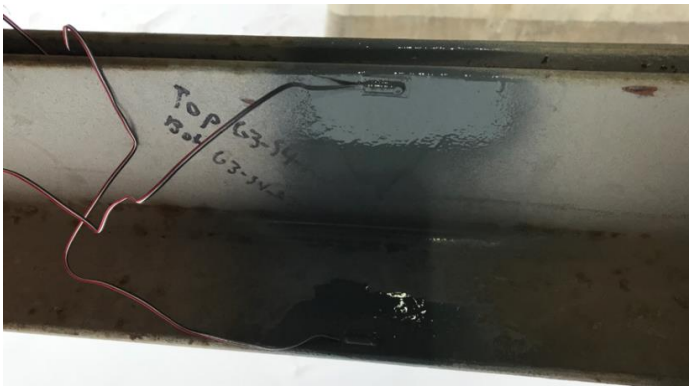

Figure 3.12 – Strain gauges on the transverse bracing as viewed from above

3.4 Sensors and Data Acquisition System

Three types of sensors were used: strain gauges, accelerometers and a weather station. The strain gauges were 350 Ohm weldable axial foil gauges supplied by HPI Strain Gages (Massachusetts, United States of America), as seen in Figure 3.15. These waterproof gauges were selected because they are specifically designed to evaluate and monitor live load stresses on bridges (https://hitecprod.com/products/waterproof-weldable/, 2018). They came pre-wired and protected and featured a stainless steel shim that can be easily spot welded with any conventional capacitive discharge spot welder. The shim size was 21.6 mm by 10.2 mm and the gauge length was 3.1 mm. Each strain gauge was accompanied by a 350 Ohm Quarter Arm Completion Unit that is produced by Bridge Diagnostics Inc. (Colorado, United States of America (BDI)). These units complete the circuit close to the in-place sensor. This approach reduces lead wire effects and improves noise reduction, resulting in enhanced data quality (https://bditest.com/product/sensors/strain-sensors/foil-gage-completion-module/, 2018). Figure 3.13 shows an installed foil strain gauge and its associated quarter arm completion unit. The quarter arm completion units were attached to a U-bracket and then clamped to nearby flanges and gusset plates.

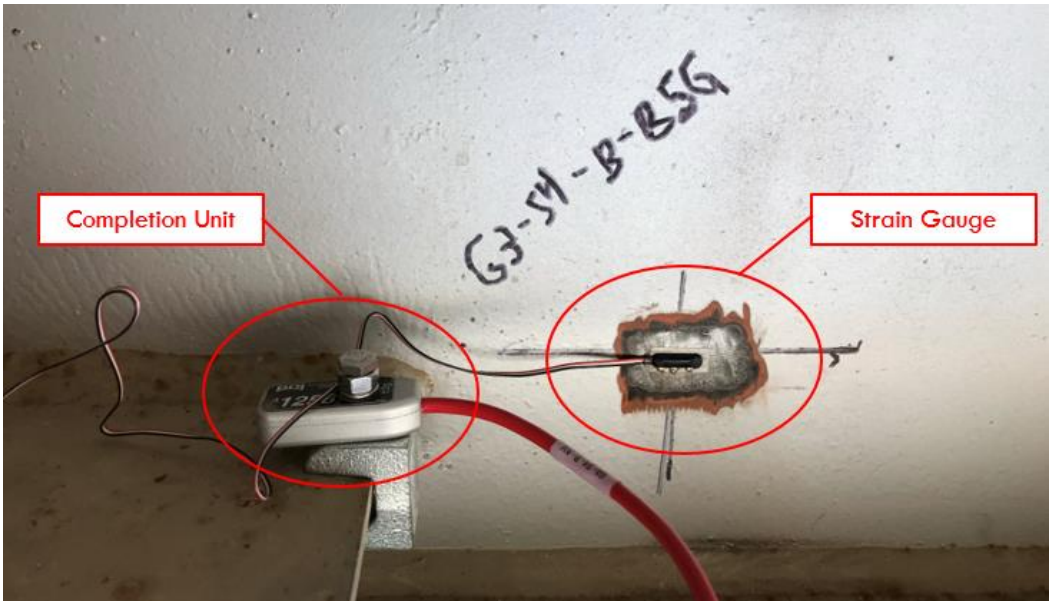

Figure 3.13 – Photograph of the foil strain gauge and completion unit (Typ.)

Four UA512 uniaxial accelerometers supplied by BDI were installed across Section B. One accelerometer was placed on each girder at locations shown in Figure 3.16 and positioned to measure vertical accelerations.

Lastly, a Vaisala INTERCAP Humidity and Temperature Probe HMP60 was installed above the primary housing cabinet just outside of the sidewalk. This temperature station measured relative humidity from 0-100% (±5%) and temperatures from -40°C to +60°C (±0.5°C).

All sensors were routed using insulated wire to node cabinets located under the bridge, then finally to a data logger secured to the outside of the pedestrian walkway. The wiring was run as shown in Figures 3.14 and 3.15.

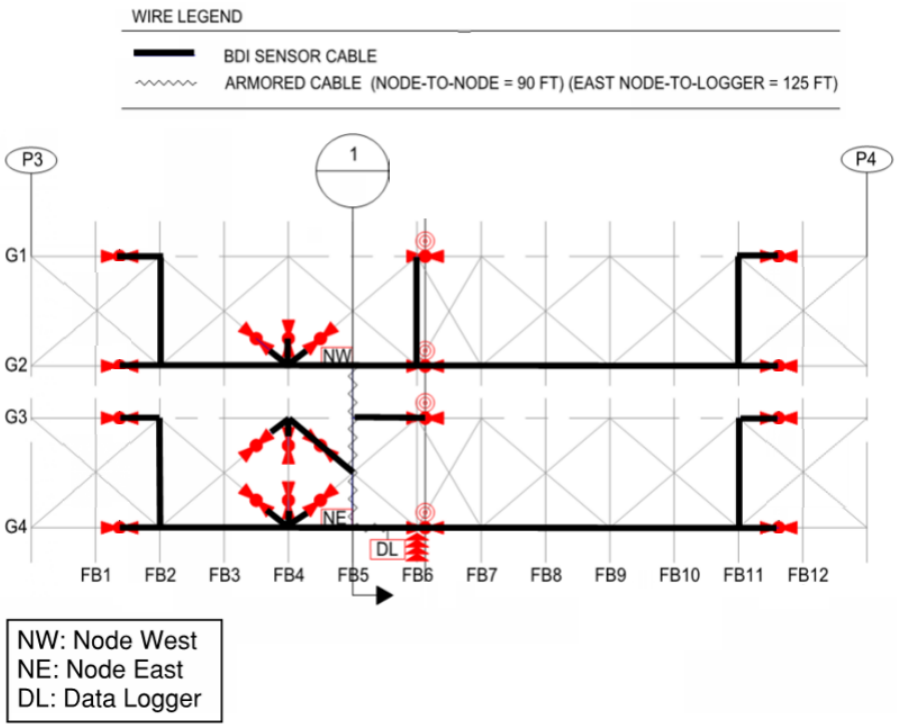

Figure 3.14 - Schematic of Sensor Wiring

Figure 3.15 shows how the wire was strung between cabinets, as well as the locations of the cabinets on the structure. Since this installation was only temporary, the cabinets were secured using clamps that could be easily removed.

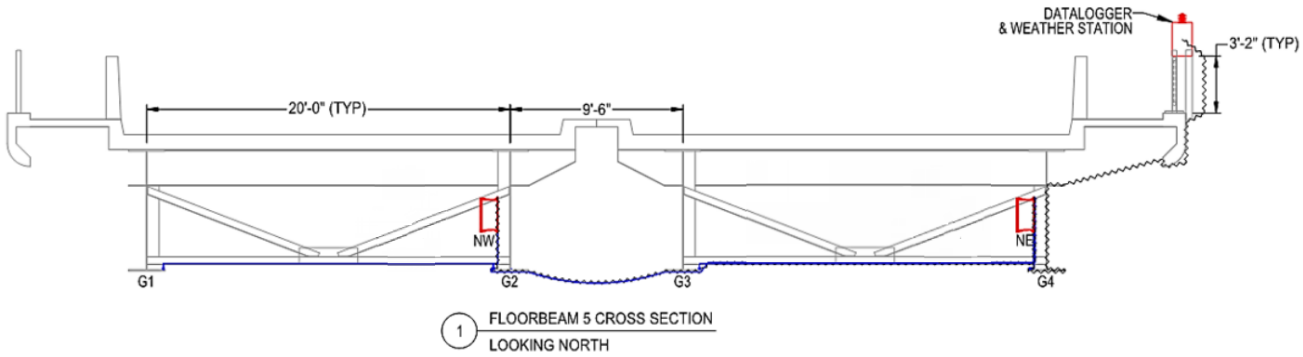

Figure 3.15 - Elevation view of wiring and cabinet locations

Figure 3.16 shows a photograph of the primary cabinet that held the data logger and the weather station. It was secured outside of the pedestrian sidewalk to allow for easy access for the project personnel but was locked to prevent vandalism or theft.

Figure 3.16 - Primary cabinet located just outside of sidewalk railing

Installation of the sensors was completed during the week of November 13th, 2017. A fully certified rope access team provided by BDI accessed the underside of the superstructure via the east sidewalk without traffic lane closures.

3.5 Data Acquisition

3.5.1 Calibration Data

Calibration data were acquired by removing all traffic from the structure and driving a truck of known load across in a controlled manner. Collaboration between the City of Prince Albert, the Ministry of Highways, and the research team was critical in performing these tests in a safe and controlled manner. The truck shown in Figures 3.17 and 3.18 was supplied by the Ministry of Highways and was used to perform the calibration loading. The axle loading was measured by a scale provided by the Ministry of Highways. Traffic accommodation was performed by the City of Prince Albert. Accommodating traffic during this testing was challenging and, as such, only a limited number of trials could be completed. A minimum of two trials per lane with controlled speeds were completed, with one additional slow median lane trial completed per direction. Completing at least two trials per test allowed the team to validate the quality of the data.

Data were acquired during the slow speed passes (10 km/hr) at 50 Hz and at 100 Hz for the high speed passes (50 km/hr). To clarify, at 50 Hz data are collected at 50 samples per second, or one sample every 0.02 seconds. By performing multiple passes in each lane and at each speed, the quality of the data could be verified. Data quality indicators included reproducibility, elastic behaviour (i.e. strains returning to zero after run), symmetry of responses, and lack of noise. With traffic removed completely from the bridge, controlled loading was implemented according to Table 3.1.

Table 3.1 - Summary of Calibration Loading

Position on Bridge	Speed	Number of Trials
Southbound Barrier Lane	10 km/hr	2
Southbound Barrier Lane	50 km/hr	2
Southbound Median Lane	10 km/hr	3
Southbound Median Lane	50 km/hr	2
Northbound Barrier Lane	10 km/hr	2
Northbound Barrier Lane	50 km/hr	2
Northbound Median Lane	10 km/hr	3
Northbound Median Lane	50 km/hr	2

The data from this calibration stage provided the baseline response characteristics of the structure that were required to quantify various parameters such as lateral load distribution, dynamic load effect, degree of composite action with the deck, and bearing restraint. Since traffic did not affect the bridge's behaviour, the aforementioned characteristics were more easily analyzed.

Figure 3.17 - Calibration vehicle

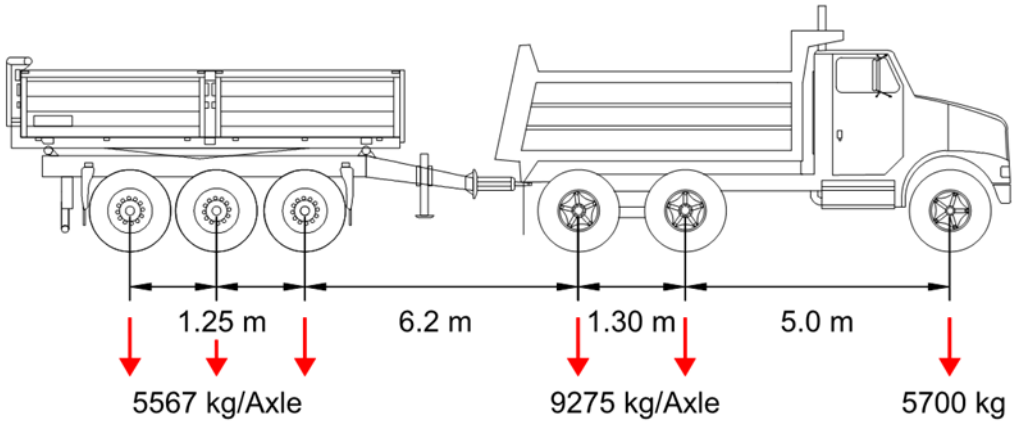

Figure 3.18 - Calibration vehicle load and axle distribution

3.5.2 Trend Data

Trend data can be used to establish trends over a long period of time. Data were continuously collected at 50 Hz and the trend data included the minimum response, maximum response, and average response for every 30 seconds.

3.5.3 Rainflow Data

There are two primary factors that affect the fatigue life of the structure: stress magnitude and the number of cycles. Unfortunately, these are also the two parameters with the largest uncertainties when evaluating the remaining fatigue life of a structure. To reduce this uncertainty, the data collection unit was programmed to keep track of specified stress range occurrences. The cycle counting algorithm was set up according to the rainflow counting method described in ASTM E1049 and summarized in Section 2.2.3. This method is well suited for variable amplitude fatigue analysis since it identifies stress ranges associated with closed-loop hysteresis. This means that the stress cycles are compatible with the constant amplitude fatigue tests that were used to develop the code values. The ranges of stress were based on the maximum values experienced during the calibration loading. Recognizing that larger stress ranges may be experienced, the ranges were set up in 5 MPa increments up to 30 MPa, as shown in Figure 3.19. Small ranges of less than 2.5 MPa were ignored, as this range would experience a large number of cycles due to the presence of noise and would have a negligible effect on fatigue life. The rainflow method also keeps track of the median stress on which the stress cycle is centered. For example, if a stress ranged from 20 MPa to 40 MPa, a range of 20 MPa was recorded with a median value of 30 MPa. This allowed the team to understand if the structural member was loaded primarily in tension or compression and at what magnitude. The histogram in Figure 3.19

shows the rainflow data for the bottom gauge on Girder 2 at Cross-Section B (as shown in Figure 3.16) for the full month of May 2018.

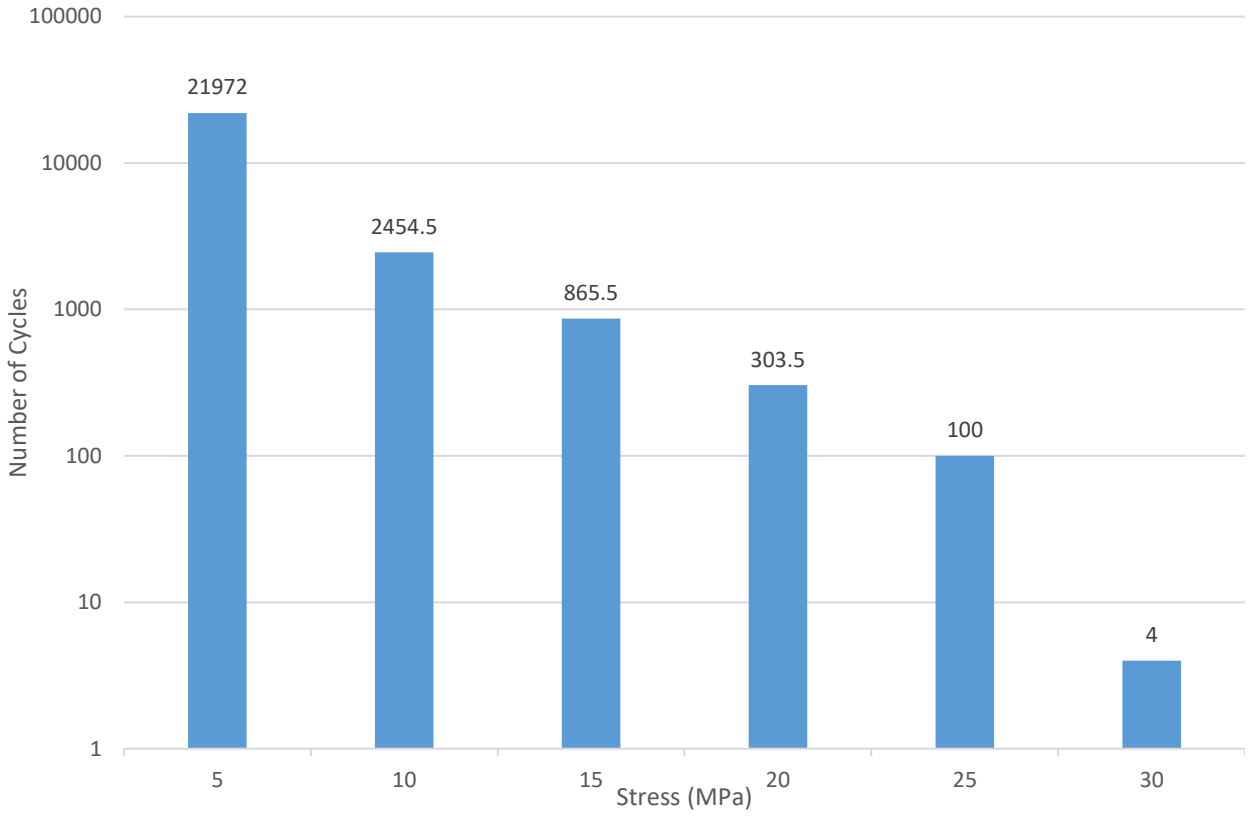

Figure 3.19 - Rainflow data for G2-S4-B-BSG in May 2018

The cycles were counted and reported daily. These data showed the actual stress ranges being experienced by the various components of bridge and were crucial in refining the remaining fatigue life estimation. Data could be remotely accessed via the computer in the primary cabinet.

3.6 Duration of Monitoring

Data were acquired from November 2017 until June 2018. This six-month duration allowed for the comparison of fatigue damage on a daily and monthly basis. All rainflow data is included in Appendix B.

CHAPTER 4. DATA ANALYSIS AND INTERPRETATION

4.1 Introduction

Given the large volume of data that were recorded, proper management of this data was crucial to project success. With over 5 billion cells of data, it was easy to become overwhelmed since familiar software such as Microsoft Excel cannot handle this amount of data without some assistance. Therefore, the following sections summarize the strategies employed to manage this data, and convert it into a useful format that could be used for analysis.

4.2 Programming

The data collected from the sensors were stored using a Technical Data Management System (TDMS) file format since it was easily exchangeable into other formats, inherently structured, and high speed streaming capable (Taken from https://www.ni.com/white-paper/3727/en/, 2018). TDMS files can be used with many different software packages, but Microsoft Office 365 Excel was selected to be the primary software for viewing and manipulating the data. To open the files Excel format, an add-in was downloaded called "TDM Excel Add-In". The TDMS files were opened and saved into a common Excel file format. This was done for all calibration data and all rainflow data.

Since a primary objective of this research was to compare the fatigue response on a daily and monthly basis, the rainflow data (which was reported daily) for each sensor was stored and compiled in the following categories:

- Monthly (i.e. – January, February, March…June); and
- Daily (i.e. – Sunday, Monday, Tuesday…Saturday).

Python 3.7.1. was used to write a program that combined the numerous Excel files and Excel sheets so that a single file could be created with the data of interest. The Anaconda 3.0 Package (https://www.anaconda.com/) was utilized since it contained the necessary modules required to work with Excel. Python was selected because it is an open source programming language with extensive online resources.

4.3 Rainflow Data

With the rainflow data organized into monthly and daily bins using the process described above, the quality of the data was reviewed. Obvious outliers were identified by comparing the distribution of cycles within each bin between sensors. For the purpose of comparing methods of

fatigue life evaluation, sample data from May 2018 can be seen in Tables 4.1 and 4.2. The complete set of data can be found in Appendix B. Data from the bottom web strain gauge on Girders 1 through 4 at Cross Section B and the Connection 1 strain gauges were selected for presentation here since they represent what is considered to be the most reliable data.

Table 4.1 - Rainflow data from May 2018 for Girder Sensors at Cross Section B

Girder Sensors	Number of Cycles					
	Stress Range (MPa)					
	5	10	15	20	25	30
G4-S4-B-BSG	24,733	3,754	1,341	736	570	269
G3-S4-B-BSG	23,328	2,582	1,292	629	43	16
G2-S4-B-BSG	21,972	2,455	866	304	100	4
G1-S4-B-BSG	25,446	3,230	878	278	152	113

The number of cycles at Connection 1 also correlated well to both the AADTT, and the number of cycles observed at Cross-Section B.

Table 4.2 – Rainflow from data from May 2018 for Connection 1

Connection 1 Sensors	Number of Cycles					
	Stress Range (MPa)					
	5	10	15	20	25	30
G2-S4-A1-BSG	24,244	2,826	806	319	171	79
G2-S4-A1-TSG	3,662	189	13	7	9	3
G2-S4-A2-BSSG	19,321	550	96	18	11	4
G2-S4-A2-TSSG	20,924	3,206	25	3	0	1
G2-S4-A2-BNSG	6,116	435	19	16	6	2
G2-S4-A2-TNSG	3,345	39	12	1	3	9
G2-S4-A3-BSG	12,874	2,017	369	225	55	1
G2-S4-A3-TSG	5,266	416	25	3	6	8

The number of cycles recorded at Cross-section B (across all four girders) was as expected, given the AADTT of 944 trucks per day, as determined by a traffic study performed by MHI. Over 31 days, approximately 30,000 cycles would be expected.

4.4 Finite Element Model

The gusset plate connection to the girder web has forces applied in varying directions causing a three-dimensional stress state. As shown in Figure 4.1, the potential sources of the stress include forces coming from:

- The bottom leg of the lateral bracing;
- The bottom leg of the transverse bracing;
- The top leg of the transverse bracing;
- Flexural stress in the girder; and
- Shear stress in the girder.

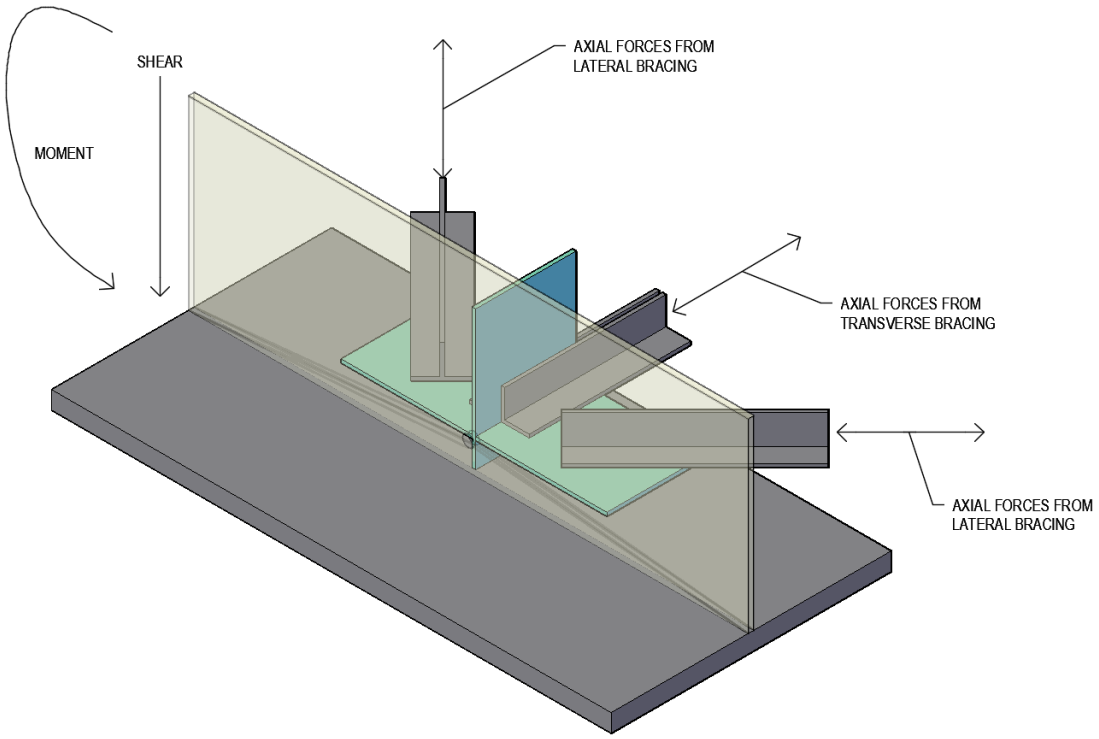

Figure 4.1 - Forces causing three-dimensional stress state

As mentioned in Section 3.2, the location on the gusset plate that is expected to fail first is the weld termination point. From this point forward, the weld termination will be referred to as the point of interest (POI). Since the POI could not be instrumented directly, the stress state at that location had to be calculated based on the incoming forces from the elements listed above.

Adding to the challenge, the number of cycles at this location had to be inferred based on the varying stresses and cycles experienced by the connecting element. For example, if the lateral brace contributed 1000 cycles at the 25 MPa stress range, and the transverse brace contributed 1500 cycles at the 10 MPa stress range, how many cycles at what stress range were experienced at the POI? To overcome this challenge, the number of cycles occurring at G2-S4-B-BSG were compared to the cycles at G2-S4-A1-BSG, as shown in Figure 4.2.

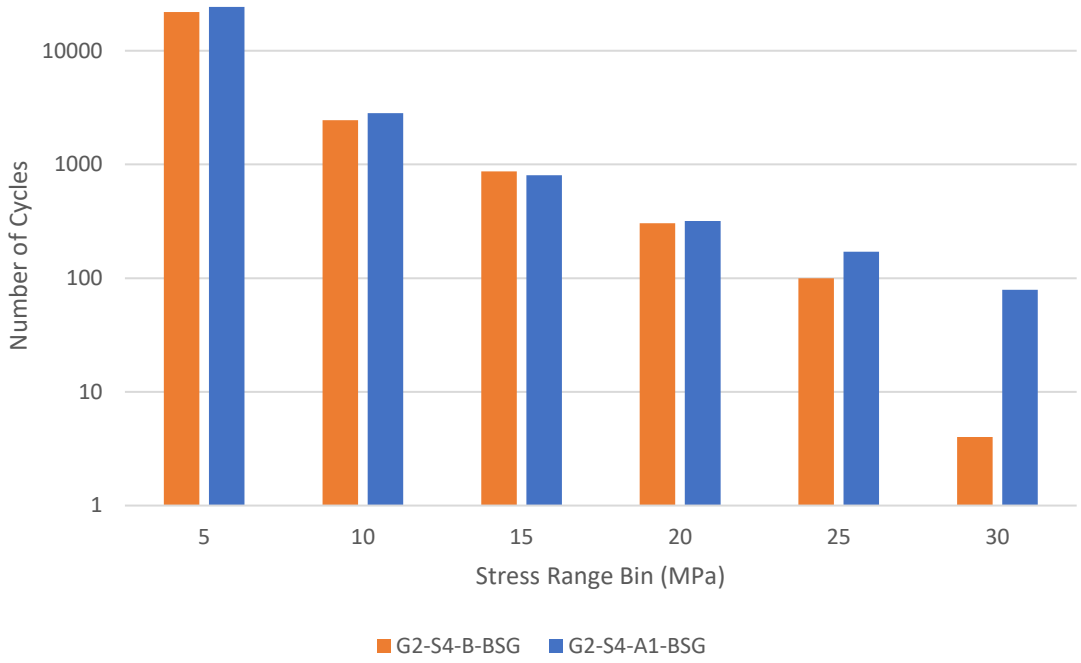

Figure 4.2 - Comparison between connection cycles and girder cycles

A statistical comparison using between the number of cycles at each stress range revealed a Pearson Correlation Coefficient of 0.99, indicating that there is a very strong correlation between the number of cycles at G2-S4-B-BSG and the number of cycles at G2-S4-A1-BSG. This result is reasonable since a load cycle experienced on the girder at Cross-Section B, is typically caused by the same load event that induces a load cycle at the POI. Therefore, for the fatigue evaluation, the load cycles experienced at the POI were assumed to correspond to the load cycles measured at Cross-Section B for the various connections.

To determine the stress state at the POI that is produced by the forces measured in the bracing members, a finite element model (FEM) was created using ANSYS Simulation Software Version 19.0 based on the following:

- Geometry- taken from the as-built drawings;

- Elements: Three dimensional solids;
- Materials: ASTM A373-56T structural steel and field-tested properties:
    - Youngs Modulus: 200,000 MPa
    - Yield Stress: 227.95 MPa
    - Ultimate Stress: 478.66 MPa
- Mesh – Coarse with adaptive sizing function; refinement on the gusset plate connection to the girder;
- Boundary Conditions – The ends of the girder segment were fixed with respect to translation so that the contributions of stress from the bracing could be isolated.

The model isolated only the connection and was used to determine the contributions of the forces in the lateral and transverse bracing to the stress state at the POI. The rainflow data were analyzed to determine the magnitude of stress ranges that existed on each brace. This data, as described in Section 4.2, also provided the number of stress cycles within each stress range experienced by the bracing elements. Since the data for the lateral and transverse bracing elements were nearly the same (Pearson Correlation Coefficient of 0.99), it was reasonable to assume that the stress ranges in each bracing element occurred at the same time (i.e., when a 15 MPa stress was induced in the lateral brace, the same 15 MPa stress was induced in the transverse brace). Therefore, the stresses were input into the FEM following this assumption. The following stress components, as defined by Figure 3.6, were extracted: τ_{zx}, τ_{zy}, σ_{yy} and σ_{zz}.

The instrumented connections were located between the instrumented Cross-Sections as shown in Figure 3.7. This means that, while the load cycles at the connection could be directly correlated to the rainflow data at each cross-section, the magnitude of the corresponding stress in the girder could not be directly obtained. To determine the flexural and shear stresses that were present in the girders at the POI (σ_{xx} and τ_{xy}) another finite element model was utilized, as shown in Figure 4.3. Castillo (2018) created a finite element model of the superstructure as part of a research project at the University of Saskatchewan into damage detection on the bridge. The model was then refined as part of the current project such that its response aligned with the data acquired during the calibration testing. The full extent of one side of the bridge was modelled, including all seven spans. The model consisted primarily of shell elements, except for the bracing elements, which were modelled as frame elements. The boundary conditions of the

model emulated the pinned and roller support conditions of the bridges. The material properties consisted of:

- Structural steel grades: Girders (Grades A373-56T and A242-55), and rolled sections (Grade A7); and
- Concrete materials (taken from as-built drawings): Deck/median/sidewalks (27.5 MPa), and barriers (35 MPa).

The girders and the floor beams were connected to the deck slab using links so that the fixity of the connection could be modified. The frame elements were meshed using the "Auto Mesh" capabilities of SAP2000. As shown in Figure 4.4, the shell elements were automatically meshed such that their maximum size did not exceed 500 mm. A moving live load was defined that matched the calibration vehicle shown in Figure 3.18. The trajectory of the live load was defined as per the calibration loading (i.e. two cases – one meter away from each curb).

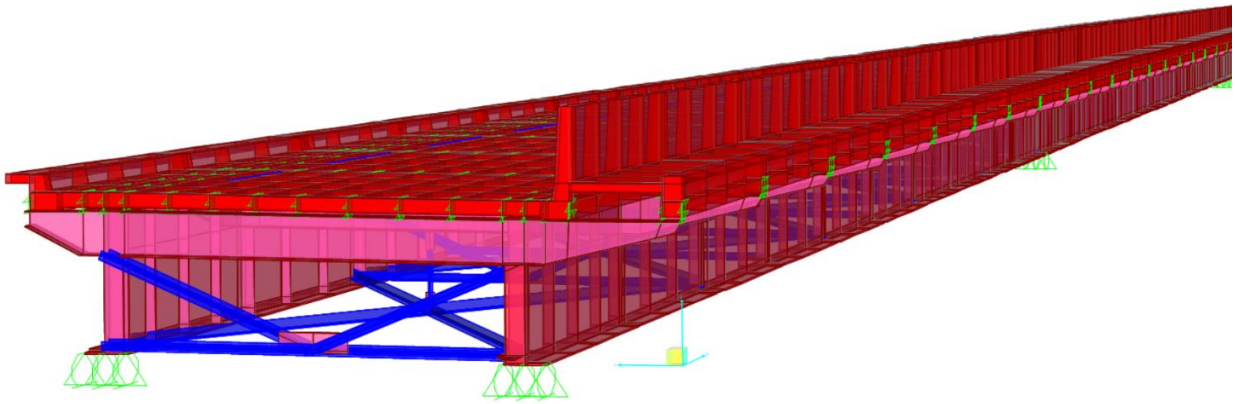

Figure 4.3 – Calibrated finite element model of the Diefenbaker Bridge

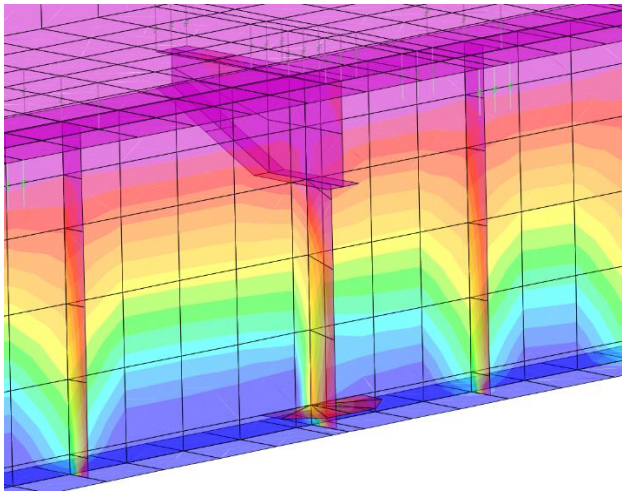

Figure 4.4 – Calibrated finite element model displaying the aspect ratio

To calibrate the model, the moving live load was applied and several parameters, including the interaction of the barrier with the deck, support conditions, and concrete modulus of elasticity were varied until there was a strong correlation between data sets (i.e., between the onsite calibration loading and the model). To determine level of calibration, the stress in the girders at strain gauge locations was examined. The model conditions were then varied until the stress in the girders at the strain gauge locations closely resembled the stress recorded during the onsite calibration loading. As expected, full composite action between the girders and deck provided the closest response to the calibration testing. The concrete modulus of elasticity was calculated to be 24,856 MPa using the method prescribed by CSA S6-14 (CSA, 2014). It was then varied ± 10% but had a minimal effect on the response (i.e., response at gauge locations varied <1.0 MPa). Model behaviour both with and without the barrier acting compositely with the deck was explored. It was found that the structural response was not sensitive to the presence of the barrier. With the girders acting in a fully composite manner with the deck, the model showed a very strong correlation with the calibration data, making further modification to the model unnecessary. Reponses at strain gauge locations were all within ± 15 microstrain, which was considered to be of very close agreement. Using this calibrated model, the moving live load (based on the calibration vehicle) was then varied successively until the stress range at the instrumented cross sections aligned with each rainflow bin.

Through this process, the flexural and shear stresses in the girders were extracted at the POI. Since the transverse and lateral bracing load cycles correlated closely with the girder load cycles for each stress range, they were assumed to coincide directly for the purpose of the fatigue analysis. The three-dimensional stress state, as shown in Figure 3.6, was then deduced from the data by combining the normal and shear stress components from the bridge model (σ_{xx} and τ_{xy}) with the other stress components (τ_{zx}, τ_{zy}, σ_{yy} and σ_{zz}) found using the gusset plate finite element model. These stress components are shown in Table 4.3 and Table 4.4 for each stress range. The Von Mises stress at the POI was then calculated.

Table 4.3 - Three-dimensional stress state at Connection 1 POI

Rainflow Stress Range in Girder at B (MPa)	Equivalent Stress in Girder at POI (MPa)		Resultant Stress Contributions from Bracing Elements at POI (MPa)			
	Flexural Stress, σ_{xx}	Shear Stress, τ_{xy}	Normal Stress, σ_{zz}	Normal Stress, σ_{yy}	Shear Stress, τ_{zy}	Shear Stress, τ_{zx}
5	6.3	2.8	1.3	2.8	0.3	-0.5
10	12.4	5.6	1.9	5.8	0.5	-1.8
15	19.8	8.8	4.6	9.7	0.9	-2.3
20	24.5	11.3	6.7	13.2	1.3	-3.2
25	31.6	14.5	8.9	17.5	2.1	-5.0
30	38.1	17.9	11.4	22.4	2.8	-6.9

Table 4.4 - Three-dimensional stress state at Connection 3 POI

Rainflow Stress Range in Girder at B (MPa)	Equivalent Stress in Girder at POI (MPa)		Resultant Stress Contributions from Bracing Elements (MPa)			
	Flexural Stress, σ_{xx}	Shear Stress, τ_{xy}	Normal Stress, σ_{zz}	Normal Stress, σ_{yy}	Shear Stress, τ_{zy}	Shear Stress, τ_{zx}
5	6.7	3.3	1.3	2.8	0.3	-0.5
10	11.8	5.7	1.9	5.8	0.5	-1.8
15	18.6	9	4.6	9.7	0.9	-2.3
20	23.7	11.5	6.7	13.2	1.3	-3.2
25	30.4	14.8	8.9	17.5	2.1	-5.0
30	37.2	18	11.4	22.4	2.8	-6.9

The von Mises stress results are summarized in Table 4.5. The transverse brace contributed very little stress to the POI because it is connected to not only the gusset plate, but also the transverse stiffener. This means that the force is distributed into the transverse stiffener in addition to the gusset, reducing the force transferred to the POI. Furthermore, since the force is

transferred into the girder at a 90-degree angle, at the transverse stiffener side of the gusset, the contribution from the transverse brace force was found to be very small.

The resulting stresses and number of cycles within each stress range at the POI for Connection 1 and Connection 3 are summarized in Tables 4.5 and 4.6. As is presented in Section 4.7, Connections 1 and 3, located on Girders 2 and 4, respectively, represented the maximum and minimum amount of accumulated damage, and were therefore used to bound the fatigue life evaluation. Theses table formed the basis for the fatigue evaluation.

Table 4.5 - Three-dimensional equivalent stress and number of cycles for Connection 1 in May 2018

Rainflow Bin (MPa)	**Equivalent Von Mises Stress at POI (MPa)**	**Number of Cycles**
5	6.7	21,972
10	13.8	2,455
15	20.7	866
20	25.7	304
25	33.4	100
30	40.8	4

Table 4.6 - Three-dimensional equivalent stress and number of cycles for Connection 3 in May 2018

Rainflow Bin (MPa)	**Equivalent Von Mises Stress at POI (MPa)**	**Number of Cycles**
5	7.5	24,733
10	13.5	3,754
15	20.3	1,341
20	25.6	736
25	33.1	570
30	40.5	269

4.5 Effective Stress Range

Based on the equivalent von Mises stress range and number of cycles outlined in Tables 4.5 and 4.6, the effective stress range was calculated using Equation 2.4. As described in Section 2.2.1.2, the effective stress range is used to convert multiple stress ranges into a single stress range that can be used for comparing fatigue damage accumulation at different details. The results from this calculation are shown in Table 4.7.

Table 4.7 - Effective and Maximum Stress Ranges for Connections 1 & 3

Case	Location	CAFL (MPa)	Effective Stress Range, S_{re} (MPa)	Maximum Stress Range, S_{Rmax} (MPa)
5 MPa Bin Included	**Connection 1**	31	10.5	40.8
	Connection 3	31	13.7	40.8
5 MPa Bin Not Included	**Connection 1**	31	18.4	40.8
	Connection 3	31	22.3	40.8

While the effective stress range is less than the CAFL for both scenarios, according to Fisher et al. (1983), since the maximum stress range (S_{rmax}) of 40.8 MPa is higher than the CAFL, the detail is expected to have a finite fatigue life.

Given the rainflow data for Connection 1 and 3, as shown in Tables 4.5 and 4.6, the individual contributions of each bin to the total damage were calculated and are shown in Figure 4.5. In May 2018, the total damage accumulated at Connections 1 and 3 was 29,173,064 MPa^3 and 81,199,968 MPa^3, respectively.

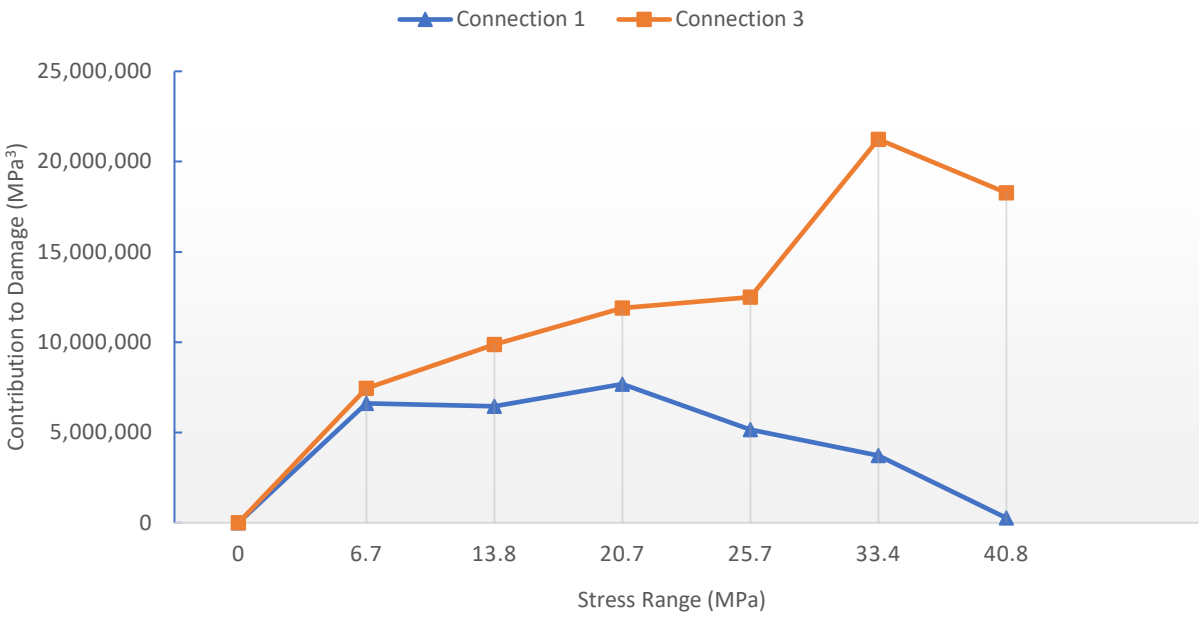

Figure 4.5 – Average contribution to fatigue damage of each bin to the total damage at the POI in May 2018

It can be seen that higher stress ranges contributed the least to the overall fatigue damage of Connection 1 since very few load cycles were recorded in these ranges. However, the significant increase in number of cycles at higher stress ranges for Connection 3 resulted in the high stress ranges contributing the largest amount of damage. This result is logical given the cubic relationship between the number cycles and stress shown in Equation 2.15. A more refined assessment of stress range contribution to total damage could have been performed if the data had been separated into smaller bin ranges during the data acquisition process.

To determine the effect of omitting the 5 MPa rainflow bin on the accumulated damage, an alternative effective stress was calculated without including the cycles in the 5 MPa bin; the results are shown in Table 4.7. As can be seen, the alternative effective stress increased by 75% at Connection 1 and 63% at Connection 3. The fact that Connection 3 was less sensitive to the 5 MPa truncation is logical given the larger contribution to damage from the higher stress range bins. This alternative stress was included as a separate scenario when calculating the remaining fatigue life in the following sections so that the effect of omitting small stress range could be explored.

4.6 Calculation of Remaining Fatigue Life

Since the detail was found to have a finite fatigue life, as described in the previous section, three methods were used to numerically calculate the remaining fatigue life, with the results compared to evaluate the effectiveness of each approach. Connection 1 was selected to be the lower bound (i.e., least damaged connection), and Connection 3 was selected to be the upper bound (i.e., most damaged connection) so that the range of remaining fatigue life on the structure could be understood. The remaining fatigue life was computed as the design fatigue life, as calculated by the three methods, less the existing structure's age (59 years).

4.6.1 Deterministic Approach

The fatigue life of a detail can be estimated using the deterministic method outlined in Section 2.5.2. Since the annual rate of traffic growth was not known with certainty throughout the life of the structure, the procedure recommended in the AASHTO specifications of assuming constant geometrical growth rates of 2% - 6%, was relied upon to establish the bounds of the estimate (AASHTO, 2011). Using Equation 2.10, the remaining fatigue life for the detail was calculated and is summarized in Table 4.8.

Table 4.8 - Calculated remaining fatigue life in years for different scenarios using the Deterministic approach

Location	Probability of Failure	Annual Traffic Volume Growth Rate		
		2%	4%	6%
Connection 1	**5% (Design)**	151	93	69
	50% (Mean)	173	104	77
Connection 3	**5% (Design)**	102	68	52
	50% (Mean)	123	79	60

Based on these calculations, the POI still has many years left before the fatigue life will be exhausted. Even under the most damaging traffic growth scenario, and a probability of failure of 5%, the POI will exceed an overall service life of at least 111 years (i.e. 59 years currently plus 52 years of remaining fatigue life).

To determine the effect of omitting the 5 MPa stress cycles, the remaining fatigue life was calculated using the same method as above. The results are summarized in Table 4.9.

Table 4.9 - Calculated remaining fatigue life in years for different scenarios using the Deterministic approach with 5 MPa stress cycles omitted

Location	Probability of Failure	Annual Traffic Volume Growth Rate		
		2%	4%	6%
Connection 1	**5% (Design)**	164	100	74
	50% (Mean)	186	111	81
Connection 3	**5% (Design)**	107	70	54
	50% (Mean)	128	81	61

From this calculation, it can be seen that by omitting the 5 MPa bin, the estimated fatigue life increases between 5% and 10% for Connection 1 and has a nearly negligible effect on Connection 3.

4.6.2 AASHTO Approach

The remaining fatigue life was calculated using the method outlined in AASHTO's Manual for Bridge Evaluation (2011). To provide a consistent level of reliability, different partial load factors are recommended (Table 2.2) based on how the effective stress range was calculated. Since field data were used to calculate the remaining fatigue life, Equation 2.13 from NCHRP Project 12-81 was used.

The remaining fatigue lives for various scenarios as calculated by Equation 2.13 are summarized in Table 4.10.

Table 4.10 - Calculated remaining fatigue life in years for different scenarios using the AASHTO approach

Location	Probability of Failure	Annual Traffic Volume Growth Rate		
		2%	**4%**	**6%**
Connection 1	**5% (Minimum)**	176	106	78
	16% (Evaluation 1)	185	110	81
	33% (Evaluation 2)	193	114	84
	50% (Mean)	175	105	77
Connection 3	**5% (Minimum)**	126	80	61
	16% (Evaluation 1)	135	85	64
	33% (Evaluation 2)	143	89	66
	50% (Mean)	125	80	60

A partial load factor of 0.85 is recommended for the minimum, evaluation 1, and evaluation 2 calculation levels, corresponding to probabilities of failure of 5%, 16%, 33%, and 50%, respectively. However, for the mean evaluation level (50% probability of failure), a partial load factor of 1.0 is recommended. Since there is a small difference in the resistance factor for a Category E detail (R_R), the calculated fatigue life at the minimum, evaluation 1, and evaluation 2 levels are greater than the mean fatigue life due to the partial load factor. This is unexpected since the mean fatigue life has a higher probability of failure than the other levels.

To determine the effect of omitting the 5 MPa stress cycles, the remaining fatigue life was calculated using the same method as above. The results are summarized in Table 4.11.

Table 4.11 - Calculated remaining fatigue life in years for different scenarios using the AASHTO approach with 5 MPa cycles omitted

Location	Probability of Failure	Annual Traffic Volume Growth Rate		
		2%	4%	6%
Connection 1	5% (Minimum)	188	112	82
	16% (Evaluation 1)	197	117	85
	33% (Evaluation 2)	205	121	88
	50% (Mean)	187	112	82
Connection 3	5% (Minimum)	131	83	62
	16% (Evaluation 1)	140	87	65
	33% (Evaluation 2)	147	91	68
	50% (Mean)	130	82	62

From these calculations, omitting the 5 MPa bin increased the remaining fatigue life by between 5% and 7% at Connection 1, and made a negligible difference at Connection 3.

4.6.3 Probabilistic Approach

The probability of failure for any given year can be calculated using the probabilistic method described in Section 2.5. This method allows owners to evaluate the risk of keeping a structure in service for a given duration and probability of failure (Fasl, 2013). This method can be compared to the other methods by determining the year when a certain probability of failure will occur (i.e., 5%, 50%, etc.). For Connections 1 and 3, the bounds on fatigue damage for the current year was based on the monthly data for May 2018, as calculated using Equation 2.19, and are summarized below:

- Mean Damage for Connection 1 in 2018, μ_{59} = 358,792,737 MPa^3
- Mean Damage for Connection 3 in 2018, μ_{59} = 974,399,611 MPa^3

The mean for 2018 was calculated by taking the average of the damage in May and multiplying it by 12 months of the year. This approach has been taken by other researchers since a full year's worth of data is rarely acquired (Fasl, 2013). May was selected due to the consistency and completeness of data (i.e. 31 days of uninterrupted data were recorded) and because it is probable that it would provide a conservative estimate of the yearly damage. Figure

4.6 displays the probability of failure versus age of bridge for Connection 1 and Connection 3 under varying traffic growth scenarios.

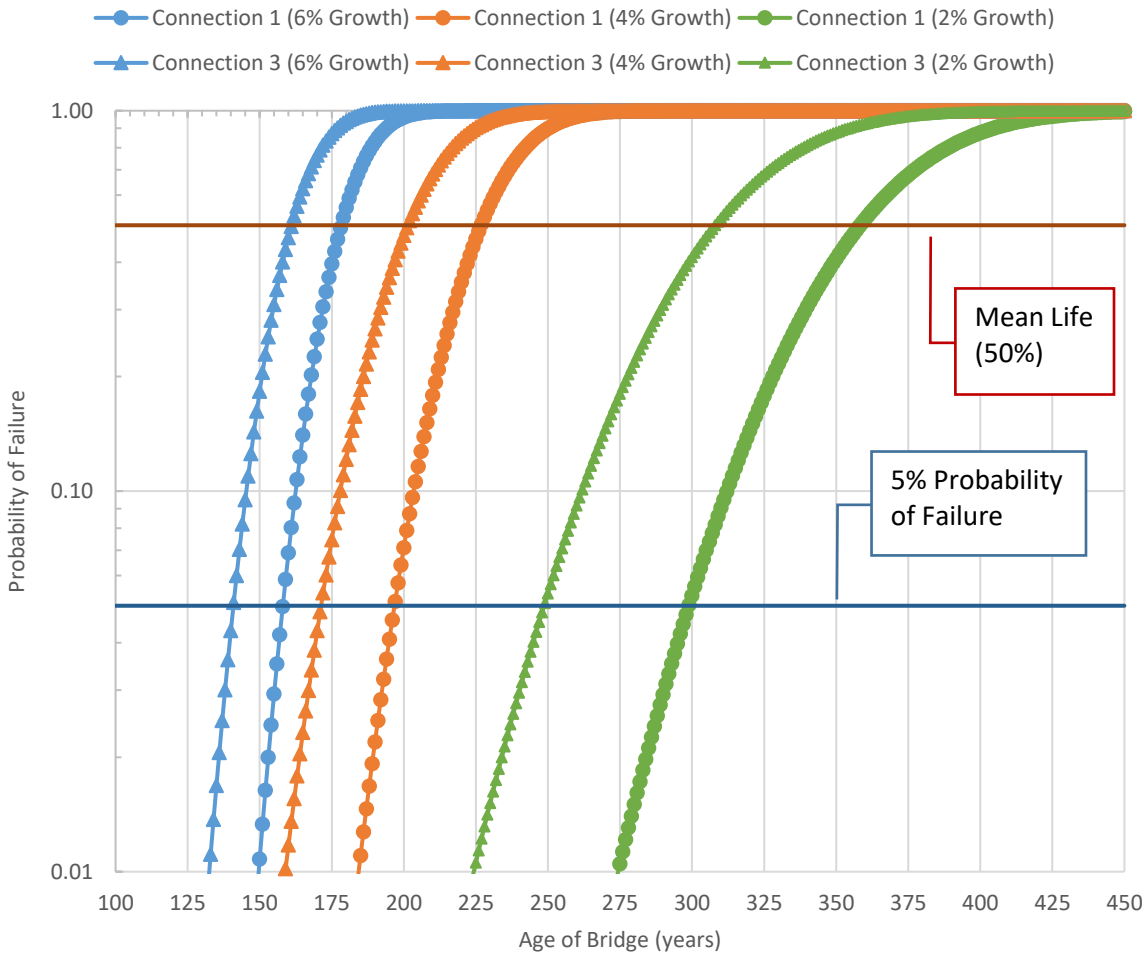

Figure 4.6 - Probability of failure of Connection 1 and Connection 3 with varied traffic growth values

The probability of failure for the current year (2018) is 0% for all traffic growth models and all connections. The failure of Connection 1 (i.e. a probability of failure of 100%) is expected to occur in years 211, 275, and 453 for growth rates of 6%, 4%, and 2%, respectively. Failure of Connection 3 is expected to occur in years 194, 250, and 403 for growth rates of 6%, 4%, and 2%, respectively.

4.6.4 Comparison

The calculated remaining fatigue lives for different probabilities of failure are summarized in Table 4.12 for the three methods of fatigue life evaluation. While the probabilistic

method can compute the probability of failure in any year, only the fatigue life associated with discrete probabilities can be computed for the deterministic method (5% and 50%) and AASHTO method (5%, 16%, 33%, 50%).

Table 4.12 - Calculated remaining fatigue life in years using deterministic, AASHTO, and probabilistic approaches

P_f	Remaining Fatigue Life at Connection 1 (years)			Remaining Fatigue Life at Connection 3 (years)		
	Deterministic	**AASHTO**	**Probabilistic**	**Deterministic**	**AASHTO**	**Probabilistic**
2% Annual Growth						
5%	151	176	240	102	126	189
16%	-	185	264	-	135	214
33%	-	193	284	-	143	234
50%	173	175	300	123	125	250
4% Annual Growth						
5%	93	106	138	68	80	113
16%	-	110	151	-	85	125
33%	-	114	161	-	89	135
50%	104	105	169	79	80	145
6% Annual Growth						
5%	69	78	100	52	61	83
16%	-	81	108	-	64	91
33%	-	84	115	-	66	98
50%	77	77	120	60	60	103

None of the methods indicated that the fatigue life was exhausted at the current time. The governing fatigue condition was found to be Connection 3, assuming a 6% growth rate, and using the deterministic method with a probability of failure of 5%. This scenario yielded a remaining fatigue life of 52 years. The deterministic and AASHTO methods produced comparable results for all growth rates, with exceptional agreement for a probability of failure of 50% in both connections. The fatigue lives predicted at Connection 3 were all consistently shorter than those at Connection 1, which is consistent with the loading distribution observed across the structure. The probabilistic method predicted fatigue lives that followed the same

trends as those predicted by the deterministic and AASHTO methods, but which were consistently longer than the others in all cases. In a study performed by Fasl (2013), in which the fatigue life of four structures was evaluated using three different methods of evaluation, it was found that agreement between methods of fatigue life evaluation was site dependent. Since only one structure was evaluated in this study, it isn't possible to conclusively determine which method is the most reliable; however, it can be concluded that employing multiple methods of evaluation is important to bound the solution. In this study, since the results from the deterministic and AASHTO displayed a very strong agreement, it was decided to use these results as the basis for the recommendations.

4.7 Variation in Measured Response

To measure the variation in fatigue damage accumulated at different parts of the structure, the total damage for the connection detail of each of the four girders was calculated using Equation 4.1:

$$\mathbf{d_{tot}} = \sum \boldsymbol{n_j} \times \boldsymbol{S_j^3} \qquad 4.1$$

where:

$d_{tot} =$ total damage during monitoring period (MPa^3);

$n_j =$ number of cycles at stress range S_j; and

$S_j =$ stress range in bin j.

This method of comparing fatigue damage allows the contribution of a particular bin or stress range to the total damage to be evaluated. It also allows the amount of damage accumulated per day, per month, per connection, and per direction of travel to be characterized, and compared. If different categories were being compared, the index stress range method described in Section 2.2.1.3 would provide a better means of comparison.

4.7.1 Daily Variations

To determine which days of the week experienced the most damage, the total daily damage values were calculated and averaged. Table 4.13 summarizes the number of samples recorded for each day of the week.

Table 4.13 – Number of daily samples recorded during monitoring period

Day of the Week	Number of Samples
Sunday	16
Monday	16
Tuesday	17
Wednesday	17
Thursday	16
Friday	16
Saturday	16

The average damage per day, and per girder, is summarized in Figure 4.7. While only Girders 2, 3 and 4 had instrumented connections, the behaviour of Girders 1 and 4 (i.e., exterior girders) and Girders 2 and 3 (i.e., interior girders) were found to behave with near symmetry (see Section 4.8.1). Therefore, since the behaviour at the connection was correlated to the behaviour of the girder at midspan (Gx-S4-B-BSG) through the calibrated finite element model, the connection on Girder 1 was also evaluated since data were acquired at midspan of this girder. This allowed the comparison of the behaviour of the Northbound structure (Girders 3 and 4) with that of the Southbound structure (Girders 1 and 2).

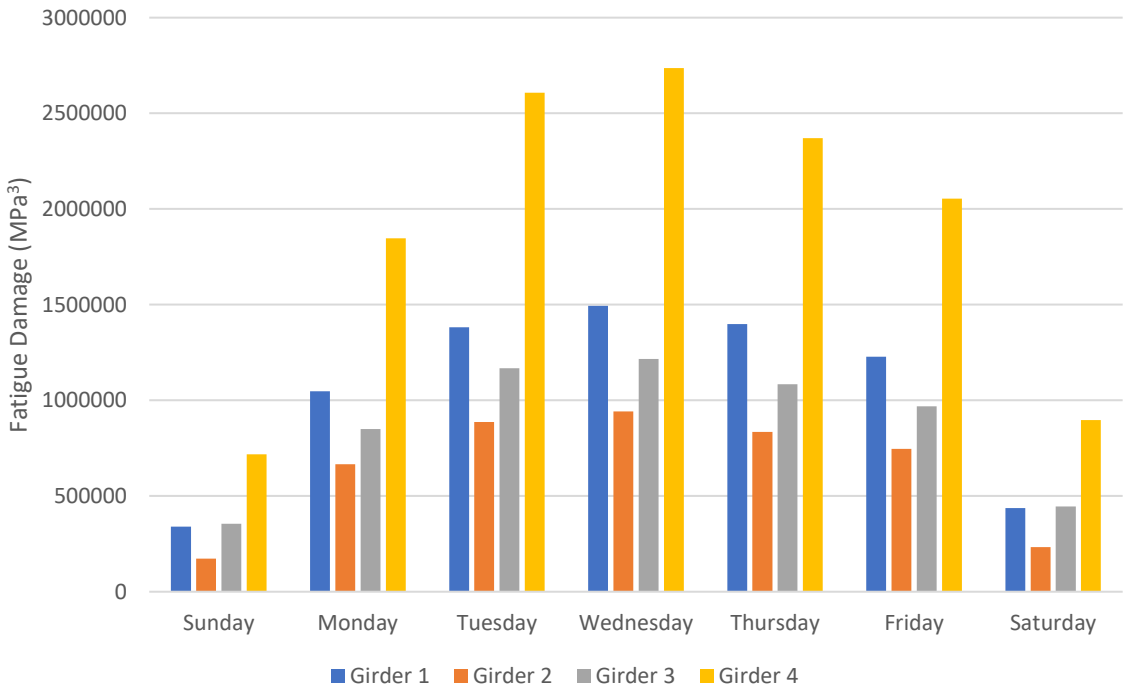

Figure 4.7 - Average daily fatigue damage at POI across all four girders

Several observations can be made regarding the fatigue damage on the structure based on Figure 4.7:

- The connection on Girder 4 (exterior northbound) experiences the most fatigue damage, with the connections on Girders 1, 2 and 3 receiving 54%, 32%, and 47% less damage than Girder 4 experiences, respectively;
- The northbound structure experiences 38% more damage than the southbound structure;
- The bridge sustains less damage during the weekend than during the week; and
- Wednesday contributes the most damage on average, with the daily contributions progressively lessening as the day nears the weekend.

4.7.2 Monthly Variations

To characterize the monthly variations of damage, the total damage values for each month were calculated. However, since not every month recorded the same number of days of data, the monthly totals were divided by the number of days recorded in each month. Table 4.14 summarizes the number of days recorded for each month.

Table 4.14 – Number of samples recorded each month during monitoring period

Month	Number of Days
February	14
March	26
April	30
May	31
June	14

Difficulties in data collection and differences in the number of days within each month are the reason for the variations in the number of days of recorded data in each month. However, by normalizing the data by the number of days of recorded data per month, the relative amounts of damage per month could be explored. Figure 4.8 shows the monthly comparison of results.

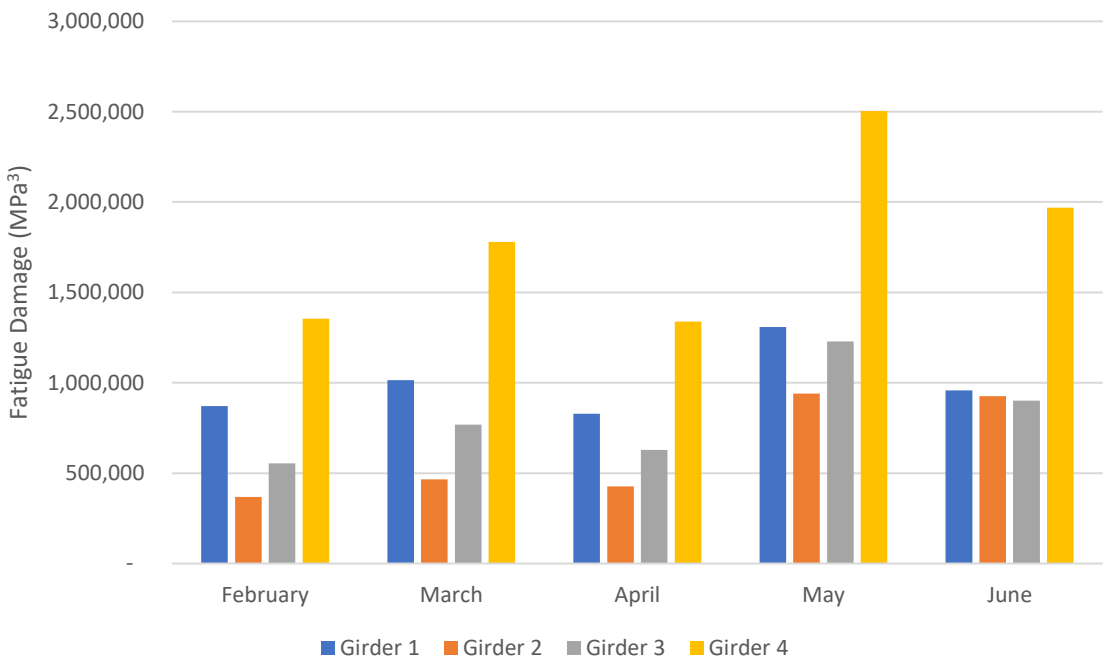

Figure 4.8 - Average daily fatigue damage at POI per month across all four girders

The following observations can be made regarding the monthly trends of fatigue damage based on Figure 4.8:

- As with the daily damage, the exterior girders sustain more damage than the interior girders, with Girder 4 accumulating the most damage;
- May is the most heavily loaded month, with the remaining months following very similar trends; and
- The trend, in general, is that the summer months may contribute slightly more damage on average than the winter months (summer months being May-October, and winter months being November-April). If May and June are considered representative of the summer months, and March and April representative of the winter months, then the winter months contribute 19%, 52%, 34%, and 30% less damage across the connections on Girders 1 through 4, respectively.

4.8 Characterization of In-Situ Structural Behaviour

4.8.1 Overview

The primary objective of this research was to refine the fatigue life evaluation using in-situ data, as was presented in the previous sections. However, there were a number of additional benefits to instrumenting the bridge, the most important of which was characterization of in-situ

performance. Structural behaviour, including the degree of composition action, load sharing, and dynamic load allowance, is typically assumed based on code values found in CSA S6-14. While these values are intended to result in a conservative design, it is not uncommon for the actual structural performance to vary based on site conditions. This can result in conservative condition evaluations that do not accurately reflect in-situ behaviour. Through instrumentation, structural behaviour can be uncovered such that the actual performance is understood. The data from the calibration loading that was used to characterize in-situ behaviour can be found in Appendix C.

4.8.2 Degree of Composite Action

The steel girder sections of Diefenbaker Bridge were designed without shear studs to connect the girders to the deck slab, as shown in Figure 3.11. Since there is no mechanical connection between the steel girders and the concrete deck, the structural behaviour is considered to be non-composite. It is recognized that composite action is possible through the development of interface shear friction, but it is a conservative approach to neglect this action, since it is challenging to quantify without the benefit of instrumentation. In addition, any composite action due to friction that is observed under service loading may not be effective at ultimate conditions.

Before analyzing the degree of composite action, the behaviours of the northbound and southbound structures were investigated and compared, since they are designed as two independent systems. A statistical comparison of the response of the structures under identical loading conditions (i.e., the calibration vehicle travelling down the same lane on both structures) was conducted and it was found that the northbound structure performed in a manner that was nearly identical to the southbound structure. Comparisons of the bending strains at Cross-section B between the exterior and interior girders showed that the responses of the two bridges to same loading generated a 0.99 Pearson Correlation Coefficient. Therefore, the structural behaviour of each bridge was considered to be symmetrical for subsequent analysis.

According to the Ontario Structure Inspection Manual (OSIM), the standard inspection methodology adopted in Saskatchewan, girders are labelled from left to right when looking north from the south abutment. Following this convention, Girder 1 refers to the western-most exterior girder, with Girder 4 being the eastern-most girder. Due to the symmetry of the structures, in discussions to follow, Girder 1 refers to the exterior girders (i.e., Girders 1 and 4) and Girder 2 refers to the interior girders (i.e., Girders 2 and 3).

The behaviour of each structure is compared in Figures 4.8 and 4.9. These charts show the response of the bottom strain gauge at Cross Section B of each corresponding girder under the same loading conditions (i.e., Girders 1 and 4 are loaded in the barriers lanes, Girders 2 and 3 are loaded in the median lanes as described in Section 3.5.1). By overlaying the girders' responses in this manner, it becomes clear that the structures responded in nearly identical manners.

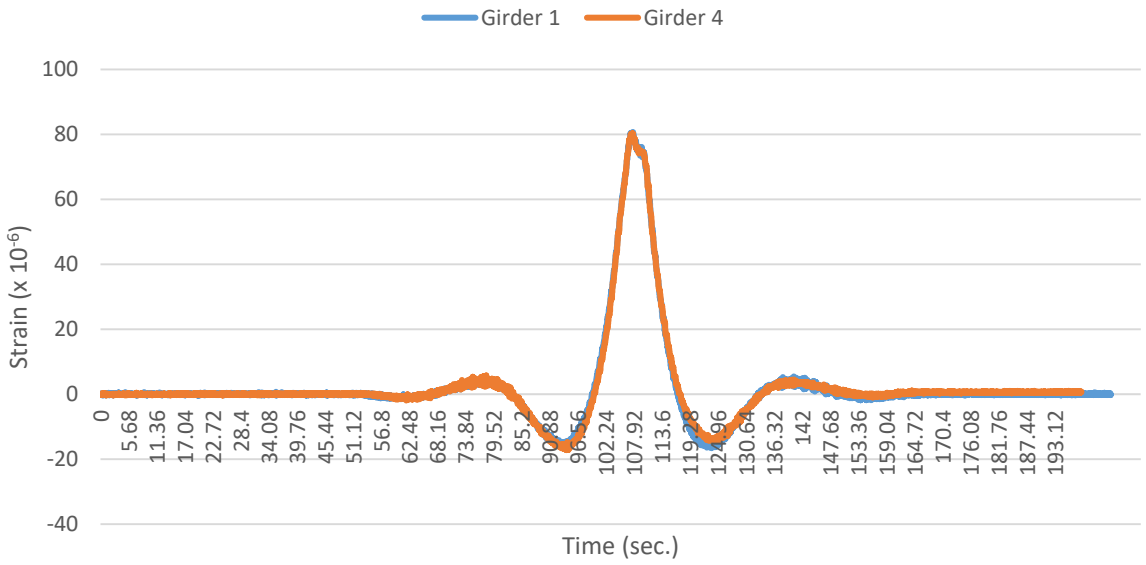

Figure 4.9 - Comparison of the measured strain response at Cross Section B in the bottom of the exterior girders' webs under calibration loading

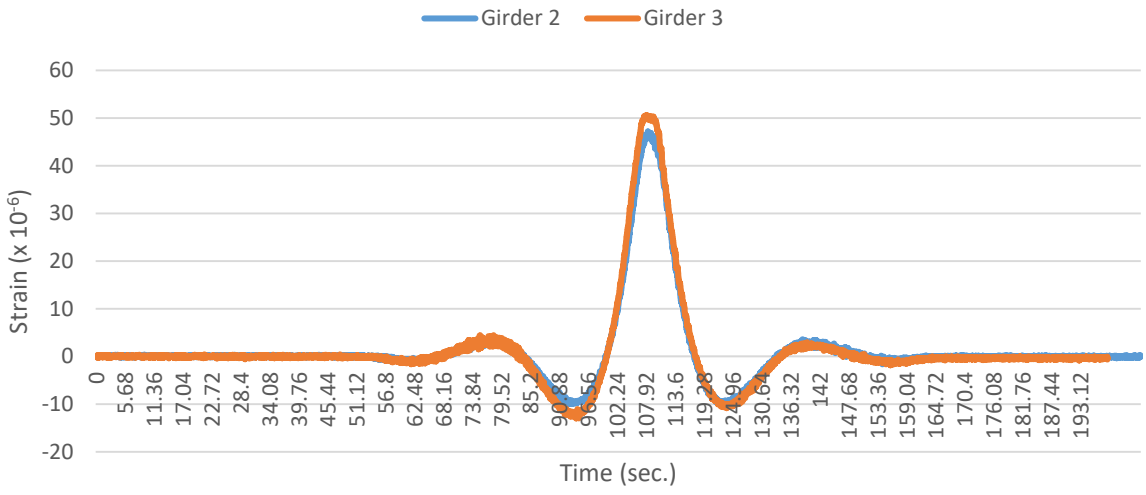

Figure 4.10 - Comparison of the measured strain response at Cross Section B in the bottom of the interior girders' webs under calibration loading

Because strain gauges were located near the top and bottom flanges of the girders, it was possible to determine where the neutral axis fell on each girder under live load. If the structure was entirely non-composite, the neutral axis would fall at the centroid of the steel girder. Since the girder is symmetric, this would be at the mid-height of the web. Figure 4.10 shows the strain response of the interior girders at midspan when a truck was driven across the bridge in the barrier lane. The orange line represents the bottom strain gauge, while the the blue line represents the top strain gauge, and positive strain represents tension.

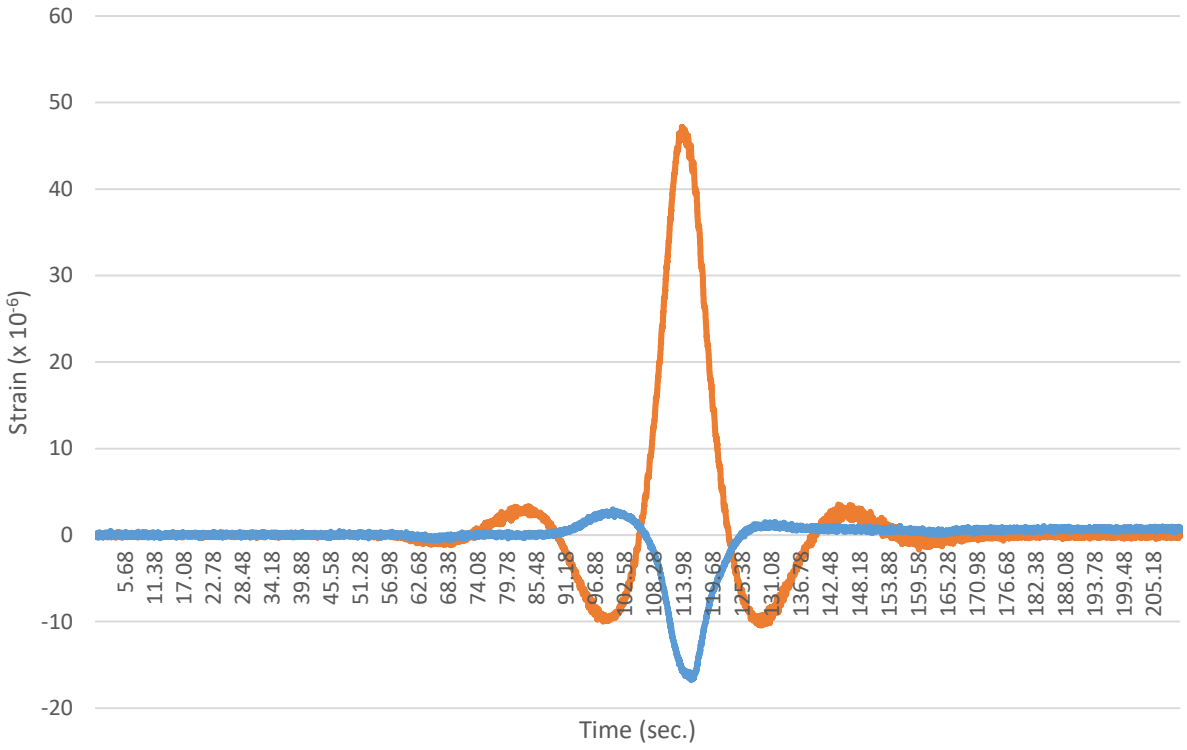

Figure 4.11 - Response of top and bottom strain gauges on interior girder due to barrier lane calibration loading

From this figure it is evident that bottom strain gauge (orange line) peaks in tension as the truck passes over midspan. The top strain gauge (blue line) peaks at the same time in compression. This response is to be expected. However, the different magnitudes of peak strains show that the neutral axis was not at the mid-height of the web, as would be expected if it were non-composite. The neutral axis was much closer to the top flange, which indicates that a degree of composite action was occurring between the concrete bridge deck and the girder.

To quantify the degree of composite action, a transformed section analysis was completed, in which the area of concrete included in the transformed section was varied until the theoretical neutral axis aligned with the measured location, as shown in Figure 4.12. Through this exercise, it was determined that approximately one-half of the deck and the barrier was likely acting compositely with Girder 1. While it is not known with certainty that the entire barrier and half deck portion was acting compositely, it can be concluded that, at the very least, some portion of the barrier, and perhaps some portion of the sidewalk was contributing to the composite action (stiffness) of the section. Girder 2 (interior girders) was assessed in the same manner as Girder 1. Using the same methodology as was used for Girder 1, it was determined that Girder 2 was acting compositely with the deck, with the neutral axis being located approximately 400 mm higher than it would be in a non-composite system.

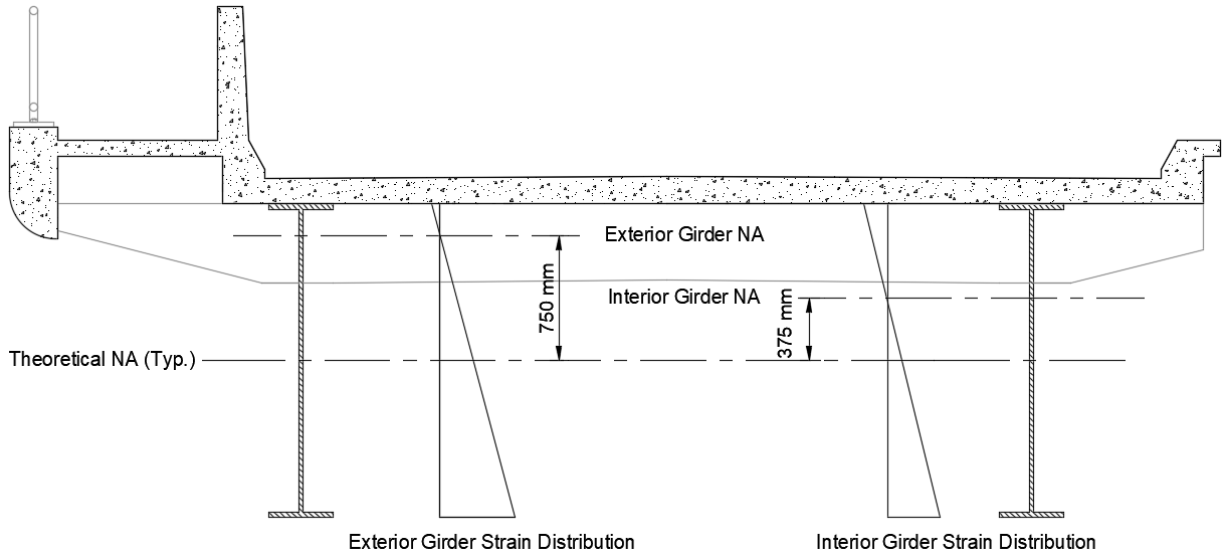

Figure 4.12 - Typical measured strain distribution for an exterior and interior girder under live load

The 375 mm difference between the location of the neutral axis of the interior and exterior girders is challenging to explain with certainty. It is hypothesized that the presence of the barrier is responsible for the neutral axis being higher in the exterior girder. The barriers are located very close to the exterior girders and it is probable that they contribute stiffness to the girder through composite action.

4.8.3 Lateral Load Distribution

With the section properties calculated and correlated with the in-situ behaviour, nominal moments (M_i) were calculated from the strain using Young's Modulus and the Section Modulus as shown in Equation 4.2:

$$M_i = \varepsilon_{meas} \times E_s \times S_{tr} \quad 4.2$$

where:

$\varepsilon_{meas} =$ measured strain;

$E_s =$ Youngs Modulus (200,000 MPa); and

$S_{tr} =$ transformed section modulus.

These values were then used to determine lateral load distribution between girders. From the strain data gathered from each calibration trial, the lateral moment distribution was found using Equation 4.3:

$$\textbf{Lateral Distribution Factor} = \frac{Mi}{\sum_{i=1}^{2} Mi} \quad 4.3$$

Using Equation 4.3, the lateral load distribution was calculated and is summarized in Table 4.15. Since the bridge is a two girder system, the static apportioning method of distributing load was employed to provide a comparison between the actual and theoretical load distribution. The static apportioning method treats the bridge deck like a simply supported beam supported on two girders (Bakht et al., 2015). The reactions from wheel point loads are then considered indicative of the load distribution.

Table 4.15 – Summary of lateral load distribution at midspan

	Actual		**Static Apportioning Method**	
	Barrier Lane Loaded	Median Lane Loaded	Barrier Lane Loaded	Median Lane Loaded
Girder 1	65%	42%	82.5%	10.9%
Girder 2	35%	58%	17.5%	89.1%

From this table, it can be seen that more load sharing occurred between girders than is typically represented by a simplified distribution. This can be partially attributed to the static apportioning method neglecting the torsional rigidity of the bridge in both the transverse and

longitudinal directions, but also to the increased composite action that was present between the girders and the deck.

It can also be noticed that the exterior girder attracted more load than the interior girder. This is logical, given the increased stiffness from composite action that the exterior girder exhibited due to the participation of the barrier wall.

Additionally, it was observed on site that vibrations could be felt on one structure when trucks passed on the opposing structure. This observation is verified by the acceleration measurements on each girder. A response was measured on the northbound structure when the calibration loading was present only on the southbound structure. However, when the strain data were investigated for each structure, no response was registered on the structure that was not loaded. This means that, while vibrations are likely transmitted through the median and/or the shared substructure, there is no load transferred from one structure to the other (i.e. movement but little deformation).

4.8.4 Bearing Restraint

Bearing restraint can have a large influence on a structure's behaviour if movement is restricted when it shouldn't be. At the Diefenbaker Bridge, Piers 3 and 4 are pinned connections (translation is fixed, rotation is permitted), with all other supports being rollers (translation and rotation permitted).

There is potential for a degree of arching action to be present in span four due to the bearing configuration, however, measured strain data suggested that arching did not play a significant role in the way load is transferred from the deck to the substructure. If arching action was a significant factor, the location of the neutral axis obtained from the transformed section analysis done in Section 4.8.2. would not have aligned with the location found using the strain data since a net axial force would have been present.

4.8.5 Bridge Dynamics

Chapter Three of CSA S6-14 recommends that a dynamic load influence factor of 1.25 be applied to the factored force live load effect if more than three axles govern the load response (CSA, 2014), as would be the case for the Diefenbaker Bridge given the length of the spans. However, it has been observed by Feldman et al. (2011) on the Red Deer River Bridge, that the dynamic influence of moving loads can be substantially less than what is prescribed by the standard. To evaluate the dynamic load effect on the Diefenbaker bridge, the peak strain

responses from the full speed calibration loading ($\varepsilon_{dynamic}$) were compared with the peak strain response from the slow speed calibration loading (ε_{static}) as described in Section 3.5.1. Results of this comparison summarized in Table 4.16 based on the following expression:

$$\textbf{Dynamic Load Allowance} = \frac{\in \textbf{dynamic}}{\in \textbf{static}} \qquad 4.4$$

Table 4.16 - Summary of dynamic load allowance on Diefenbaker Bridge using Equation 4.4

	Girder 1	**Girder 2**	**Girder 3**	**Girder 4**
SB Barrier 1	0.9095	1.0893	-	-
SB Barrier 2	1.0338	0.9744	-	-
SB Median 1	1.0380	0.9970	-	-
SB Median 2	1.0556	1.0055	-	-
NB Barrier 1	-	-	1.0336	0.9756
NB Barrier 2	-	-	1.0192	0.9795
NB Median 1	-	-	0.9652	1.0252
NB Median 2	-	-	0.9509	1.0386
Average	1.0092	1.0166	0.9922	1.0047

The average dynamic allowance among the girders was found to be 1.0057. This is substantially less than the value of 1.25 prescribed in CSA S6-14 and indicates that there was not a significant dynamic effect present.

It should be noted that dynamic impact is influenced by several factors including riding surface roughness, vehicle weight, axle arrangement, speed, and suspension characteristics (Feldman et al. 2011). This means that, while the calibration loading used for this study did not produce significant dynamic effects, situations may exist where the dynamic load amplification is significant.

CHAPTER 5. CONCLUSIONS AND RECOMMENDATIONS

5.1 Summary

The focus of this research was on exploring how structural health monitoring could be used to refine a fatigue life evaluation of the Diefenbaker Bridge. The accumulation of fatigue damage was evaluated on a per girder basis, a per direction basis, as well as a daily, and monthly basis. The remaining fatigue life was calculated using a deterministic method, AASHTO's method, and a probabilistic method using strain data obtained through structural health monitoring. Using this same strain data, structural behaviour such as the degree of composite action, the lateral load distribution, and dynamic load amplification were investigated and quantified.

Conclusions from this research are organized into two areas: techniques for fatigue evaluation, and structural health monitoring. Lastly, recommendations are made for future studies.

5.2 Conclusions

5.2.1 Techniques for Fatigue Evaluation

The techniques used for evaluating the fatigue effects on the Diefenbaker bridge using structural health monitoring data, as well as the results of that evaluation were described in Chapter Two and Chapter Four. Based on that analysis, the following conclusions can be made:

1. **There is considerable fatigue life remaining at the bracing's connection to the girder web on the Diefenbaker Bridge.**

The deterministic and AASHTO approaches provided very similar fatigue life predictions when similar probabilities of failure and traffic growth models were assumed. The remaining fatigue life predicted by these approaches varied between 52 – 143 years remaining at Connection 3 (located on the northbound exterior girder), and 69 – 193 years remaining at Connection 1 (located on the soutbound interior girder), depending on the traffic growth models (between 2% and 6% annual growth) and probabilities of failure (5%, 16%, 33%, and 50%) utilized in the evaluation. These evaluations may be relatively conservative since the gusset plate's connection to the girder web was characterized as Category E detail (as per CSA S6-14 Chapter 10), while research on the response of this connection type to tri-directional stress has

shown that the detail may have a larger constant amplitude fatigue threshold (CAFL) stress than is currently being used (NCHRP, 1990).

2. **Fatigue damage varies with location on the structure due to loading patterns and structural response unique to each structure.**

Diefenbaker bridge's northbound superstructure accumulated more fatigue damage than the southbound superstructure. More specifically, the exterior girders experienced a larger number of high magnitude stress cycles than the interior girders (as described in Sections 4.7.1 and 4.7.2), with the northbound exterior lane accumulating the most damage on the structure**.** This observation supports the theory that heavily loaded trucks are travelling northbound to deliver supplies to the northern half of the province and returning south with lower loads. It also makes sense that the exterior lane would be more heavily loaded than the interior lane, since the exit onto another major highway (Highway No. 55) is located just past the north abutment, on the barrier side.

Wednesday is the most heavily loaded day of the week, and May is the most heavily loaded month among the months that were considered. By examining the damage accumulated during the other week days, it was found that the amount of damage decreased as the days became closer to the weekend, with weekends producing comparably very little damage. Following May, the next most loaded month is June, followed by March, then April, and lastly, February. Observations of these daily and monthly trends support the theory that the loading on the structure is strongly connected to commercial activity.

3. **The partial load factor of 0.85 used in the AASHTO approach (AASHTO, 2011) is not justified when using field monitored data.**

The modified AASHTO approach proposed by NCHRP Project 12-81 applies a partial load factor of 0.85 to the effective stress range calculation when the stress ranges are determined by field-measured strains. This partial load factor is the only difference between the modified AASHTO approach and the deterministic method. When a probability of failure of 50% is assumed, this factor increases to 1.0, which produces a remaining fatigue life that is equivalent to that obtained using a 5% probability of failure. This is not a logical result since a higher probability of failure should produce a longer fatigue life.

4. **Omitting stress cycle magnitudes up to 25% of the constant amplitude fatigue threshold stress range is not always justified.**

Some researchers recommend that load cycles with stress ranges below 25%-50% of the CAFL not be included in the fatigue life evaluation calculations (Connor et al., 2005). The gusset plate connection on Diefenbaker Bridge is considered a Category E detail with a CAFL of 31 MPa. To determine the effect of not including stress ranges below 25% of CAFL, the 5 MPa bin from the rainflow analysis was removed from the fatigue life evaluation. Truncating this data had little to no effect on fatigue life predictions of Connection 3. However, it increased the fatigue life estimate of Connection 1 by between 5% and 10%. The reason Connection 1 was impacted more than Connection 3 is due to the differences in contribution to total damage of each stress range. Connection 3 sustained most of its damage from the higher stress ranges of 25.7 MPa to 40.8 MPa, whereas Connection 1 sustained most of its damage from the smaller stress ranges of 6.7 MPa to 20.7 MPa. By truncating one of the more damaging stress ranges, a larger impact was seen on the fatigue life predicted. Therefore, truncating load cycles with stress ranges up to 25% of the CAFL does not appear to be justified but is dependent on the specific situation.

5. **There is a large amount of uncertainty that remains with the fatigue evaluation.**

Despite the reduction in uncertainty that short term structural health monitoring provides, traffic patterns can change from day to day, month to month, and year to year. Weather, accidents, commercial activity, and many other factors affect the accumulation of damage on a structure, and these are difficult to predict and account for. If possible, the strain data obtained through structural health monitoring should be validated using traffic counts, or a bounded approach be taken by employing multiple methods of evaluation (i.e., AASHTO, deterministic, probabilistic) on numerous locations, with varying traffic growths.

5.2.2 Structural Health Monitoring

The structural health monitoring plan was detailed in Chapter Three. The following conclusions can be made from the selected monitoring plan:

1. **Calculating fatigue damage using field data provides a more realistic estimate than using structural analysis and standard design assumptions.**

The Canadian Highway Bridge Design Code (CSA S6-14) does not directly address fatigue life evaluation of existing structures. Therefore, local or code specified design vehicles are typically used in conjunction with prescribed dynamic load influence factors and lateral live load

distributions to estimate the parameters used for fatigue life evaluation. However, these values are not bridge specific, and may lead to an overly conservative, or inaccurate, remaining fatigue life calculation. A well-designed structural health monitoring system provides the local stress range and cycle spectrum that can be used in the fatigue life calculation to improve the accuracy of the estimate. At Diefenbaker Bridge, a fatigue life estimate based on structural analysis and code specified parameters predicted a remaining fatigue life of less than five years (ISL, 2016). Using the structural health monitoring data obtained as part of the current study, the remaining fatigue life was calculated to be 52 years, as the most conservative estimate.

The structural health monitoring data allowed for the characterization of certain behaviours that were found to differ substantially from code specifications. For example, full composite behaviour between the steel girders and the concrete deck at service loading levels was discovered, despite the lack of mechanical attachment between the deck and girder. In addition, no increase in stresses resulting from dynamic load amplification was found during the calibration loading tests and increased load sharing between adjacent girders (lateral live load distribution) was measured.

2. **Having a monitoring plan that captures both global behaviour, and local behaviour is important.**

Performing a structural analysis before developing the instrumentation plan for a structural health monitoring system will help identify the specific details that govern the fatigue life. The identified areas should be instrumented on a local level to understand the stress distribution, but instrumentation that can be used to calibrate a full model of the structure should be installed as well. In this study, it would have been advantageous to have instrumentation on the girder at the location being investigated (i.e., in addition to the global instrumentation). Unexpected in-situ behaviour may mean a detail at a different location becomes critical, in which case a calibrated finite element model of the structure as a whole may be required. The calibrated finite element model of Diefenbaker Bridge proved valuable for determining the stress contributions from the girder at the gusset plate detail.

5.3 Recommendations for Future Study

The following recommendations are for research projects that would contribute to a better understanding of fatigue life evaluation and structural health monitoring, and could be completed using the data that has been collected during the current study:

1. **Research and development of a data management system.**

Structural health monitoring provides the means to refine a multitude of different analyses. Regardless of the purpose behind the monitoring, a large volume of data will typically be acquired, which can very cumbersome to manipulate. Research into, and development of, a data management system that can automatically acquire and manipulate the raw strain data into useful forms for specific applications would be very valuable for both researchers and public agencies.

2. **Development of a damage detection system for the Diefenbaker Bridge.**

A large volume of data was acquired for the purposes of this study. This data could be used to explore the effects of damage on the Diefenbaker Bridge, and for the preliminary development of a damage detection system. Given the history of a constraint induced fracture on this structure, a damage detection system that could warn the owner of structural damage immediately would increase public safety.

3. **Develop a weigh-in-motion system that utilizes the response characteristics of the Diefenbaker Bridge.**

Utilizing existing structures as a weigh-in-motion scale could be useful for both bridge management and for provincial permitting. Currently, a weigh-in-motion system only exists on Highway No. 2 north of Prince Albert. By using the Diefenbaker Bridge as a weigh-in-motion system, traffic from Highway No. 55 could be included, thus enabling collection of all northbound and southbound traffic.

4. **Perform an experimental study on the gusset plate's connection to the girder web's fatigue performance.**

The current study concluded that load cycles at lower stress ranges can influence the calculated fatigue life, and that omitting these cycles is not always justified. However, an experimental study on whether these load cycles at smaller stress ranges contribute to fatigue damage in practice, would provide validation to this conclusion.

REFERENCES

AASHTO. (1990). *Guide Specifications for Fatigue Evaluation of Existing Steel Bridges*. Washington, DC: American Association of State Highway and Transportation Officials.

AASHTO. (2011). *The Manual for Bridge Evaluation*. *2nd Edition.* Washington, DC: American Association of State Highway and Transportation Officials.

AASHTO. (2014). *LRFD Bridge Design Specification*. 7*th Edition.* Washington, DC: American Association of State Highway and Transportation Officials.

AASHTO. (2017). *LRFD Bridge Design Specification*. *8th Edition.* Washington, DC: American Association of State Highway and Transportation Officials.

ASCE. (1982). *Fatigue Reliability: Variable Amplitude Loading*. Journal of the Structural Division, 108(ST1), 47-69.

ASTM. (2011). *E1049-85: Standard Practices for Cycle Counting in Fatigue Analysis*. West Conshohocken: ASTM International.

Bakht, B., and Mufti, A. (2015). *Bridges – Analysis, Design, Structural Health Monitoring, and Rehabilitation (2nd Edition).* Springer International Publishing. Switzerland

Barsom, J., and Rolfe, S. (1999). *Fracture and Fatigue Control in Structures: Applications of Fracture Mechanics (3rd ed.)*. West Conshohocken, PA: ASTM.

Bocchini, P., and Frangopol, D. (2011). *A Probabilistic Computational Framework for Bridge Network Optimal Maintenance Scheduling*. Reliability Engineering and System Safety, 96, 332-349.

Bowman, M., Fu, G., Zhou, Y., Connor, R., and Godbole, A. (2012). *Fatigue Evaluation of Steel Bridges*. Washington, DC: Transportation Research Board.

Beer, F., Johnston, E., Dewolf, J., Mazurek, D. (2009). *Mechanics of Materials. 5th Edition.* McGraw-Hill. New York, NY

Canadian Standards Association (CSA). (2014). *Canadian Highway Bridge Design Code (CAN/CSA S6-14)*. Missisauga, Ontario, Canada.

Castillo, J. (2019). An Investigation into the Effects of Damage on the Diefenbaker Bridge. University of Saskatchewan. Saskatoon. Saskatchewan.

Chung, H. (2004). *Fatigue Reliability and Optimal Inspection Strategies for Steel Bridges.* Austin, TX: The University of Texas at Austin. Ph.D. Dissertation

Connor, R., and Fisher, J. (2006). *Identifying Effective and Ineffective Retrofits for Distortion Fatigue Cracking in Steel Bridges Using Field Instrumentation*. Journal of Bridge Engineering, 11(6), 745-752.

Dowling, N. (1972). *Fatigue Failure Predictions for Complicated Stress-Strain Histories*. Journal of Materials, 7(1), 71-87.

Downing, S., and Socie, D. (1982). *Simple Rainflow Counting Algorithms*. International Journal of Fatigue, 4(1), 31-40.

ECCS Technical Committee 6. (1985). Recommendations for the Fatigue Design of Steel Structures. Rotterdam: European Convention for Constructional Steelwork.

Ellis, R., Connor, R., Medhekar, M., MacLaggan, D., and Biolowas, M. (2013). *Investigation and Repair of the Diefenbaker Bridge Fracture*. Proceedings of the Transportation Association of Canada Conference. Winnipeg, Manitoba, Canada.

Fasl, J. (2013). *Estimating the Remaining Fatigue Life of Steel Bridges Using Field Measurements*. The University of Texas at Austin. Ph.D. Dissertation.

Fasl, J., Samaras, V., Reichenbach, M., Helwig, T., Wood, S., Potter, D., Lindenberg, R., and Frank, K. (2012c). *Evaluating Fatigue Damage Using Strain Data*. Conference Proceedings of NDE/NDT for Highways and Bridges: Structural 334 Materials Technology. New York, NY: American Society for Nondestructive Testing.

Feldman, L., Jackson, K., Sparling, B., and Sparks, G. (2011). *Comparison of Load Rating Techniques for the Red Deer River Bridge.* Canadian Journal of Civil Engineering. Numer 38: 1072-1081.

Fisher, J., Albrecht, P., Yen, B., Klingerman, D., and McNamee, B. (1974). *Fatigue Strength of Steel Beams with Welded Stiffeners and Attachments*. Washington, D.C.: Transportation Research Board.

Fisher, J., Mertz, D., and Zhong, A. (1983). *Steel Bridge Members Under Variable Amplitude Long Life Fatigue Loading.* Washington, D.C.: Transportation Research Board.

Fisher, J., Kulak, G., and Smith, I. (1998). *A Fatigue Primer for Structural Engineers*. Chicago, IL: National Steel Bridge Alliance.

Fisher, J., Nussbaumer, A., Keating, P., and Yen, B. (1993). *Resistance of Welded Details Under Variable Amplitude Long-Life Fatigue Loading*. Washington, D.C.: Transportation Research Board.

Google. (2019). Prince Albert, Saskatchewan. Retrieved from https://www.google.ca/maps/@53.2037137,-105.7494542,4504m/data=!3m1!1e3?hl=en

ISL Engineering and Land Services. (2016). *Diefenbaker Assessment and Evaluation Report*. Saskatchewan Ministry of Highways and Infrastructure. Saskatoon. Saskatchewan. Canada.

Keating, P., and Fisher, J. (1986). *Evaluation of Fatigue Tests and Design Criteria on Welded Details.* Washington, DC: Transportation Research Board.

Keating, P., Halley, S., and Fisher, J. (1986). *Fatigue Test Database for Welded Steel Bridge Details*. Bethlehem, PA: Lehigh University. Report 488.2.

Kim, S.-H., Lee, S.-W., and Mha, H.-S. (2001). *Fatigue Reliability Assessment of an Existing Steel Railroad Bridge.* Engineering Structures, 23, 1203-1211.

Kwon, K., and Frangopol, D. (2010). *Bridge Fatigue Reliability Assessment Using Probability Density Functions of Equivalent Stress Range Based on Field Monitoring Data*. International Journal of Fatigue, 32, 1221-1232.

Leander, J., Andersson, A., and Karoumi, R. (2010). *Monitoring and Enhanced Fatigue Evaluation of a Steel Railway Bridge. Engineering Structures*, 32, 854-863.

Li, Z., Chan, T., and Ko, J. (2001). *Fatigue Analysis and Life Prediction of Bridges with Structural Health Monitoring Data - Part I: Methodology and Strategy*. International Journal of Fatigue, 23, 45-53.

Liu, M., Frangopol, D., and Kwon, K. (2010). *Fatigue Reliability Assessment of Retrofitted Steel Bridges Integrating Monitored Data*. Structural Safety, 32, 77- 89.

Miner, M. (1945). *Cumulative Damage in Fatigue*. Journal of Applied Mechanics, 12, A159-A164.

Moses, F., Schilling, C., and Raju, K. (1987). *Fatigue Evaluation Procedures for Steel Bridges*. Washington, D.C.: Transportation Research Board.

National Cooperative Highway Research Program. (1990). *Distortion Induced Fatigue Cracking in Steel Bridges,* NCHRP Report 336, Transportation Research Board, National Research Council, Washington, DC.

Oresci, A., Frangopol, D., and Kim, S. (2010). *Optimization of Bridge Maintenance Strategies Based on Multiple Limit States and Monitoring*. Engineering Structures, 32, 627-640.

Saskatchewan Ministry of Highways and Infrastructure. (1959). *Diefenbaker Bridge As-Built Drawings.* Prince Albert, Saskatchewan.

Schilling, C., Klippstein, K., Barsom, J., and Blake, G. (1978). *Fatigue of Welded Steel Bridge Members Under Variable-Amplitude Loadings*. Washington, D.C.: Transportation Research Board.

Stantec Consulting. (2013). *Prince Albert Area Second Bridge River Crossing Study*. City of Prince Albert, Saskatchewan.

Stantec Consulting. (2015). *Diefenbaker Bridge Management Plan*. City of Prince Albert. Prince Albert, Saskatchewan.

Swenson, K., and Frank, K. (1984). *The Application of Cumulative Damage Fatigue Theory to Highway Bridge Fatigue Design*. Austin, TX: Center for Transportation Research.

Szerszen, M., Nowak, A., and Laman, J. (1999). *Fatigue Reliability of Steel Bridges*. Journal of Constructional Steel Research, 52, 83-92.

Ye. X. (2014). *A State of the Art Review on Fatigue Life Assessment of Steel Bridges*. Journal of Mathematical Problems in Engineering. (3), 1-13

Zhou, Y. (2006). *Assessment of Bridge Remaining Fatigue Life Through Field Strain Measurement*. Journal of Bridge Engineering, 11(6), 737-744.

APPENDIX A - INSTRUMENTATION PLAN

Included in this appendix are the as-built instrumentation drawings that provide detail on where the sensors were installed on the Diefenbaker Bridge, how they were connected, and what equipment was used to transmit the data from the cabinet.

RAW DATA. REFINED RESULTS.

ISL ENGINEERING AND LAND SERVICES
DIEFENBAKER BRIDGE
STRUCTURAL HEALTH MONITORING SYSTEM

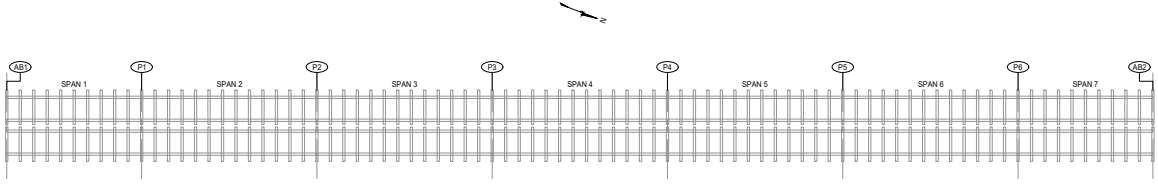

BDI
740 S PIERCE AVE, SUITE 15
LOUISVILLE, CO 80027
303.494.3230
WWW.BDITEST.COM

ISSUE

CLIENT

ISL
259 Robin Crescent
Saskatoon, SK S7L 6M8

PROJECT NAME

ISL ENGINEERING AND LAND SERVICES
DIEFENBAKER BRIDGE
STRUCTURAL HEALTH MONITORING SYSTEM

Drawn By:	KNR
Checked By:	JDS
Date:	2/16/18
Client No.:	
BDI No.:	170906-SK
SCALE:	NTS

COVER PAGE

SHM-00

ANNOTATION KEY

SECTION CALLOUT:

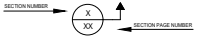

DETAIL CALLOUT:

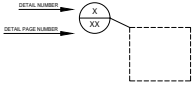

DRAWING TITLE:

SENSOR CALLOUT:

ELEVATION CALLOUT:

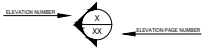

GAGE LEGEND & SPECIFICATION

SYMBOL	TYPE	BRAND	MODEL	NOTES
	WELDABLE AXIAL STRAIN GAGE (PLAN, SECTION, ELEVATION)	HPI	HBW-35-125-6-VR	
	ACCELEROMETER	BDI	UNIAXIAL	
	WEATHER STATION	VAISALA	HMP 60	

SENSOR LEGEND - PHASE 1	SENSOR COUNTS	CHANNEL COUNTS
WELDABLE AXIAL STRAIN GAGE	(48)	(48)
ACCELEROMETER	(4)	(4)
WEATHER STATION	(1)	(1)
TOTAL		(53)

INDEX OF SHEETS

LOCATION KEY

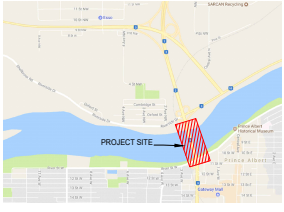

INDEX OF REVISIONS

NO.	DATE	REVISION DESCRIPTION
-	03 NOVEMBER 2017	STRUCTURAL HEALTH MONITORING SYSTEM (SHMS) INSTRUMENTATION PLAN
1	29 NOVEMBER 2017	STRUCTURAL HEALTH MONITORING SYSTEM (SHMS) INSTRUMENTATION PLAN (AS BUILT)
2	12 FEBRUARY 2018	SHMS INSTRUMENTATION PLAN (AS BUILT) WITH OPERATION GUIDE
2	16 FEBRUARY 2018	SHMS SYSTEM SPECIFICATIONS WITH MODIFICATIONS PER ISL COMMENTS
BDI REFERENCE NUMBER: 170906-SK		

BDI
740 S PIERCE AVE, SUITE 15
LOUISVILLE, CO 80027
303.494.3230
WWW.BDITEST.COM

ISSUE

CLIENT

ISL
259 Robin Crescent
Saskatoon, SK S7L 6M8

PROJECT NAME

ISL ENGINEERING AND LAND SERVICES
DIEFENBAKER BRIDGE
STRUCTURAL HEALTH MONITORING SYSTEM

Drawn By:	KNR
Checked By:	JDS
Date:	2/16/18
Client No.:	
BDI No.:	170906-SK
SCALE:	NTS

OVERALL LEGEND

SHM-01

GENERAL NOTES

PROJECT LOGISTICS / TIMELINE:
MONITORING SYSTEM PARAMETERS CONSIST OF MOBILIZATION/DEMOBILIZATION TO PROJECT SITE AND INSTALLATION OF ALL SENSORS AND DATA ACQUISITION EQUIPMENT.
1. MONITORING SYSTEM INSTALL SHALL BEGIN 11/13/2017.
2. MONITORING OF DIEFENBAKER BRIDGE SHALL BEGIN FOLLOWING INSTALLATION OF ALL SENSORS.
3. ACCESS PROVIDED BY BDI SPRAT ROPE ACCESS.

MONITORING INSTRUMENTATION:
1. INSTRUMENTATION SHALL INCLUDE WELDABLE QUARTER ARM AXIAL STRAIN GAGES, UNIAXIAL ACCELEROMETERS, AND A WEATHER STATION.
   1.1. ALL SENSORS TO BE RATED TO INGRESS PROTECTION IP66.
2. AXIAL STRAIN GAGES:
   2.1. ORIENTATION DESCRIBED ON SHM-09.
   2.2. ILLUSTRATED DIMENSIONS SHALL BE BASED FROM CENTER OF GAGE SHOWN IN SHM-09 DETAIL 2A.
   2.3. QUARTER ARM STRAIN GAGE SHALL BE CONNECTED TO COMPLETION UNIT MODULE MOUNTED TO STRUCTURE ADJACENT TO GAGE LOCATION
   2.4. COMPLETION UNITS SHALL BE MOUNTED TO STRUCTURE USING EITHER A MOUNTING TAB AND STRUCTURAL ADHESIVE OR MECHANICAL CLAMP
   2.5. EACH AXIAL STRAIN GAGE REQUIRES 1 CHANNEL OF DATA ACQUISITION.
3. ACCELEROMETERS:
   3.1. ACCELEROMETERS SHALL BE MOUNTED TO THE TOP FACE OF THE BOTTOM FLANGE TO MEASURE ACCELERATION IN THE GLOBAL VERTICAL DIRECTION.
4. ACCELEROMETERS SHALL BE MOUNTED TO STRUCTURE USING EITHER STRUCTURAL ADHESIVE OR A MECHANICAL CLAMP
5. WEATHER STATION
   5.1. USED TO MEASURE AMBIENT AIR TEMPERATURE AND HUMIDITY
   5.2. WEATHER STATION SHALL BE MOUNTED DIRECTLY TO DATALOGGER CABINET.
   5.3. WEATHER STATION SHALL BE WIRED DIRECTLY INTO TCP/IP PORT ON CORE COMPUTER AT THE DATALOGGER.

MONITORING EQUIPMENT:
1. INSTRUMENTATION SHALL CONNECT INTO DATA ACQUISITION SYSTEMS - BDI STS4 TERMINAL NODES (4 AND 16 CHANNEL) VIA SENSOR CABLE.
2. DATA ACQUISITION SYSTEMS SHALL CONNECT TO DATA LOGGER VIA ARMORED CABLE THAT CONTAINS ETHERNET CABLE AND POWER CABLE.

EQUIPMENT INSTALLATION:
1. DATA LOGGER SHALL BE MOUNTED TO LIGHT STANDARD ON EAST SIDE OF PIER 3 USING STEEL BAND.
2. DATALOGGER POWER SHALL BE SUPPLIED USING LIGHT STANDARD POWER SOURCE
3. WEST AND EAST NODES SHALL BE INSTALLED ON GIRDER 2 AND GIRDER 4 RESPECTIVELY USING UNISTRUT MOUNTED TO GIRDER STIFFENERS.
4. ARMORED CABLE SHALL BE ROUTED ON INTERIOR OF GIRDER 4 BOTTOM FLANGE FROM EAST NODE TO PIER 3 THEN AROUND GIRDER 4 TO LOGGER.
5. ALL CABLES SHALL BE ANCHORED TO STRUCTURE USING P-CLAMPS FIXED TO BEAM CLAMPS CLAMPED TO FLANGES AND GIRDER STIFFENERS.

INSTRUMENTATION INSTALLATION:
1. ACCESS:
   1.1. PRELIMINARY ACCESS TO STRUCTURE SHALL BE ESTABLISHED BY A SPRAT L3 TECHNICIAN BY RAPPELLING OFF PIER 3 EAST LIGHT STANDARD AND NEARBY HANDRAIL POSTS. USING ROPE AND AID TECHNIQUES THE SPRAT L3 TECHNICIAN WILL ESTABLISH ANCHOR AND ROPES SYSTEMS ON THE BRIDGE INTERIOR TO ENABLE REMAINDER OF ROPE ACCESS PERSONNEL TO ACCESS INTERIOR OF STRUCTURE.
   1.2. LONG REBELAYS, AID CLIMBING, AND HORIZONTAL LIFELINES WILL BE USED TO NAVIGATE STRUCTURE ONCE ESTABLISHED ON INTERIOR OF STRUCTURE.
   1.3. BDI PERSONNEL AND SUBCONTRACTORS SHALL BE CONNECTED TO HORIZONTAL LIFELINE USING TWO LANYARDS WITH LOCKING CARABINERS ON EACH.
      1.3.1. TWO PERSONNEL MAXIMUM PER HORIZONTAL LIFE LINE.
2. ARMORED CABLE:
   2.1. CONTAINS QTY1 ETHERNET CABLE FOR DATA COMMUNICATION AND QTY2 12 AWG POWER CABLE.
3. SURFACE PREPARATION:
   3.1. PAINT REMOVAL:
      3.1.1. PERFORMED FOR STRAIN GAGES
      3.1.2. GAGE AREA SHALL BE MARKED.
      3.1.3. COATING SHALL BE MECHANICALLY REMOVED FROM 3" X 3" AREA OF GAGE INSTALLATION UNTIL SURFACE ABNORMALITIES OR IMPERFECTIONS ARE REMOVED.
      3.1.4. GAGE SHALL BE ATTACHED TO STEEL USING CAPACITIVE DISCHARGE SPOT WELDER. (NOT APPLICABLE FOR ACCELEROMETERS)
      3.1.5. ONCE GAGE INSTALLATION IS VERIFIED, AREA AND GAGE SHALL BE COVERED WITH ZINC SPRAY COATING. (NOT APPLICABLE FOR ACCELEROMETERS)
4. PROTECTION FROM VANDALISM
   4.1. DUE TO REQUIRED ACCESS FROM ROPES, MOST SENSORS ARE PROTECTED FROM VANDALISM.
5. PROTECTION FROM WEATHER
   5.1. ALL SENSORS SHALL BE IP66 INGRESS PROTECTION RATED OR BETTER.
6. PROTECTION FROM HUMIDITY
   6.1. ALL DATALOGGERS, NODE BOXES AND GAGE BREAKOUT BOXES WILL BE INSTALLED WITH DESICCANT PACKETS INSIDE TO PREVENT HUMIDITY BUILD UP.

FIELD DOCUMENTS:
1. ANY MODIFICATIONS TO SHOP DRAWINGS SHALL BE DOCUMENTED IN THE FIELD BY BDI ENGINEERS.
2. BDI RESERVES THE RIGHT TO MODIFY SENSOR LOCATIONS DUE TO FIELD CONDITIONS.
   2.1. ANY SIGNIFICANT CHANGES SHALL BE SUBMITTED FOR REVIEW AND APPROVAL.
3. PHOTOGRAPHS
   3.1. EACH SENSOR LOCATION SHALL BE PHOTOGRAPHED NEAR TO SHOW GAGE ID'S AND FAR TO SHOW GAGE PROXIMITY, LOCATION, AND ORIENTATION.
      3.1.1. SENSOR IDENTIFICATION WILL BE WRITTEN ON STRUCTURE ADJACENT TO SENSOR FOR PHOTO IDENTIFICATION.
      3.1.2. SENSORS INSTALLATION PHOTOS WILL BE TAKEN AFTER THE FOLLOWING STAGES:
         3.1.2.1. LOCATION MARKING
         3.1.2.2. SENSOR ATTACHMENT
         3.1.2.3. SENSOR COATING
      3.1.3. PHOTOS SHALL BE TAKEN OF COMPLETION UNITS AFTER MOUNTED IN PLACE.
      3.1.4. PHOTOS SHALL BE TAKEN OF LEAD WIRE ROUTING AND CABLE ROUTING.
   3.2. OVERALL BRIDGE PHOTOS SHALL BE TAKEN.
   3.3. PHOTOGRAPHS OF FINAL INSTALLATION OF DATA LOGGERS, JUNCTION BOXES, AND ANY ADDITIONAL HARDWARE SHALL BE TAKEN.
   3.4. PHOTOGRAPHS OF THE GENERAL AREA OF INSTRUMENTATION SHALL BE TAKEN.
   3.5. PHOTOGRAPHS OF INSIDE OF ALL DATALOGGERS, NODE BOXES AND JUNCTION BOXES SHALL BE TAKEN.

WARRANTY
1. ALL COMPONENTS OF SHMS ARE COVERED UNDER A MINIMUM OF 2 YEARS WARRANTY FROM DATE OF SUBSTANTIAL COMPLETION.

BDI
740 S PIERCE AVE, SUITE 15
LOUISVILLE, CO 80027
303.494.3230
WWW.BDITEST.COM

ISSUE

CLIENT

ISL
259 Robin Crescent
Saskatoon, SK S7L 6MB

PROJECT NAME

ISL ENGINEERING AND LAND SERVICES
DIEFENBAKER BRIDGE
STRUCTURAL HEALTH MONITORING SYSTEM

Drawn By:	KNR
Checked By:	JDS
Date:	2/16/18
Client No.:	
BDI No.:	170906-SK
SCALE:	NTS

GENERAL NOTES

SHM-02

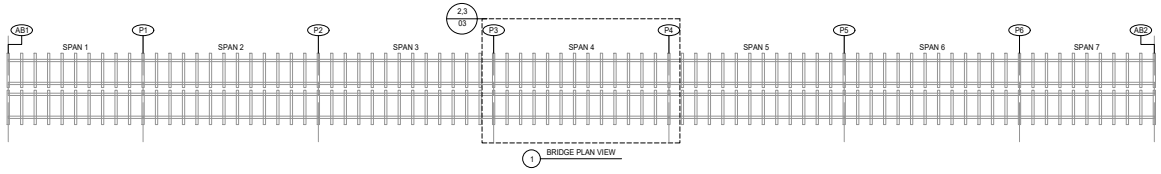

1 BRIDGE PLAN VIEW

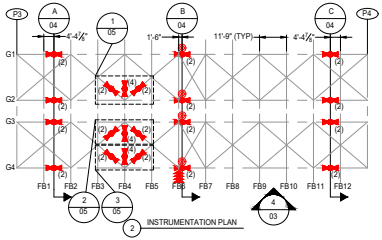

2 INSTRUMENTATION PLAN

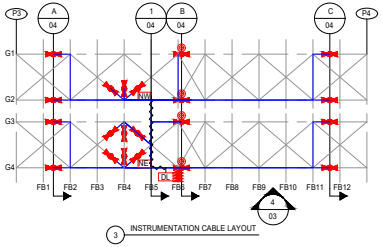

3 INSTRUMENTATION CABLE LAYOUT

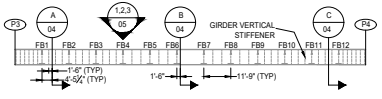

4 INSTRUMENTATION ELEVATION
LOOKING WEST

DESIGNATIONS:

- G# = GIRDER NUMBER
- AB# = ABUTMENT NUMBER
- P# = PIER NUMBER
- FB# = FLOORBEAM/DIAPHRAGM NUMBER IN SPAN 4

NOTES:

1. CROSS SECTION A SHALL BE CENTERED BETWEEN FIRST AND SECOND STIFFENERS NORTH OF FLOORBEAM 1 (FB1)
2. CROSS SECTION C SHALL BE CENTERED BETWEEN FIRST AND SECOND STIFFENERS SOUTH OF FB1
3. CROSS SECTION B SHALL BE CENTERED ON SPAN 4 AND CENTERED BETWEEN FB6 AND FB7
4. THE EAST AND WEST NODE BOXES (NE & NW) SHALL BE MOUNTED TO BRACING ALIGNED WITH FB5
5. THE DATALOGGER SHALL BE MOUNTED TO EAST CONCRETE BARRIER NEAR FLOORBEAM 5
6. WEATHER STATION SHALL BE MOUNTED TO THE DATALOGGER CABINET

WIRE LEGEND

BDI SENSOR CABLE (RED)	
ARMORED CABLE (NODE-TO-NODE = 90 FT) (EAST NODE-TO-LOGGER = 125 FT)	

SENSOR LEGEND	TOTAL COUNTS
WELDABLE FOIL AXIAL STRAIN GAGE	(48)
ACCELEROMETER	(4)
WEATHER STATION	(1)
TOTAL	(53)

BDI
740 S PIERCE AVE, SUITE 15
LOUISVILLE, CO 80027
303.494.3230
WWW.BDITEST.COM

ISSUE

CLIENT

ISL
259 Robin Crescent
Saskatoon, SK S7L 6M8

PROJECT NAME

ISL ENGINEERING AND LAND SERVICES
DIEFENBAKER BRIDGE
STRUCTURAL HEALTH MONITORING SYSTEM

Drawn By:	KNR
Checked By:	JDS
Date:	2/16/18
Client No.:	
BDI No.:	170906-SK
SCALE:	NTS

INSTRUMENTATION PLAN AND ELEVATION

SHM-03

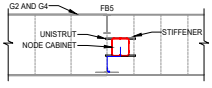

2 NODE INSTALLATION
LOOKING EAST

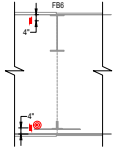

3 G2 & FB6 ELEVATION

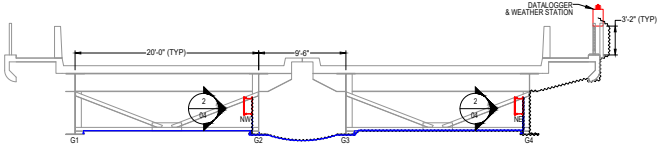

1 FLOORBEAM 5 CROSS SECTION
LOOKING NORTH

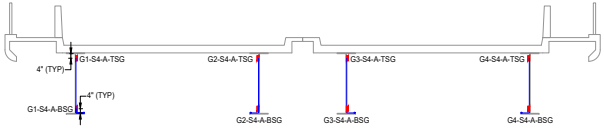

A CROSS SECTION A
LOOKING NORTH

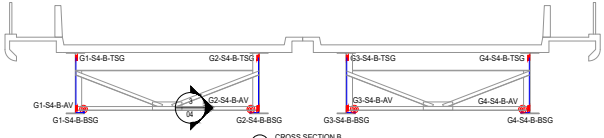

B CROSS SECTION B
LOOKING NORTH

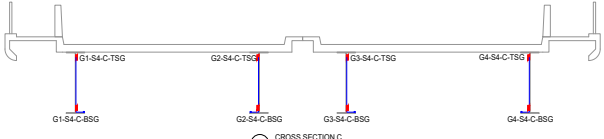

C CROSS SECTION C
LOOKING NORTH

SENSOR NAMING CONVENTION:
GIRDER # - SPAN # - SECTION ID - SENSOR POSITION & TYPE

- GIRDER #
  - G1 = GIRDER 1
  - G2 = GIRDER 2
  - G3 = GIRDER 3
  - G4 = GIRDER 4
- SPAN #
  - S4 = SPAN 4
- SECTION ID
  - A = SECTION NEAR PIER 3
  - A1 = SOUTHERN-MOST BRACE SECTION (DIAGONAL BRACE)
  - A2 = MIDDLE BRACE (TRANSVERSE BRACE)
  - A3 = NORTHERN-MOST BRACE SECTION (DIAGONAL BRACE)
  - B = MIDSPAN SECTION
  - C = SECTION NEAR PIER 4
- SENSOR POSITION & TYPE
  - TSG = TOP STRAIN GAGE
  - BSG = BOTTOM STRAIN GAGE
  - TSSG = TOP STRAIN GAGE ON SOUTH SIDE OF MEMBER
  - TNSG = TOP STRAIN GAGE ON NORTH SIDE OF MEMBER
  - BSSG = BOTTOM STRAIN GAGE ON SOUTH SIDE OF MEMBER
  - BNSG = BOTTOM STRAIN GAGE ON NORTH SIDE OF MEMBER
  - AV = ACCELEROMETER MEASURING VERTICAL VIBRATION

NOTES:

1. STRAIN GAGES ON GIRDER 1 & GIRDER 3 SHALL BE INSTALLED ON THE EAST FACE OF THE WEB.
2. STRAIN GAGES ON GIRDER 2 & GIRDER 4 SHALL BE INSTALLED ON THE WEST FACE OF THE WEB.
3. TOP STRAIN GAGES SHALL BE INSTALLED AS CLOSE TO THE BOTTOM OF THE TOP FLANGE AS POSSIBLE. EXACT DIMENSION SHALL BE DETERMINED IN THE FIELD.
4. BOTTOM STRAIN GAGES SHALL BE INSTALLED AS CLOSE TO THE TOP OF THE BOTTOM FLANGE AS POSSIBLE. EXACT DIMENSION SHALL BE DETERMINED IN THE FIELD.
5. ACCELEROMETERS SHALL BE INSTALLED ON THE BOTTOM OF THE TRANSVERSE BRACE ADJACENT TO CROSS SECTION B. THEY SHALL BE CLAMPED TO THE EDGE OF THE BRACE FLANGE.
6. NODES SHALL BE INSTALLED ON GIRDER 2 AND GIRDER 4 USING UNISTRUT CLAMPED TO VERTICAL STIFFENERS.
7. CABLES SHALL BE ROUTED ALONG TOP EDGE OF GIRDER BOTTOM FLANGE USING BEAM CLAMPS AND P-CLAMPS CLAMPED TO VERTICAL STIFFENERS.
8. QUARTER ARM COMPLETION UNITS SHALL BE MOUNTED TO BEAM CLAMPS ON NEAREST VERTICAL STIFFENER.
9. DATA LOGGER SHALL BE MOUNTED TO UNISTRUT ANCHORED TO CONCRETE AND BAND STRAPPED TO HANDRAIL.

WIRE LEGEND

	BDI SENSOR CABLE (RED)
	ARMORED CABLE

SENSOR LEGEND	TOTAL COUNTS
STRAIN TRANSDUCER	(24)
ACCELEROMETER	(4)
TOTAL	(28)

BDI
740 S PIERCE AVE, SUITE 15
LOUISVILLE, CO 80027
303.494.3230
WWW.BDITEST.COM

ISSUE

CLIENT

ISL
259 Robin Crescent
Saskatoon, SK S7L 6M8

PROJECT NAME

ISL ENGINEERING AND LAND SERVICES
DIEFENBAKER BRIDGE
STRUCTURAL HEALTH MONITORING SYSTEM

Drawn By:	KNR
Checked By:	JDS
Date:	2/16/18
Client No.:	
BDI No.:	170906-SK
SCALE:	NTS

INSTRUMENTATION
CROSS SECTIONS
SHM-04

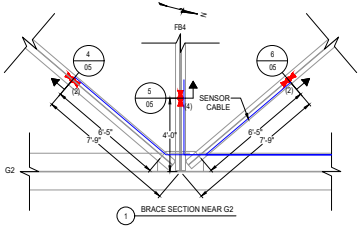

1 BRACE SECTION NEAR G2

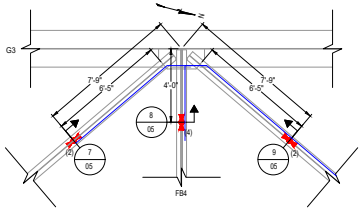

2 BRACE SECTION NEAR G3

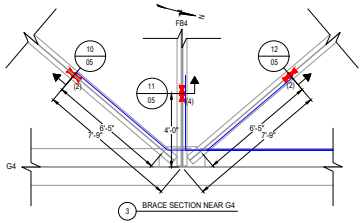

3 BRACE SECTION NEAR G4

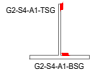

4 G3-S4-A1
LOOKING WEST

7 G3-S4-A1
LOOKING WEST

10 G4-S4-A1
LOOKING WEST

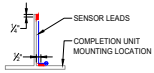

13 DIAGONAL BRACE SENSOR LOCATIONS
LOOKING WEST

5 G3-S4-A2
LOOKING WEST

8 G3-S4-A2
LOOKING WEST

11 G4-S4-A2
LOOKING WEST

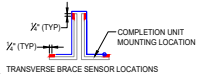

14 TRANSVERSE BRACE SENSOR LOCATIONS
LOOKING WEST

DESIGNATIONS:

- G# = GIRDER NUMBER
- AB# = ABUTMENT NUMBER
- P# = PIER NUMBER
- FB# = FLOORBEAM/DIAPHRAGM NUMBER IN SPAN 4

SENSOR NAMING CONVENTION:

GIRDER # - SPAN # - SECTION ID - SENSOR POSITION & TYPE

- GIRDER #
  - G1 = GIRDER 1
  - G2 = GIRDER 2
  - G3 = GIRDER 3
  - G4 = GIRDER 4
- SPAN #
  - S4 = SPAN 4
- SECTION ID
  - A = SECTION NEAR PIER 3
  - A1 = SOUTHERN-MOST BRACE SECTION (DIAGONAL BRACE)
  - A2 = MIDDLE BRACE (TRANSVERSE BRACE)
  - A3 = NORTHERN-MOST BRACE SECTION (DIAGONAL BRACE)
  - B = MIDSPAN SECTION
  - C = SECTION NEAR PIER 4
- SENSOR POSITION & TYPE
  - TSG = TOP STRAIN GAGE
  - BSG = BOTTOM STRAIN GAGE
  - TSSG = TOP STRAIN GAGE ON SOUTH SIDE OF MEMBER
  - TNSG = TOP STRAIN GAGE ON NORTH SIDE OF MEMBER
  - BSSG = BOTTOM STRAIN GAGE ON SOUTH SIDE OF MEMBER
  - BNSG = BOTTOM STRAIN GAGE ON NORTH SIDE OF MEMBER
  - AV = ACCELEROMETER MEASURING VERTICAL VIBRATION

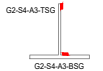

6 G3-S4-A3
LOOKING WEST

9 G3-S4-A3
LOOKING WEST

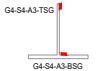

12 G4-S4-A3
LOOKING WEST

SENSOR LEGEND	TOTAL COUNTS
STRAIN TRANSDUCER	(24)

BDI
740 S PIERCE AVE, SUITE 15
LOUISVILLE, CO 80027
303.494.3230
WWW.BDITEST.COM

ISSUE

CLIENT

ISL
259 Robin Crescent
Saskatoon, SK S7L 6M8

PROJECT NAME

ISL ENGINEERING AND LAND SERVICES
DIEFENBAKER BRIDGE
STRUCTURAL HEALTH MONITORING SYSTEM

Drawn By:	KNR
Checked By:	JDS
Date:	2/16/18
Client No.:	
BDI No.:	170906-SK
SCALE:	NTS

BRACING
INSTRUMENTATION SECTIONS
SHM-05

06

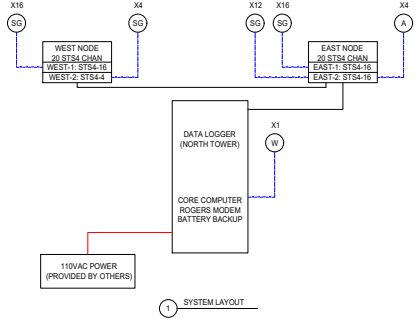

LEGEND

- ARMORED CABLE (ETHERNET & POWER)
- INSTRUMENTATION CABLE
- POWER CABLE FROM LIGHT STANDARD

- SG — UNIAXIAL STRAIN GAGE
- A — ACCELEROMETER
- W — HMP-60 TEMP/REL. HUMIDITY SENSOR

- X# — SENSOR QUANTITY
- X — SENSOR DESIGNATION

N-O-P-1
6 STS4 CHAN
STS4-4/16

- NODE BOX DESIGNATION
- NUMBER OF CHANNELS USED
- NODE SIZE

740 S PIERCE AVE, SUITE 15
LOUISVILLE, CO 80027
303.494.3230
WWW.BDITEST.COM

ISSUE

CLIENT

ISL
259 Robin Crescent
Saskatoon, SK S7L 6M8

PROJECT NAME

ISL ENGINEERING AND LAND SERVICES
DIEFENBAKER BRIDGE
STRUCTURAL HEALTH MONITORING SYSTEM

Drawn By:	KNR
Checked By:	JDS
Date:	2/16/18
Client No.:	
BDI No.:	170906-SK
SCALE:	NTS

SYSTEM LAYOUT

SHM-06

NODE BOX ID: EAST-1 (QTY 1 - 16CH) - ST54-16-T64-0142			
CHANNEL	SENSOR ID	CH INPUT	INSTRUMENTATION CABLE WIRING
1	G3-S4-A1-TSG [I2432] (60ft)	V EXC+	RED
		GND	BLACK
		SIG+	GREEN
		SIG-	WHITE
		SHLD	SHIELD
2	G3-S4-A1-BSG [I2433] (60ft)	V EXC+	RED
		GND	BLACK
		SIG+	GREEN
		SIG-	WHITE
		SHLD	SHIELD
3	G3-S4-A2-TSSG [I2434] (60ft)	V EXC+	RED
		GND	BLACK
		SIG+	GREEN
		SIG-	WHITE
		SHLD	SHIELD
4	G3-S4-A2-BSSG [I2435] (60ft)	V EXC+	RED
		GND	BLACK
		SIG+	GREEN
		SIG-	WHITE
		SHLD	SHIELD
5	G3-S4-A2-TNSG [I2436] (60ft)	V EXC+	RED
		GND	BLACK
		SIG+	GREEN
		SIG-	WHITE
		SHLD	SHIELD
6	G3-S4-A2-BNSG [I2437] (60ft)	V EXC+	RED
		GND	BLACK
		SIG+	GREEN
		SIG-	WHITE
		SHLD	SHIELD
7	G3-S4-A3-TSG [I2438] (60ft)	V EXC+	RED
		GND	BLACK
		SIG+	GREEN
		SIG-	WHITE
		SHLD	SHIELD
8	G3-S4-A3-BSG [I2439] (60ft)	V EXC+	RED
		GND	BLACK
		SIG+	GREEN
		SIG-	WHITE
		SHLD	SHIELD
9	G4-S4-A1-TSG [I2440] (40ft)	V EXC+	RED
		GND	BLACK
		SIG+	GREEN
		SIG-	WHITE
		SHLD	SHIELD
10	G4-S4-A1-BSG [I2441] (40ft)	V EXC+	RED
		GND	BLACK
		SIG+	GREEN
		SIG-	WHITE
		SHLD	SHIELD
11	G4-S4-A2-TSSG [I2442] (40ft)	V EXC+	RED
		GND	BLACK
		SIG+	GREEN
		SIG-	WHITE
		SHLD	SHIELD
12	G4-S4-A2-BSSG [I2443] (40ft)	V EXC+	RED
		GND	BLACK
		SIG+	GREEN
		SIG-	WHITE
		SHLD	SHIELD
13	G4-S4-A2-TNSG [I2444] (40ft)	V EXC+	RED
		GND	BLACK
		SIG+	GREEN
		SIG-	WHITE
		SHLD	SHIELD
14	G4-S4-A2-BNSG [I2445] (40ft)	V EXC+	RED
		GND	BLACK
		SIG+	GREEN
		SIG-	WHITE
		SHLD	SHIELD
15	G4-S4-A3-TSG [I2446] (40ft)	V EXC+	RED
		GND	BLACK
		SIG+	GREEN
		SIG-	WHITE
		SHLD	SHIELD
16	G4-S4-A3-BSG [I2447] (40ft)	V EXC+	RED
		GND	BLACK
		SIG+	GREEN
		SIG-	WHITE
		SHLD	SHIELD

NODE BOX ID: EAST-2 (QTY 1 - 16CH) - ST54-16-T64-0147			
CHANNEL	SENSOR ID	CH INPUT	INSTRUMENTATION CABLE WIRING
1	G3-S4-A-BSG [I2448] (90ft)	V EXC+	RED
		GND	BLACK
		SIG+	GREEN
		SIG-	WHITE
		SHLD	SHIELD
2	G3-S4-A-TSG [I2449] (90ft)	V EXC+	RED
		GND	BLACK
		SIG+	GREEN
		SIG-	WHITE
		SHLD	SHIELD
3	G4-S4-A-BSG [I2450] (70ft)	V EXC+	RED
		GND	BLACK
		SIG+	GREEN
		SIG-	WHITE
		SHLD	SHIELD
4	G4-S4-A-TSG [I2451] (70ft)	V EXC+	RED
		GND	BLACK
		SIG+	GREEN
		SIG-	WHITE
		SHLD	SHIELD
5	G3-S4-B-BSG [I2452] (60ft)	V EXC+	RED
		GND	BLACK
		SIG+	GREEN
		SIG-	WHITE
		SHLD	SHIELD
6	G3-S4-B-TSG [I2453] (70ft)	V EXC+	RED
		GND	BLACK
		SIG+	GREEN
		SIG-	WHITE
		SHLD	SHIELD
7	G4-S4-B-BSG [I2454] (40ft)	V EXC+	RED
		GND	BLACK
		SIG+	GREEN
		SIG-	WHITE
		SHLD	SHIELD
8	G4-S4-B-TSG [I2455] (54ft)	V EXC+	RED
		GND	BLACK
		SIG+	GREEN
		SIG-	WHITE
		SHLD	SHIELD
9	G3-S4-C-BSG [I2456] (125ft)	V EXC+	RED
		GND	BLACK
		SIG+	GREEN
		SIG-	WHITE
		SHLD	SHIELD
10	G3-S4-C-TSG [I2457] (125ft)	V EXC+	RED
		GND	BLACK
		SIG+	GREEN
		SIG-	WHITE
		SHLD	SHIELD
11	G4-S4-C-BSG [I2458] (110ft) +Therm	V EXC+	RED
		GND	RED (BLACK)
		SIG+	GREEN
		SIG-	GREEN (BLACK)
		TEMP +	WHITE
		TEMP -	WHITE (BLACK)
		SHLD	SHIELD
12	G4-S4-C-TSG [I2459] (110ft)	V EXC+	RED
		GND	BLACK
		SIG+	GREEN
		SIG-	WHITE
		SHLD	SHIELD
13	G1-S4-B-AV [A1256] (110ft)	V EXC+	RED
		GND	BLACK
		SIG+	GREEN
		SIG-	WHITE
		SHLD	SHIELD
14	G2-S4-B-AV [A1257] (90ft)	V EXC+	RED
		GND	BLACK
		SIG+	GREEN
		SIG-	WHITE
		SHLD	SHIELD
15	G3-S4-B-AV [A1258] (60ft)	V EXC+	RED
		GND	BLACK
		SIG+	GREEN
		SIG-	WHITE
		SHLD	SHIELD
16	G4-S4-B-AV [A1259] (40ft)	V EXC+	RED
		GND	BLACK
		SIG+	GREEN
		SIG-	WHITE
		SHLD	SHIELD

SENSOR NAMING CONVENTION:

GIRDER # - SPAN # - SECTION ID - SENSOR POSITION & TYPE

- GIRDER #
  - G1 = GIRDER 1
  - G2 = GIRDER 2
  - G3 = GIRDER 3
  - G4 = GIRDER 4
- SPAN #
  - S4 = SPAN 4
- SECTION ID
  - A = SECTION NEAR PIER 3
  - A1 = SOUTHERN-MOST BRACE SECTION (DIAGONAL BRACE)
  - A2 = MIDDLE BRACE (TRANSVERSE BRACE)
  - A3 = NORTHERN-MOST BRACE SECTION (DIAGONAL BRACE)
  - B = MIDSPAN SECTION
  - C = SECTION NEAR PIER 4
- SENSOR POSITION & TYPE
  - TSG = TOP STRAIN GAGE
  - BSG = BOTTOM STRAIN GAGE
  - TSSG = TOP STRAIN GAGE ON SOUTH SIDE OF MEMBER
  - TNSG = TOP STRAIN GAGE ON NORTH SIDE OF MEMBER
  - BSSG = BOTTOM STRAIN GAGE ON SOUTH SIDE OF MEMBER
  - BNSG = BOTTOM STRAIN GAGE ON NORTH SIDE OF MEMBER
  - AV = ACCELEROMETER MEASURING VERTICAL VIBRATION

BDI
STRUCTURAL HEALTH MONITORING SOLUTIONS
740 S PIERCE AVE, SUITE 15
LOUISVILLE, CO 80027
303.494.3230
WWW.BDITEST.COM

ISSUE

CLIENT

ISL
259 Robin Crescent
Saskatoon, SK S7L 6M8

PROJECT NAME

ISL ENGINEERING AND LAND SERVICES
DIEFENBAKER BRIDGE
STRUCTURAL HEALTH MONITORING SYSTEM

Drawn By:	KNR
Checked By:	JDS
Date:	2/16/18
Client No.:	
BDI No.:	170906-SK
SCALE:	NTS

EAST NODE WIRING TABLES

SHM-07

NODE BOX ID: WEST-1 [QTY 1 - 16CH] - ST54-16-TE4-0111			
CHANNEL	SENSOR ID	CH INPUT	INSTRUMENTATION CABLE WIRING
1	G1-54-A-BSG [Q2460] (60ft) +Therm	V EXC+	RED
		GND	RED (BLACK)
		SIG+	GREEN
		SIG-	GREEN (BLACK)
		TEMP +	WHITE
		TEMP -	WHITE (BLACK)
		SHLD	SHIELD
2	G1-54-A-TSG [Q2461] (60ft)	V EXC+	RED
		GND	BLACK
		SIG+	GREEN
		SIG-	WHITE
		SHLD	SHIELD
3	G2-54-A-BSG [Q2462] (70ft)	V EXC+	RED
		GND	BLACK
		SIG+	GREEN
		SIG-	WHITE
		SHLD	SHIELD
4	G2-54-A-TSG [Q2463] (70ft)	V EXC+	RED
		GND	BLACK
		SIG+	GREEN
		SIG-	WHITE
		SHLD	SHIELD
5	G1-54-B-BSG [Q2464] (60ft)	V EXC+	RED
		GND	BLACK
		SIG+	GREEN
		SIG-	WHITE
		SHLD	SHIELD
6	G1-54-B-TSG [Q2465] (70ft)	V EXC+	RED
		GND	BLACK
		SIG+	GREEN
		SIG-	WHITE
		SHLD	SHIELD
7	G2-54-B-BSG [Q2466] (40ft) +Therm	V EXC+	RED
		GND	RED (BLACK)
		SIG+	GREEN
		SIG-	GREEN (BLACK)
		TEMP +	WHITE
		TEMP -	WHITE (BLACK)
		SHLD	SHIELD
8	G2-54-B-TSG [Q2467] (50ft) +Therm	V EXC+	RED
		GND	RED (BLACK)
		SIG+	GREEN
		SIG-	GREEN (BLACK)
		TEMP +	WHITE
		TEMP -	WHITE (BLACK)
		SHLD	SHIELD

NODE BOX ID: WEST-1 [QTY 1 - 16CH] - ST54-16-TE4-0111			
9	G2-54-A1-TSG [Q2468] (40ft)	V EXC+	RED
		GND	BLACK
		SIG+	GREEN
		SIG-	WHITE
		SHLD	SHIELD
10	G2-54-A1-BSG [Q2469] (40ft)	V EXC+	RED
		GND	BLACK
		SIG+	GREEN
		SIG-	WHITE
		SHLD	SHIELD
11	G2-54-A2-TSG [Q2470] (40ft)	V EXC+	RED
		GND	BLACK
		SIG+	GREEN
		SIG-	WHITE
		SHLD	SHIELD
12	G2-54-A2-BSG [Q2471] (40ft)	V EXC+	RED
		GND	BLACK
		SIG+	GREEN
		SIG-	WHITE
		SHLD	SHIELD
13	G2-54-A2-TNSG [Q2472] (40ft)	V EXC+	RED
		GND	BLACK
		SIG+	GREEN
		SIG-	WHITE
		SHLD	SHIELD
14	G2-54-A2-BNSG [Q2473] (40ft)	V EXC+	RED
		GND	BLACK
		SIG+	GREEN
		SIG-	WHITE
		SHLD	SHIELD
15	G2-54-A3-TSG [Q2474] (40ft)	V EXC+	RED
		GND	BLACK
		SIG+	GREEN
		SIG-	WHITE
		SHLD	SHIELD
16	G2-54-A3-BSG [Q2475] (40ft)	V EXC+	RED
		GND	BLACK
		SIG+	GREEN
		SIG-	WHITE
		SHLD	SHIELD

NODE BOX ID: WEST-2 [QTY 1 - 4CH] - TE4-0122			
CHANNEL	SENSOR ID	CH INPUT	INSTRUMENTATION CABLE WIRING
1	G1-54-C-BSG [Q2476] (125ft)	V EXC+	RED
		GND	BLACK
		SIG+	GREEN
		SIG-	WHITE
		SHLD	SHIELD
2	G1-54-C-TSG [Q2477] (145ft)	V EXC+	RED
		GND	BLACK
		SIG+	GREEN
		SIG-	WHITE
		SHLD	SHIELD
3	G2-54-C-BSG [Q2478] (110ft)	V EXC+	RED
		GND	BLACK
		SIG+	GREEN
		SIG-	WHITE
		SHLD	SHIELD
4	G2-54-C-TSG [Q2479] (110ft)	V EXC+	RED
		GND	BLACK
		SIG+	GREEN
		SIG-	WHITE
		SHLD	SHIELD

SENSOR NAMING CONVENTION:

GIRDER # - SPAN # - SECTION ID - SENSOR POSITION & TYPE

- GIRDER #
  - G1 = GIRDER 1
  - G2 = GIRDER 2
  - G3 = GIRDER 3
  - G4 = GIRDER 4
- SPAN #
  - S4 = SPAN 4
- SECTION ID
  - A = SECTION NEAR PIER 3
  - A1 = SOUTHERN-MOST BRACE SECTION (DIAGONAL BRACE)
  - A2 = MIDDLE BRACE (TRANSVERSE BRACE)
  - A3 = NORTHERN-MOST BRACE SECTION (DIAGONAL BRACE)
  - B = MIDSPAN SECTION
  - C = SECTION NEAR PIER 4
- SENSOR POSITION & TYPE
  - TSG = TOP STRAIN GAGE
  - BSG = BOTTOM STRAIN GAGE
  - TSNG = TOP STRAIN GAGE ON SOUTH SIDE OF MEMBER
  - TNSG = TOP STRAIN GAGE ON NORTH SIDE OF MEMBER
  - BSSG = BOTTOM STRAIN GAGE ON SOUTH SIDE OF MEMBER
  - BNSG = BOTTOM STRAIN GAGE ON NORTH SIDE OF MEMBER
  - AV = ACCELEROMETER MEASURING VERTICAL VIBRATION

BDI
740 S PIERCE AVE, SUITE 15
LOUISVILLE, CO 80027
303.494.3230
WWW.BDITEST.COM

ISSUE

CLIENT

ISL
259 Robin Crescent
Saskatoon, SK S7L 6MB

PROJECT NAME

ISL ENGINEERING AND LAND SERVICES
DIEFENBAKER BRIDGE
STRUCTURAL HEALTH MONITORING SYSTEM

Drawn By:	KNR
Checked By:	JDS
Date:	2/16/18
Client No.:	
BDI No.:	170906-SK
SCALE:	NTS

WEST NODE WIRING TABLES

SHM-08

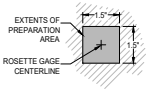

PREPARATION INSTRUCTIONS:

1. AREA SHALL BE THOROUGHLY DEGREASED.
2. PAINT SHALL BE REMOVED FROM PREPARATION AREA
3. SURFACE SHALL BE MECHANICALLY ABRADED TO ACHIEVE A SMOOTH FINISH, REMOVING ANY PITTING OR IMPERFECTIONS TO SSPC STANDARD SP-11.

1 PREPARATION AREA - UNIAXIAL STRAIN GAGE

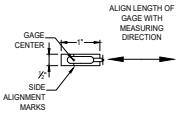

2A UNIAXIAL STRAIN GAGE

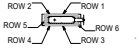

2B UNIAXIAL GAGE TACK PATTERN

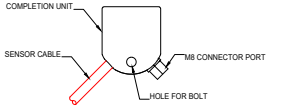

2C COMPLETION UNIT

WELDABLE UNIAXIAL GAGE INSTALLATION:

1. CLEARLY MARK OUT GAGE LOCATION WITHIN PREPARATION AREA.
2. WIPE PREPARATION AREA WITH CLEAN CLOTH OR GAUZE PAD TO ENSURE IT IS FREE OF CONTAMINANTS.
3. REMOVE GAGE FROM PACKAGING, INSPECT FOR ANY IMPERFECTIONS, AND POSITION INTO PROPER LOCATION.
   - 3.1. GIRDER INSTALLATION: TIP OF GAGE SHALL BE POINTING NORTH.
   - 3.2. GIRDER 2 BRACE INSTALLATION: TIP OF GAGE SHALL BE POINTING WEST.
   - 3.2. GIRDER 3 BRACE INSTALLATION: TIP OF GAGE SHALL BE POINTING EAST.
   - 3.2. GIRDER 4 BRACE INSTALLATION: TIP OF GAGE SHALL BE POINTING WEST.
4. TO KEEP GAGE IN PLACE, TAPE DOWN TO STRUCTURE AT BASE OF GAGE WHERE WIRES ENTER SHIM.
5. USING CAPACITIVE DISCHARGE SPOT WELDER, TACK GAGE IN PLACE WITH ONE WELD AT EACH OF THE SIDE ALIGNMENT MARKS.
6. CAREFULLY REMOVE TAPE AND ENSURE GAGE IS POSITIONED IN PROPER LOCATION.
7. CONTINUE TO WELD GAGE IN PLACE FOLLOWING PATTERN OUTLINED BELOW AND SHOWN IN SECTION 2B.
   - 7.1. ROW 1 FROM SIDE ALIGNMENT MARK TOWARD LEAD WIRES.
   - 7.2. ROW 2 FROM SIDE ALIGNMENT MARK TOWARD SENSOR TIP.
   - 7.3. ROW 3 FROM SIDE ALIGNMENT MARK TOWARD LEAD WIRES.
   - 7.4. ROW 4 FROM SIDE ALIGNMENT MARK TOWARD SENSOR TIP.
   - 7.5. ROWS 5 ACROSS GAGE TOP.
   - 7.6. ROW 6 ACROSS GAGE BOTTOM.
8. COMPLETE INSTALLATION BY ADDING A SECOND ROW OF WELDS OUTBOARD OF THE FIRST ROW.
9. COAT SENSOR AND PREPPED SURFACE WITH COLD GALVANIZING SPRAY PAINT.
10. CONDUCT VISUAL INSPECTION TO ENSURE GAGE IS SECURELY WELDED INTO THE PROPER LOCATION.
11. ROUTE LEAD WIRES TO CORRESPONDING COMPLETION UNIT AND PLUG M8 CONNECTOR INTO COMPLETION UNIT.
12. ATTACH SMALL ZIP TIES TO LEAD WIRES INCREMENTALLY AND GLUE ZIP TIES TO STRUCTURE FIRST USING LOCTITE 410 TO PROVIDE LEAD WIRE STRAIN RELIEF AND ROUTE THE LEAD CABLE TO THE COMPLETION UNIT.
13. COMPLETION UNITS SHALL BE MOUNTED TO STRUCTURE USING MECHANICAL CLAMP.

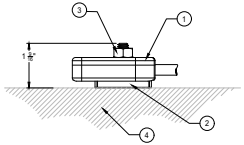

1. BDI UNIAXIAL ACCELEROMETER
2. 1/4"-20 THREADED MOUNTING TAB
3. 1/4"-20 STAINLESS STEEL NUT
4. MOUNTING SURFACE (TOP OF BOTTOM FLANGE)

FOOTNOTES - MOUNTING APPLICATION
1. ACCELEROMETERS TO BE MOUNTED DIRECTLY TO SURFACED PREPPED AREA WITH STRUCTURAL ADHESIVE OR MECHANICAL CLAMP.

1 BDI ACCELEROMETER INSTALLATION

BDI
740 S PIERCE AVE, SUITE 15
LOUISVILLE, CO 80027
303.494.3230
WWW.BDITEST.COM

ISSUE

CLIENT

ISL
259 Robin Crescent
Saskatoon, SK S7L 6M8

PROJECT NAME

ISL ENGINEERING AND LAND SERVICES
DIEFENBAKER BRIDGE
STRUCTURAL HEALTH MONITORING SYSTEM

Drawn By:	KNR
Checked By:	JDS
Date:	2/16/18
Client No.:	
BDI No.:	170906-SK
SCALE:	NTS

SENSOR INSTALLATION DETAILS

SHM-09

BDI
Boulder Dynamics Instrumentation
74 Lafayette Ave, Suite 501
Lowerville, CO 80027
(303) 440-3300
WWW.BDISTECH.COM

ISSUE

CLIENT
ISL
250 Rand Crescent
Saskatoon, SK S7L 6M8

PROJECT NAME
ISL ENGINEERING AND LAND SERVICES
DIEFENBAKER BRIDGE
STRUCTURAL HEALTH MONITORING SYSTEM

Drawn By: KNR
Checked By: JDS
Date: 2/9/2018
Client No.:
BDI No.: 170906.SK
SCALE: NTS

SYSTEM OPERATION
SHEET
SHM-10

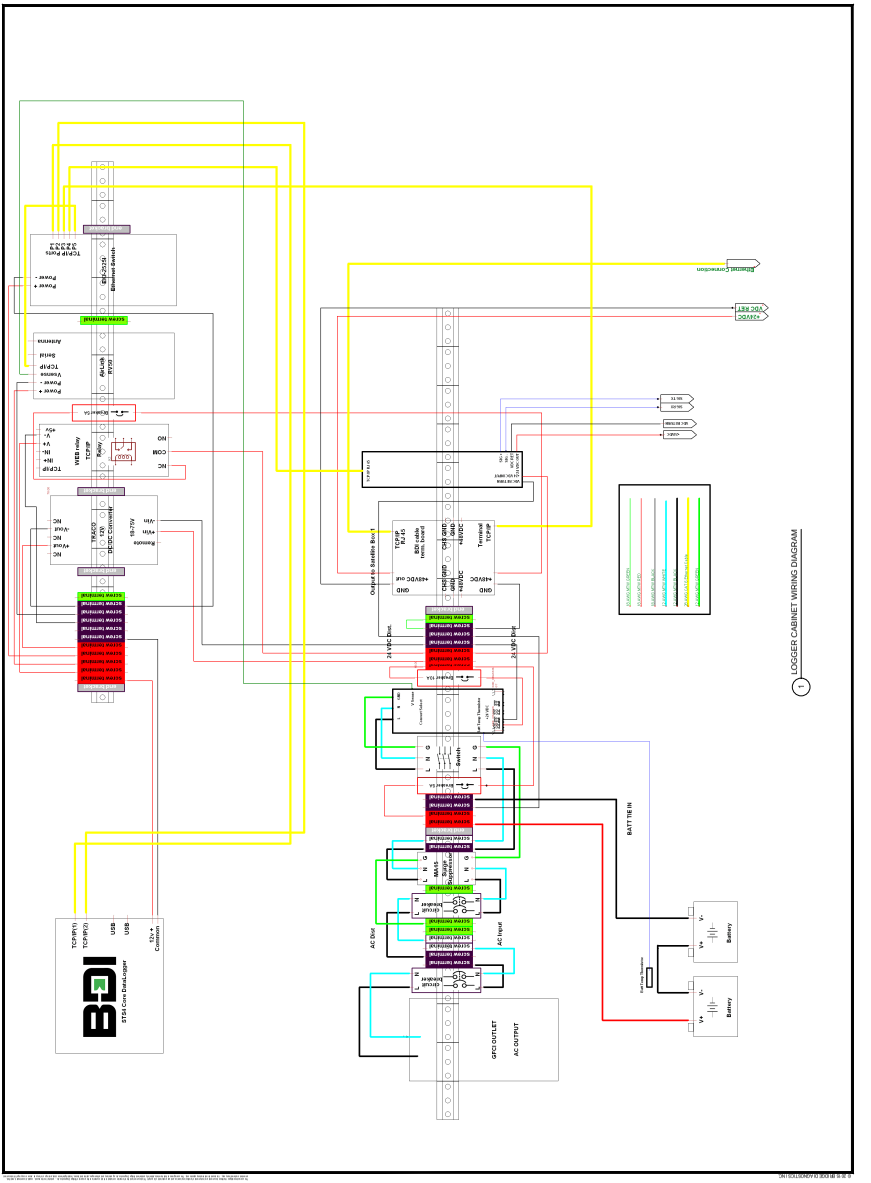
LOGGER CABINET WIRING DIAGRAM
STGI Core Data-Logger
Ethernet Switch
Power Supply
Battery
Battery
AC Input
AC Distr
AC OUTPUT
GFCI OUTLET
BATT THERM
24 VDC Bus
24 VDC Bus
Output to Bundle Box 1
Terminal
TCP/IP
RS-485
Modbus
Isolator
Relay
Switch
Breaker
Terminal Strip
Fuse
Ground Bus
Ground Bar
Power +
Power -
Ethernet
Shield
Antenna
TCP/IP Ports
Ethernet Switch
Power Supply
Relay
Isolator
Fuse
Ground Bus
Ground Bar
Terminal Strip
Battery
Battery
Breaker
Switch
Terminal
Terminal
Terminal

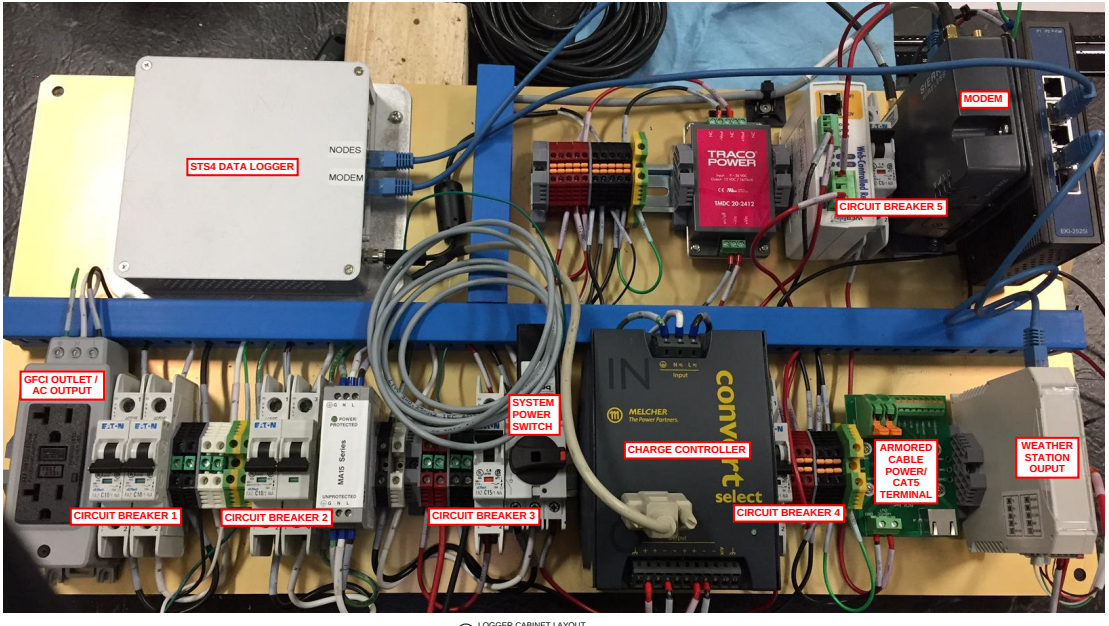

1 LOGGER CABINET LAYOUT

DATA LOGGER PANEL LEGEND:

STS4 DATA LOGGER: Computer that operates data acquisition system for data collection. Controls and collects data from remote nodes via CAT5 cable connection.
ARMORED CABLE POWER/CAT5 TERMINAL: Terminal Board for armored cable that connects STS4 Data Logger to STS4 Nodes.
WEATHER STATION INPUT TERMINAL: Weather station terminal port.
MODEM: Allows remote connectivity to STS4 Data Logger.
GFCI OUTLET / AC OUPUT: Outlet for battery heat blanket or other external device such as a laptop.
SYSTEM POWER SWITCH: (OFF = Horizontal, ON = Vertical) Turns power ON/OFF to STS4 Data Logger, Nodes, Modem, and Weather Station. When in the OFF position power is still live from AC Power Source or Batteries unless appropriate Circuit Breakers are flipped.
CIRCUIT BREAKER 1: (OFF = Down/Green, ON = Up/Red) ON position supplies power to the GFCI Outlet.
CIRCUIT BREAKER 2: (OFF = Down/Green, ON = Up/Red) ON position enables power to be supplied from the AC Power Source.
CIRCUIT BREAKER 3: (OFF = Down/Green, ON = Up/Red) ON position enables power to be supplied from the Batteries and for the Batteries to be charged.
CIRCUIT BREAKER 4: (OFF = Down/Green, ON = Up/Red) ON position enables power to be supplied to the 24V DC Power supply which sends power to the STS4 Data Logger, Nodes, Modem, and Weather Station.
CIRCUIT BREAKER 5: (OFF = Down/Green, ON = Up/Red) ON position enables power to be supplied to the STS4 Nodes.

BDI
740 S PIERCE AVE, SUITE 15
LOUISVILLE, CO 80027
303.494.3230
WWW.BDITEST.COM

ISSUE

CLIENT
ISL
259 Robin Crescent
Saskatoon, SK S7L 6M8

PROJECT NAME
ISL ENGINEERING AND LAND SERVICES
DIEFENBAKER BRIDGE
STRUCTURAL HEALTH MONITORING SYSTEM

Drawn By:	KNR
Checked By:	JDS
Date:	2/16/18
Client No.:	
BDI No.:	170906-SK
SCALE:	NTS

SYSTEM OPERATION
SHEET 2
SHM-11

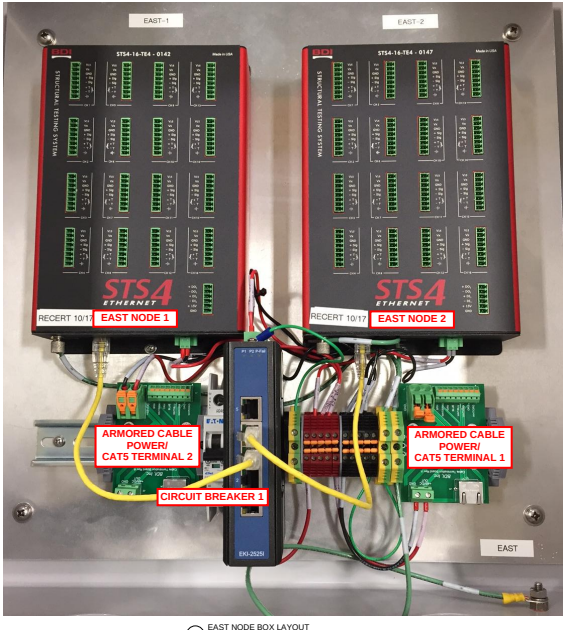

1 EAST NODE BOX LAYOUT

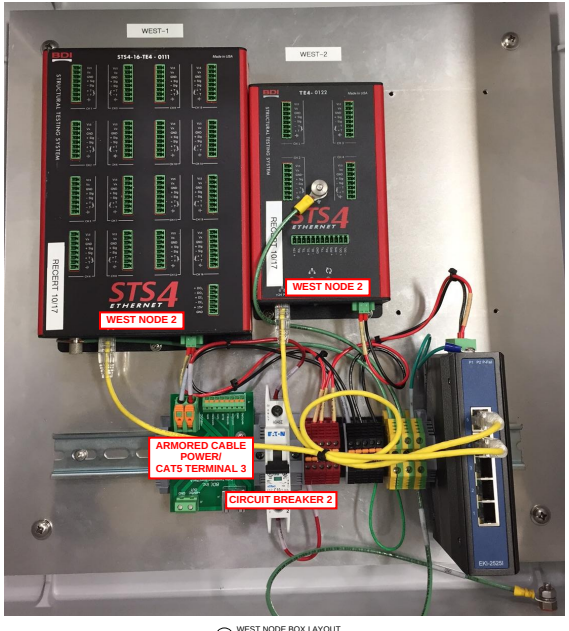

2 WEST NODE BOX LAYOUT

NODE LEGEND:

EAST NODE 1: See SHM-07 for sensor wiring inputs.
EAST NODE 2: See SHM-07 for sensor wiring inputs.
WEST NODE 1: See SHM-08 for sensor wiring inputs.
WEST NODE 2: See SHM-08 for sensor wiring inputs.
ARMORED CABLE POWER/CAT5 TERMINAL 1: Terminal Board for armored cable that connects STS4 Data Logger to STS4 East Nodes.
ARMORED CABLE POWER/CAT5 TERMINAL 2: Terminal Board for armored cable that routes connection from STS4 East Nodes to STS4 West Nodes.
ARMORED CABLE POWER/CAT5 TERMINAL 3: Terminal Board for armored cable from STS4 East Nodes to STS4 West Nodes.
CIRCUIT BREAKER 1: (OFF = Down/Green, ON = Up/Red) ON position enables power to be supplied to the STS4 East Nodes.
CIRCUIT BREAKER 2: (OFF = Down/Green, ON = Up/Red) ON position enables power to be supplied to the STS4 West Nodes.

BDI
740 S PIERCE AVE, SUITE 15
LOUISVILLE, CO 80027
303.494.3230
WWW.BDITEST.COM

ISSUE

CLIENT

ISL
259 Robin Crescent
Saskatoon, SK S7L 6M8

PROJECT NAME

ISL ENGINEERING AND LAND SERVICES
DIEFENBAKER BRIDGE
STRUCTURAL HEALTH MONITORING SYSTEM

Drawn By:	KNR
Checked By:	JDS
Date:	2/16/18
Client No.:	
BDI No.:	170906-SK
SCALE:	NTS

SYSTEM OPERATION
SHEET 3
SHM-12

BASE SYSTEM OPERATION:
BDI monitoring systems can be configured to collect data in several modes. At the root of the system operation there is global sample rate, which is fixed for all sensors
Global Sample Rate: 50Hz

FILE STRUCTURE:
All data is written to TDMS (*.tdms) files. TDMS files can be opened in MS Excel using a tdms extension found on the National Instrumentations website at the link below.

Filename Structure: ProjectName_Test Run #_File Date (Month_Day_Year)_File Writing Time (HH_MM_SS)_Data Output Type.tdms

MS Excel TDMS extension: http://www.ni.com/example/27944/en/

DATA OUTPUT DETAILS:
Data output types from BDI monitoring systems are defined in a Test Specification unique to the project.
Test Specification implement on: 2/13/2018

LIVE-LOAD DATA:
Normal data is typically used when conduction a live-load test or during commissioning of the system to verify all sensors are performing correctly.

- Filename: ########_Normal Data_AllNormal.tdms
- Records and writes 50Hz continuous data on QTY7 sensors:
  - G1-S4-A-BSG
  - G1-S4-A-TSG
  - G1-S4-B-AV
  - G1-S4-B-BSG
  - G1-S4-B-TSG
  - G1-S4-C-BSG
  - G1-S4-C-TSG

TREND DATA:
Trend data is typically used to store a reduced set of data over an extended period of time.
Trend Data Sample Rate: One point every 30 seconds (0.033Hz)

- Filename is appended with "Decimate_AllDec"
- Data is sampled at the global sample rate then decimated
- Average, Maximum, and Minimum values are written for all sensors at the trend data sample rate.

RAINFLOW DATA:
Rainflow data is typically used to assess stress cycles
Rain Flow Output Rate: One file every 24 hours

- Filename is appended with "Rainflow_AllRainflow"
- Data is based on the global sample rate
- Rainflow data is generated according to ASTM E1049-85 Section 5.4.4 for all strain sensors.
- One rainflow data file is written at the rain flow output rate.
- Cycling counting for the 24-hour period starts and ends at midnight.
- Rainflow cycle counts are sorted into 13 mean bins and 7 range bins for all strain sensors
- No rainflow cycles are counted for cycles less than 12.5 microstrain.
- Mean Bins:
  1) -150: -150 to -137.5 microstrain
  2) -125: -137.5 to -112.5 microstrain
  3) -100: -112.5 to -87.5 microstrain
  4) -75: -87.5 to 37.5 microstrain
  5) -50: -62.5 to -37.5 microstrain
  6) -25: -37.5 to -12.5 microstrain
  7) 0: -12.5 to 12.5 microstrain
  8) 25: 12.5 to 37.5 microstrain
  9) 50: 37.5 to 62.5 microstrain
  10) 75: 62.5 to 87.5 microstrain
  11) 100: 87.5 to 112.5 microstrain
  12) 125: 112.5 to 137.5 microstrain
  13) 150: 137.5 to 150 microstrain
- Range Bins:
  1) 0: 0 to 12.5 microstrain
  2) 25: 12.5 to 37.5 microstrain
  3) 50: 37.5 to 62.5 microstrain
  4) 75: 62.5 to 87.5 microstrain
  5) 100: 87.5 to 112.5 microstrain
  6) 125: 112.5 to 137.5 microstrain
  7) 150: 137.5 to 162.5 microstrain

EVENT DATA:
System has the ability to record data associated with "events". This allows the user to record data at the global sample rate when something of interest occurs and avoids recording mass quantities of irrelevant data. The event capture mode creates individual data files for each event occurrence that are associated with a single event type. Multiple sensors can be used in an "and/or" configuration to trigger an event data collection.

- Event capturing is not currently implemented.

BDI
740 S PIERCE AVE, SUITE 15
LOUISVILLE, CO 80027
303.494.3230
WWW.BDITEST.COM

ISSUE

CLIENT

ISL
259 Robin Crescent
Saskatoon, SK S7L 6MB

PROJECT NAME

ISL ENGINEERING AND LAND SERVICES
DIEFENBAKER BRIDGE
STRUCTURAL HEALTH MONITORING SYSTEM

Drawn By:	KNR
Checked By:	JDS
Date:	2/16/18
Client No.:	
BDI No.:	170906-SK
SCALE:	NTS

SYSTEM OPERATION
SHEET 4
SHM-13

APPENDIX B - RAINFLOW DATA

The rainflow data from the bottom strain gauges at Cross Section B are presented in this Appendix. This data was used to characterize the fatigue damage across the structure, and to refine the fatigue life evaluation.

Table B.1 - Rainflow data for February 14, 2018

Stress Range Bin (MPa)	Number of Cycles			
	Girder 1	Girder 2	Girder 3	Girder 4
5	653.5	613	599.5	562.5
10	94.5	66.5	95	199
15	25	19	31	48
20	9	5	9	12
25	11	0.5	0.5	23
30	0.5	0.5	0.5	4

Table B.2 – Rainflow data for February 15, 2018

Stress Range Bin (MPa)	Number of Cycles			
	Girder 1	Girder 2	Girder 3	Girder 4
5	740	528	559	535.5
10	115	51.5	63.5	120
15	20	17	38	29
20	4	2	3.5	17
25	8.5	0.5	0.5	26.5
30	2.5	0.5	0.5	1

Table B.3 – Rainflow data for February 16, 2018

Stress Range Bin (MPa)	Number of Cycles			
	Girder 1	Girder 2	Girder 3	Girder 4
5	620.5	537	612.5	603.5
10	92.5	66.5	56	105
15	20	19	32	36
20	8.5	0.5	7.5	13
25	12	0.5	1.5	17.5
30	0.5	0	0	3

Table B.4 – Rainflow data for February 17, 2018

Stress Range Bin (MPa)	Number of Cycles			
	Girder 1	Girder 2	Girder 3	Girder 4
5	231	180	197.5	240
10	36	16.5	25	28.5
15	9	5.5	10	19
20	1	0	4.5	3
25	4.5	0	0.5	8.5
30	0	0	0	1

Table B.5 – Rainflow data for February 18, 2019

Stress Range Bin (MPa)	Number of Cycles			
	Girder 1	Girder 2	Girder 3	Girder 4
5	225	133	146	148.5
10	21.5	20	18.5	23.5
15	11.5	2	8.5	15
20	4	0.5	5.5	2
25	1	0	1	8.5
30	0	0	0	1.5

Table B.6 – Rainflow data for February 19, 2018

Stress Range Bin (MPa)	Number of Cycles			
	Girder 1	Girder 2	Girder 3	Girder 4
5	355	180.5	171	181
10	40	21.5	26	36
15	12	1.5	16.5	14
20	1.5	0	3	5.5
25	0.5	1	0.5	13
30	0.5	0	0	1

Table B.7 – Rainflow data for February 20, 2018

Stress Range Bin (MPa)	Number of Cycles			
	Girder 1	Girder 2	Girder 3	Girder 4
5	549.5	450.5	494.5	468
10	101.5	54.5	55.5	124.5
15	16	14	30	31.5
20	6	1.5	6	14
25	8.5	0.5	1	15
30	1.5	0	0	1

Table B.8 – Rainflow data for February 22, 2018

Stress Range Bin (MPa)	Number of Cycles			
	Girder 1	Girder 2	Girder 3	Girder 4
5	254	237.5	262.5	242.5
10	43	30	32	42
15	10.5	10	12	15
20	7.5	3	4	8
25	3.5	0.5	0	10
30	0.5	0.5	0	1.5

Table B.9 – Rainflow data for February 23, 2018

Stress Range Bin (MPa)	Number of Cycles			
	Girder 1	Girder 2	Girder 3	Girder 4
5	622.5	509	565	576
10	100	62	75.5	115.5
15	29	21.5	20	39.5
20	13.5	3.5	6.5	11
25	11	0.5	1.5	15
30	1.5	0	0.5	2.5

Table B.10 – Rainflow data for February 24, 2018

Stress Range Bin (MPa)	Number of Cycles			
	Girder 1	Girder 2	Girder 3	Girder 4
5	266.5	201.5	212.5	223.5
10	42.5	22	22.5	27
15	14.5	4.5	11	14.5
20	2.5	0.5	5.5	7.5
25	2	0	0.5	8.5
30	0	0	0	2

Table B.11 – Rainflow data for February 25, 2018

Stress Range Bin (MPa)	Number of Cycles			
	Girder 1	Girder 2	Girder 3	Girder 4
5	231	160.5	163	173.5
10	34	18	19.5	25
15	13	2.5	6.5	12.5
20	0	0.5	3.5	5
25	0	0	2	6.5
30	1	0	0.5	1

Table B.12 – Rainflow data for February 26, 2018

Stress Range Bin (MPa)	Number of Cycles			
	Girder 1	Girder 2	Girder 3	Girder 4
5	727	615	639.5	6686.5
10	83.5	64.5	60	139
15	20.5	19.5	31	30
20	8	2	8	17.5
25	11	0	2	18
30	4	0	0.5	2.5

Table B.13 – Rainflow data for February 27, 2018

Stress Range Bin (MPa)	Number of Cycles			
	Girder 1	Girder 2	Girder 3	Girder 4
5	721	624.5	682	692
10	111	70.5	72	154.5
15	28	32.5	40.5	41.5
20	9	4	5	20.5
25	20	0.5	4	25
30	1.5	0	0.5	1.5

Table B.14 – Rainflow data for February 28, 2018

Stress Range Bin (MPa)	Number of Cycles			
	Girder 1	Girder 2	Girder 3	Girder 4
5	762.5	702.5	723.5	645
10	107.5	68	89.5	181
15	20.5	26.5	39	57
20	8	2	14.5	21
25	15	0	0.5	27
30	3	0.5	0	2

Table B.15 – Rainflow data for March 1, 2018

Stress Range Bin (MPa)	Number of Cycles			
	Girder 1	Girder 2	Girder 3	Girder 4
5	729	677	718.5	667.5
10	130	82.5	83.5	138.5
15	33	36.5	38	48.5
20	9	2.5	20.5	27
25	28.5	0.5	3.5	30.5
30	2.5	0.5	0.5	2.5

Table B.16 – Rainflow data for March 2, 2018

Stress Range Bin (MPa)	Number of Cycles			
	Girder 1	Girder 2	Girder 3	Girder 4
5	598.5	509	603.5	616.5
10	93	56	65	104
15	19.5	27	28.5	30
20	4.5	3.5	4	19.5
25	17	1	1.5	12
30	2	0.5	0	1

Table B.17 – Rainflow data for March 3, 2018

Stress Range Bin (MPa)	Number of Cycles			
	Girder 1	Girder 2	Girder 3	Girder 4
5	225	186	217	234.5
10	42	24.5	27	31.5
15	10.5	3.5	10	18.5
20	0.5	0.5	3.5	5
25	0	0	0.5	4
30	0	0	0	1

Table B.18 – Rainflow data for March 4, 2018

Stress Range Bin (MPa)	Number of Cycles			
	Girder 1	Girder 2	Girder 3	Girder 4
5	323	27	232	248.5
10	57	2	41	56.5
15	6.5	0	7.5	22.5
20	1	0	7	6.5
25	0.5	0	4	5.5
30	1	0	0	2.5

Table B.19 – Rainflow data for March 5, 2018

Stress Range Bin (MPa)	Number of Cycles			
	Girder 1	Girder 2	Girder 3	Girder 4
5	608.5	560.5	614.5	589
10	80	68.5	70.5	147
15	18.5	11.5	28.5	35
20	3.5	3	8.5	9
25	8.5	0.5	0	16.5
30	0.5	0	0	0.5

Table B.20 – Rainflow data for March 6, 2018

Stress Range Bin (MPa)	Number of Cycles			
	Girder 1	Girder 2	Girder 3	Girder 4
5	923	819	931.5	806.5
10	102	76	94	299.5
15	20	15.5	29.5	36
20	4	4	12.5	17
25	8	0.5	0.5	19.5
30	1	0	0	1

Table B.21 – Rainflow data for March 7, 2018

Stress Range Bin (MPa)	Number of Cycles			
	Girder 1	Girder 2	Girder 3	Girder 4
5	1062	1017.5	1085.5	892.5
10	126.5	92	113	401
15	32	21.5	34	38
20	7	4	21	18.5
25	8.5	0.5	0.5	28.5
30	0	0.5	0.5	2

Table B.22 – Rainflow data for March 8, 2018

Stress Range Bin (MPa)	Number of Cycles			
	Girder 1	Girder 2	Girder 3	Girder 4
5	919.5	801.5	876	816
10	129.5	94.5	99	257.5
15	27.5	38	41	45
20	15.5	1.5	12.5	14.5
25	23	1.5	1.5	32
30	1	0	0.5	4

Table B.23 – Rainflow data for March 9, 2018

Stress Range Bin (MPa)	Number of Cycles			
	Girder 1	Girder 2	Girder 3	Girder 4
5	900	784.5	868.5	821.5
10	125.5	75	86.5	207.5
15	23.5	20	29.5	45
20	7	2	3	18.5
25	11	0.5	2	17.5
30	0.5	0	0	1.5

Table B.24 – Rainflow data for March 13, 2018

Stress Range Bin (MPa)	Number of Cycles			
	Girder 1	Girder 2	Girder 3	Girder 4
5	72	68	68.5	75.5
10	16	3	11	11
15	0.5	0	4.5	11
20	0	0	4	6
25	0	0	1	2.5
30	0.5	0	0	0.5

Table B.25 – Rainflow data for March 14, 2018

Stress Range Bin (MPa)	Number of Cycles			
	Girder 1	Girder 2	Girder 3	Girder 4
5	825	707	808.5	748.5
10	127.5	79.5	74.5	211.5
15	28.5	38	42	40
20	7.5	3.5	16	28.5
25	14.5	1	3.5	19
30	6.5	0.5	0	9

Table B.26 – Rainflow data for March 15, 2018

Stress Range Bin (MPa)	Number of Cycles			
	Girder 1	Girder 2	Girder 3	Girder 4
5	723.5	599	723	722
10	109.5	74	81	180.5
15	31	34.5	30.5	37.5
20	6	2	9	16
25	19	0.5	1.5	19.5
30	7	0	0.5	3.5

Table B.27 – Rainflow data for March 17, 2018

Stress Range Bin (MPa)	Number of Cycles			
	Girder 1	Girder 2	Girder 3	Girder 4
5	237	180.5	218.5	264.5
10	33	13.5	15.5	24
15	6.5	36	7	11.5
20	1.5	1	8.5	6
25	1	0	3	5
30	0	0	0	3.5

Table B.28 – Rainflow data for March 18, 2018

Stress Range Bin (MPa)	Number of Cycles			
	Girder 1	Girder 2	Girder 3	Girder 4
5	227.5	171.5	181.5	216.5
10	30	22	21	32.5
15	16.5	3.5	7	11.5
20	2.5	0.5	5.5	8
25	0	0	1	3.5
30	0	0	1	3

Table B.29 – Rainflow data for March 19, 2018

Stress Range Bin (MPa)	Number of Cycles			
	Girder 1	Girder 2	Girder 3	Girder 4
5	52.5	48	64.5	69.5
10	11	10.5	5.5	11
15	6.5	0.5	2.5	3.5
20	1.5	1	0	0.5
25	0	0	0	2
30	0	0	0	0

Table B.30 – Rainflow data for March 20, 2019

Stress Range Bin (MPa)	Number of Cycles			
	Girder 1	Girder 2	Girder 3	Girder 4
5	662	639	669.5	678
10	117	61	82	153
15	24	29	38	43.5
20	10	2	16	18.5
25	16	0.5	2	21
30	2.5	0	0	9.5

Table B.31 – Rainflow data for March 21, 2018

Stress Range Bin (MPa)	Number of Cycles			
	Girder 1	Girder 2	Girder 3	Girder 4
5	717.5	691.5	692	692
10	128	79	77.5	125.5
15	26	29	44.5	51.5
20	11	1.5	39	25
25	10	1.5	4.5	32
30	7	0.5	0.5	23

Table B.32 – Rainflow data for March 22, 2018

Stress Range Bin (MPa)	Number of Cycles			
	Girder 1	Girder 2	Girder 3	Girder 4
5	69.5	73.5	75	95.5
10	17.5	1.5	10	8.5
15	1	2.5	4	3
20	2.5	0.5	1.5	5.5
25	0.5	0.5	1	1.5
30	0	0	0	1

Table B.33 – Rainflow data for March 23, 2018

Stress Range Bin (MPa)	Number of Cycles			
	Girder 1	Girder 2	Girder 3	Girder 4
5	579.5	534.5	597	628
10	85.5	69	60.5	105
15	20.5	18.5	29	36.5
20	6	1.5	10.5	17.5
25	10	1	1	15
30	2	0	0	4

Table B.34 – Rainflow data for March 24, 2018

Stress Range Bin (MPa)	Number of Cycles			
	Girder 1	Girder 2	Girder 3	Girder 4
5	276	220.5	271.5	290.5
10	45	22	28	43.5
15	11	3.5	10	13
20	2	0	9	5
25	0	1	0.5	7
30	0	0	0	3.5

Table B.35 – Rainflow data for March 25, 2018

Stress Range Bin (MPa)	Number of Cycles			
	Girder 1	Girder 2	Girder 3	Girder 4
5	311.5	281	276.5	299
10	43	27	29.5	67
15	11.5	3.5	5.5	12
20	0	0	7.5	5
25	0	0	1.5	6
30	0.5	0	0	2

Table B.36 – Rainflow data for March 26, 2018

Stress Range Bin (MPa)	Number of Cycles			
	Girder 1	Girder 2	Girder 3	Girder 4
5	843.5	787	807	795.5
10	122.5	65	82	208
15	20	14.5	36	44.5
20	6.5	1	18	12
25	5.5	1	4.5	22.5
30	1	0	0	10.5

Table B.37 – Rainflow data for March 27, 2018

Stress Range Bin (MPa)	Number of Cycles			
	Girder 1	Girder 2	Girder 3	Girder 4
5	736.5	711	720.5	736
10	120.5	79	84	189.5
15	21	18.5	39.5	49
20	5.5	2	19.5	14
25	9.5	0.5	1.5	31.5
30	0.5	0	0	7.5

Table B.38 – Rainflow data for March 28, 2018

Stress Range Bin (MPa)	Number of Cycles			
	Girder 1	Girder 2	Girder 3	Girder 4
5	792.5	728	741.5	780
10	132.5	84	90	185
15	32	28.5	39.5	44
20	8.5	4.5	15.5	13
25	15	0.5	4	28
30	2	0	0.5	8.5

Table B.39 – Rainflow data for March 30, 2018

Stress Range Bin (MPa)	Number of Cycles			
	Girder 1	Girder 2	Girder 3	Girder 4
5	412	184.5	224.5	274.5
10	41	26	22	38.5
15	8	4	10.5	11.5
20	2.5	0	4	6
25	0.5	0.5	0.5	6
30	0	0	0	1.5

Table B.40 – Rainflow data for March 31, 2018

Stress Range Bin (MPa)	Number of Cycles			
	Girder 1	Girder 2	Girder 3	Girder 4
5	243	178.5	168	205.5
10	34.5	14	8.5	18
15	8.5	1.5	5	3
20	1.5	0	4	3
25	1	0.5	1	4.5
30	0.5	0	0	1.5

Table B.41 – Rainflow data for April 1, 2018

Stress Range Bin (MPa)	Number of Cycles			
	Girder 1	Girder 2	Girder 3	Girder 4
5	207	139.5	152	171
10	13.5	12	11.5	19
15	7	2	9.5	8
20	1.5	0	4.5	8
25	1	0.5	0	3.5
30	0	0	0.5	2.5

Table B.42 – Rainflow data for April 2, 2018

Stress Range Bin (MPa)	Number of Cycles			
	Girder 1	Girder 2	Girder 3	Girder 4
5	489.5	440.5	491.5	473
10	84	58	47	103.5
15	22.5	23	30.5	31
20	6	4.5	10.5	9.5
25	10.5	0.5	1.5	25
30	3	0.5	0	2.5

Table B.43 – Rainflow data for April 3, 2018

Stress Range Bin (MPa)	Number of Cycles			
	Girder 1	Girder 2	Girder 3	Girder 4
5	606.5	539.5	584.5	593.5
10	87	77.5	72.5	142.5
15	33	29.5	28	31.5
20	10	1	19.5	12
25	12	0.5	1.5	19.5
30	0.5	0.5	0	7.5

Table B.44 – Rainflow data for April 4, 2018

Stress Range Bin (MPa)	Number of Cycles			
	Girder 1	Girder 2	Girder 3	Girder 4
5	573	525.5	534.5	557
10	83.5	56.5	61.5	123.5
15	16	18.5	25.5	27.5
20	10.5	0.5	20.5	18
25	9.5	0.5	2	19.5
30	0.5	0	0.5	9.5

Table B.45 – Rainflow data for April 5, 2018

Stress Range Bin (MPa)	Number of Cycles			
	Girder 1	Girder 2	Girder 3	Girder 4
5	301.5	270.5	305	287.5
10	39.5	35	32.5	44
15	18	12	14	13.5
20	2	0	7	10
25	6	1	1	4
30	1	0	0	6.5

Table B.46 – Rainflow data for April 6, 2018

Stress Range Bin (MPa)	Number of Cycles			
	Girder 1	Girder 2	Girder 3	Girder 4
5	224.5	198.5	266.5	265.5
10	26.5	22.5	16.5	36
15	12.5	3	6.5	11
20	0	1.5	2	3
25	1.5	0.5	1	3
30	0	0	0	1

Table B.47 – Rainflow data for April 7, 2018

Stress Range Bin (MPa)	Number of Cycles			
	Girder 1	Girder 2	Girder 3	Girder 4
5	234	193	236	260
10	28	20	10	28.5
15	7	5	8	5.5
20	2.5	0	8.5	3.5
25	3	0	0	5.5
30	0.5	0.5	0.5	5.5

Table B.48 – Rainflow data for April 8, 2018

Stress Range Bin (MPa)	Number of Cycles			
	Girder 1	Girder 2	Girder 3	Girder 4
5	188.5	143.5	175.5	224
10	17	18.5	15	17
15	11.5	6.5	2	11
20	2.5	0	3.5	2
25	2	0.5	1	2.5
30	1	0	0	1.5

Table B.49 – Rainflow data for April 9, 2018

Stress Range Bin (MPa)	Number of Cycles			
	Girder 1	Girder 2	Girder 3	Girder 4
5	228.5	190.5	257	299
10	18	19.5	15	25
15	7	4.5	7	7.5
20	5.5	1.5	7	3
25	2	0	0.5	6
30	0	0	0	4

Table B.50 – Rainflow data for April 10, 2018

Stress Range Bin (MPa)	Number of Cycles			
	Girder 1	Girder 2	Girder 3	Girder 4
5	628	630	696.5	691.5
10	101	85	71.5	139
15	32	26.5	33.5	44
20	7.5	3.5	15.5	22
25	10	2	3.5	13
30	6	0.5	0.5	6

Table B.51 – Rainflow data for April 11, 2018

Stress Range Bin (MPa)	Number of Cycles			
	Girder 1	Girder 2	Girder 3	Girder 4
5	676	629	662.5	688.5
10	108	73.5	68	155.5
15	25	29.5	39.5	32
20	10.5	2.5	13	14
25	13	1.5	1	12
30	3.5	0.5	0	7

Table B.52 – Rainflow data for April 12, 2018

Stress Range Bin (MPa)	Number of Cycles			
	Girder 1	Girder 2	Girder 3	Girder 4
5	658	615.5	664.5	670.5
10	98.5	66	78	146
15	20.5	18.5	31	35.5
20	7.5	2.5	12.5	15.5
25	10.5	1.5	1	14
30	0.5	0	2	8

Table B.53 – Rainflow data for April 13, 2018

Stress Range Bin (MPa)	Number of Cycles			
	Girder 1	Girder 2	Girder 3	Girder 4
5	604	522.5	629	678.5
10	78	74	49	110.5
15	22.5	15.5	24	25.5
20	10.5	1	10	10
25	7	0	0.5	14
30	1	0	0	5

Table B.54 – Rainflow data for April 14, 2018

Stress Range Bin (MPa)	Number of Cycles			
	Girder 1	Girder 2	Girder 3	Girder 4
5	229	170.5	258	307
10	28	18.5	16.5	27
15	8	4	11.5	13
20	2.5	1.5	3.5	5.5
25	2	1	0.5	7
30	1	0	0.5	1

Table B.55 – Rainflow data for April 15, 2018

Stress Range Bin (MPa)	Number of Cycles			
	Girder 1	Girder 2	Girder 3	Girder 4
5	201.5	166.5	180.5	244
10	26.5	14	8	12.5
15	4	2.5	13.5	7
20	1	1	4	10
25	0	0	0	2.5
30	1	0	0	2.5

Table B.56 – Rainflow data for April 16, 2018

Stress Range Bin (MPa)	Number of Cycles			
	Girder 1	Girder 2	Girder 3	Girder 4
5	155	118	79.5	214.5
10	14.5	13	3.5	22
15	7.5	5.5	0.5	6
20	3	1.5	0	1
25	0.5	0.5	0	4
30	1	0	0	1

Table B.57 – Rainflow data for April 17, 2018

Stress Range Bin (MPa)	Number of Cycles			
	Girder 1	Girder 2	Girder 3	Girder 4
5	641	576.5	647.5	679.5
10	105	86.5	71.5	143.5
15	37	20.5	24	33
20	8.5	2	12.5	8
25	3	0.5	1	12.5
30	3.5	0	0	6.5

Table B.58 – Rainflow data for April 18, 2018

Stress Range Bin (MPa)	Number of Cycles			
	Girder 1	Girder 2	Girder 3	Girder 4
5	664	565.5	672.5	691
10	88.5	81	68.5	142.5
15	28	20	27	28.5
20	7	2.5	6.5	11
25	3	0.5	1	7
30	4	0.5	0	4

Table B.59 – Rainflow data for April 19, 2018

Stress Range Bin (MPa)	Number of Cycles			
	Girder 1	Girder 2	Girder 3	Girder 4
5	770.5	717.5	710	796.5
10	122	83.5	85	147
15	34	16	47	35
20	8.5	1.5	14	16.5
25	3	1.5	0.5	15.5
30	3	0	0	7

Table B.60 – Rainflow data for April 20, 2018

Stress Range Bin (MPa)	Number of Cycles			
	Girder 1	Girder 2	Girder 3	Girder 4
5	729.5	649	686.5	728
10	85	65.5	60.5	122
15	20.5	17	33	28.5
20	7	1.5	14.5	8
25	4	2	1	10
30	4	0	0	5

Table B.61 – Rainflow data for April 21, 2018

Stress Range Bin (MPa)	Number of Cycles			
	Girder 1	Girder 2	Girder 3	Girder 4
5	303	234	287.5	341
10	37	24	21	31
15	7	3.5	9.5	7.5
20	3.5	1.5	4.5	2
25	1.5	0	0.5	3
30	2	0	0	1.5

Table B.62 – Rainflow data for April 22, 2018

Stress Range Bin (MPa)	Number of Cycles			
	Girder 1	Girder 2	Girder 3	Girder 4
5	236.5	151	178	236
10	16	11	9	24.5
15	8	3.5	5.5	5
20	0.5	0	1	2.5
25	1	0	0	1.5
30	0	0	0	0

Table B.63 – Rainflow data for April 23, 2018

Stress Range Bin (MPa)	Number of Cycles			
	Girder 1	Girder 2	Girder 3	Girder 4
5	758.5	678	664.5	214.5
10	95	71	78.5	22
15	22.5	10	30.5	6
20	6.5	2	16.5	1
25	2.5	1.5	1	4
30	0	0	0	1

Table B.64 – Rainflow data for April 24, 2018

Stress Range Bin (MPa)	Number of Cycles			
	Girder 1	Girder 2	Girder 3	Girder 4
5	767	673	721	757.5
10	112	78	82.5	132.5
15	20.5	18	31.5	43.5
20	9	2.5	14.5	10
25	3.5	0	0.5	14.5
30	2.5	0	1	7.5

Table B.65 – Rainflow data for April 25, 2018

Stress Range Bin (MPa)	Number of Cycles			
	Girder 1	Girder 2	Girder 3	Girder 4
5	86.5	72.5	103.5	111.5
10	13.5	10.5	5	7
15	8	1.5	3	3.5
20	1.5	0.5	0	4
25	0.5	0	1.5	0.5
30	0	0	0	0

Table B.66 – Rainflow data for April 26, 2018

Stress Range Bin (MPa)	Number of Cycles			
	Girder 1	Girder 2	Girder 3	Girder 4
5	840.5	674	723.5	758.5
10	93.5	81	79.5	130.5
15	29	13.5	27.5	37
20	8.5	3	6	18
25	3	3	2	7.5
30	1	0	0.5	1.5

Table B.67 – Rainflow data for April 27, 2018

Stress Range Bin (MPa)	Number of Cycles			
	Girder 1	Girder 2	Girder 3	Girder 4
5	840.5	680	790.5	842
10	89.5	84	68	121.5
15	26	23.5	24.5	39.5
20	7	2.5	8	19
25	6.5	1	2	5
30	0	0	1.5	3.5

Table B.68 – Rainflow data for April 28, 2018

Stress Range Bin (MPa)	Number of Cycles			
	Girder 1	Girder 2	Girder 3	Girder 4
5	365	273.5	376	398
10	32.5	18.5	15	19.5
15	5	4.5	11	13
20	2	1	2	4.5
25	0.5	0.5	1.5	1.5
30	1	0	0.5	1.5

Table B.69 – Rainflow data for April 29, 2018

Stress Range Bin (MPa)	Number of Cycles			
	Girder 1	Girder 2	Girder 3	Girder 4
5	266	187.5	227.5	261
10	13.5	15	11	19
15	9.5	2	5	5.5
20	4	1.5	5	6
25	1	1	0.5	2
30	1	0	0	3

Table B.70 – Rainflow data for April 30, 2018

Stress Range Bin (MPa)	Number of Cycles			
	Girder 1	Girder 2	Girder 3	Girder 4
5	769	691.5	762.5	805
10	93.5	79.5	82	149
15	23	22.5	32	36
20	8.5	4.5	12.5	18
25	10.5	1	1	7.5
30	5	0	0	8.5

Table B.71 – Rainflow data for May 1, 2018

Stress Range Bin (MPa)	Number of Cycles			
	Girder 1	Girder 2	Girder 3	Girder 4
5	864	779	821.5	875
10	121	70.5	89	153
15	24	17.5	47	46
20	8	8	14	25
25	3.5	3	0.5	14
30	4	0	1	8.5

Table B.72 – Rainflow data for May 2, 2018

Stress Range Bin (MPa)	Number of Cycles			
	Girder 1	Girder 2	Girder 3	Girder 4
5	877.5	768	816	855.5
10	110	82	93.5	152
15	28	17.5	50.5	42
20	9.5	5.5	7.5	20.5
25	5	5.5	1.5	12.5
30	7	0	0.5	5.5

Table B.73 – Rainflow data for May 3, 2018

Stress Range Bin (MPa)	Number of Cycles			
	Girder 1	Girder 2	Girder 3	Girder 4
5	919.5	815	786	809.5
10	109.5	82	101.5	154
15	25	18	53.5	52.5
20	7	2	9	14
25	4.5	2.5	0.5	16
30	3	0	1	3

Table B.74 – Rainflow data for May 4, 2018

Stress Range Bin (MPa)	Number of Cycles			
	Girder 1	Girder 2	Girder 3	Girder 4
5	837	727.5	846	836.5
10	93.5	72	74.5	128.5
15	19.5	18	27	37.5
20	7.5	2.5	10.5	15.5
25	4	1	1	10.5
30	3	0	0.5	4.5

Table B.75 – Rainflow data for May 5, 2018

Stress Range Bin (MPa)	Number of Cycles			
	Girder 1	Girder 2	Girder 3	Girder 4
5	410.5	322.5	385.5	391
10	23	15	15	30
15	7.5	4.5	6	7.5
20	2	2	6.5	4.5
25	0.5	0.5	1.5	2
30	2	0	0.5	5

Table B.76 – Rainflow data for May 6, 2018

Stress Range Bin (MPa)	Number of Cycles			
	Girder 1	Girder 2	Girder 3	Girder 4
5	329.5	236	288	281.5
10	18	17	16.5	22
15	10.5	1	4.5	11.5
20	3	1	2	3.5
25	0	1.5	0.5	1
30	0	0	0	0

Table B.77 – Rainflow data for May 7, 2018

Stress Range Bin (MPa)	Number of Cycles			
	Girder 1	Girder 2	Girder 3	Girder 4
5	946.5	813	875.5	832.5
10	121.5	109.5	93	143
15	38.5	24	45.5	38
20	13.5	3.5	20.5	17.5
25	4	2.5	1.5	16.5
30	2	0.5	1.5	8

Table B.78 – Rainflow data for May 8, 2018

Stress Range Bin (MPa)	Number of Cycles			
	Girder 1	Girder 2	Girder 3	Girder 4
5	877	777	805	811
10	112.5	87.5	83	139
15	24	18	55.5	44
20	5	4	14.5	32.5
25	8	1.5	1.5	17.5
30	3	0	0.5	4

Table B.79 – Rainflow data for May 9, 2018

Stress Range Bin (MPa)	Number of Cycles			
	Girder 1	Girder 2	Girder 3	Girder 4
5	863	740.5	802.5	873
10	113.5	101.5	93	156
15	32.5	20.5	43.5	44
20	15	5	18.5	25.5
25	6.5	0.5	2	25
30	2	0	0.5	9.5

Table B.80 – Rainflow data for May 10, 2018

Stress Range Bin (MPa)	Number of Cycles			
	Girder 1	Girder 2	Girder 3	Girder 4
5	911.5	798	846.5	916.5
10	130.5	98.5	96	145.5
15	34	12.5	53.5	49.5
20	3	3	21.5	27.5
25	5	0.5	2	23
30	1.5	0	0.5	16.5

Table B.81 – Rainflow data for May 11, 2018

Stress Range Bin (MPa)	Number of Cycles			
	Girder 1	Girder 2	Girder 3	Girder 4
5	996	841.5	900	1041.5
10	120	94.5	102	151.5
15	32.5	19.5	58.5	54
20	7.5	7.5	24	29
25	8	1	2.5	28.5
30	2.5	0	0	12.5

Table B.82 – Rainflow data for May 12, 2018

Stress Range Bin (MPa)	Number of Cycles			
	Girder 1	Girder 2	Girder 3	Girder 4
5	551	424.5	470	488.5
10	50	30.5	30.5	50
15	9	10.5	25.5	18.5
20	4.5	1	24.5	15
25	0	0.5	0.5	19.5
30	3	0	1.5	10

Table B.83 – Rainflow data for May 13, 2018

Stress Range Bin (MPa)	Number of Cycles			
	Girder 1	Girder 2	Girder 3	Girder 4
5	381.5	305	306	325
10	31.5	28	31.5	22.5
15	12.5	3.5	18.5	21
20	4	0.5	13.5	20.5
25	0.5	0.5	2	11.5
30	1	0	1	5

Table B.84 – Rainflow data for May 14, 2018

Stress Range Bin (MPa)	Number of Cycles			
	Girder 1	Girder 2	Girder 3	Girder 4
5	998.5	896	928	926
10	135	91.5	115	146
15	36.5	31	48.5	59
20	10.5	5	30	34
25	9.5	5.5	2.5	27.5
30	7.5	0	1.5	10.5

Table B.85 – Rainflow data for May 15, 2018

Stress Range Bin (MPa)	Number of Cycles			
	Girder 1	Girder 2	Girder 3	Girder 4
5	995.5	874.5	938	884.5
10	134.5	110	122.5	179
15	36	26	64.5	60
20	14	5.5	34.5	35
25	6	2	1.5	32
30	2.5	0.5	1	8

Table B.86 – Rainflow data for May 16, 2018

Stress Range Bin (MPa)	Number of Cycles			
	Girder 1	Girder 2	Girder 3	Girder 4
5	1020.5	943.5	938	970.5
10	138	109	133	161
15	34.5	26	69	71.5
20	12.5	4.5	27.5	40
25	7	2	2.5	30.5
30	2	0	0.5	18

Table B.87 – Rainflow data for May 17, 2018

Stress Range Bin (MPa)	Number of Cycles			
	Girder 1	Girder 2	Girder 3	Girder 4
5	966.5	892.5	970.5	1052.5
10	109.5	92.5	122	144
15	25	31.5	53	71
20	7	5	32.5	38
25	4.5	1.5	1	30
30	3	0	1	16.5

Table B.88 – Rainflow data for May 18, 2018

Stress Range Bin (MPa)	Number of Cycles			
	Girder 1	Girder 2	Girder 3	Girder 4
5	914.5	826	1249	1321.5
10	129.5	88	104	142.5
15	34	22	53	66
20	7.5	4.5	34	31
25	4	1	5	26.5
30	4	0	1.5	17.5

Table B.89 – Rainflow data for May 19, 2018

Stress Range Bin (MPa)	Number of Cycles			
	Girder 1	Girder 2	Girder 3	Girder 4
5	433.5	384	551.5	553.5
10	52	29.5	24	41
15	10.5	3.5	25	24
20	5.5	1	27.5	18
25	0	2	2.5	18
30	0	0	1.5	9

Table B.90 – Rainflow data for May 20, 2018

Stress Range Bin (MPa)	Number of Cycles			
	Girder 1	Girder 2	Girder 3	Girder 4
5	376	313.5	326.5	378
10	49	23.5	21	22.5
15	7	11.5	23.5	21
20	4.5	1	20.5	20.5
25	2	0.5	1.5	11.5
30	0	0	0.5	5

Table B.91 – Rainflow data for May 21, 2018

Stress Range Bin (MPa)	Number of Cycles			
	Girder 1	Girder 2	Girder 3	Girder 4
5	892.5	700.5	421	435.5
10	73	39	40	43
15	8.5	10	31.5	30.5.
20	6.5	3	26	20
25	1	0	1	19.5
30	1.5	0	0.5	10.5

Table B.92 – Rainflow data for May 22, 2018

Stress Range Bin (MPa)	Number of Cycles			
	Girder 1	Girder 2	Girder 3	Girder 4
5	1120	918	987	984
10	134.5	105	116	162.5
15	34.5	39.5	59.5	58.5
20	11.5	10	33.5	27.5
25	7.5	9.5	1	36
30	2	0.5	0.5	9

Table B.93 – Rainflow data for May 23, 2018

Stress Range Bin (MPa)	Number of Cycles			
	Girder 1	Girder 2	Girder 3	Girder 4
5	987.5	900	972.5	937
10	165	115	112	146.5
15	31.5	71.5	52	52.5
20	15	12.5	30	38
25	5.5	9	1.5	20.5
30	8.5	0.5	2	13.5

Table B.94 – Rainflow data for May 24, 2018

Stress Range Bin (MPa)	Number of Cycles			
	Girder 1	Girder 2	Girder 3	Girder 4
5	1002	899	946.5	993
10	150	118	124	157
15	33.5	60	48.5	62
20	11	17	29	29
25	11	4	2	22
30	5	0.5	0	8.5

Table B.95 – Rainflow data for May 25, 2018

Stress Range Bin (MPa)	Number of Cycles			
	Girder 1	Girder 2	Girder 3	Girder 4
5	1003.5	868.5	1098	1100
10	151	128.5	123	164.5
15	50	78	38.5	56
20	15.5	27	21	26
25	7.5	3	3	21.5
30	10.5	0	0.5	5

Table B.96 – Rainflow data for May 26, 2018

Stress Range Bin (MPa)	Number of Cycles			
	Girder 1	Girder 2	Girder 3	Girder 4
5	434	355.5	432	454
10	35	30.5	25	48.5
15	8	24	22.5	17.5
20	12.5	1	11.5	10.5
25	9.5	3.5	0	11
30	1.5	0	0	1.5

Table B.97 – Rainflow data for May 27, 2018

Stress Range Bin (MPa)	Number of Cycles			
	Girder 1	Girder 2	Girder 3	Girder 4
5	396.5	316.5	254.5	355.5
10	20	14	20.5	24.5
15	4.5	3	12.5	15
20	0.5	0.5	3.5	11
25	0.5	0.5	1	4
30	0.5	0	0.5	1

Table B.98 – Rainflow data for May 28, 2018

Stress Range Bin (MPa)	Number of Cycles			
	Girder 1	Girder 2	Girder 3	Girder 4
5	1056	912.5	983.5	951.5
10	135	118.5	107	172
15	51	52.5	47.5	51
20	16	34.5	23.5	24.5
25	7.5	13	3.5	20
30	7	1	0	5.5

Table B.99 – Rainflow data for May 29, 2018

Stress Range Bin (MPa)	Number of Cycles			
	Girder 1	Girder 2	Girder 3	Girder 4
5	1025.5	921	1038	1038
10	140.5	116.5	123	123
15	69.5	64.5	60.5	60.5
20	13	48.5	17	17
25	4.5	7.5	0.5	0.5
30	5	0	0	10

Table B.100 – Rainflow data for May 30, 2018

Stress Range Bin (MPa)	Number of Cycles			
	Girder 1	Girder 2	Girder 3	Girder 4
5	1025	853.5	950	981
10	147	127.5	122.5	184
15	53	56.5	54.5	47
20	14..5	45.5	22.5	28
25	5	7.5	2	10
30	8.5	0.5	0	14

Table B.101 – Rainflow data for May 31, 2018

Stress Range Bin (MPa)	Number of Cycles			
	Girder 1	Girder 2	Girder 3	Girder 4
5	1033.5	849.5	986.5	1076
10	160	109.5	113.5	182.5
15	48.5	69.5	39	52
20	9	31	18	22
25	5	7	1	10.5
30	2.5	0	1.5	13

Table B.102 – Rainflow data for June 1, 2018

Stress Range Bin (MPa)	Number of Cycles			
	Girder 1	Girder 2	Girder 3	Girder 4
5	939	789.5	951.5	1074.5
10	102.5	75	75	143
15	36	46.5	33	29
20	9	25	14	27
25	2	6	0	10
30	4	0	0.5	8

Table B.103 – Rainflow data for June 2, 2018

Stress Range Bin (MPa)	Number of Cycles			
	Girder 1	Girder 2	Girder 3	Girder 4
5	377.5	306	304.5	386.5
10	30	18	10.5	27.5
15	5.5	2	7	3.5
20	0.5	0.5	7	6
25	2	2	0.5	3.5
30	0	0	0	4.5

Table B.104 – Rainflow data for June 3, 2018

Stress Range Bin (MPa)	Number of Cycles			
	Girder 1	Girder 2	Girder 3	Girder 4
5	437	282.5	262	347
10	16.5	18.5	13.5	18.5
15	4.5	3	5.5	9
20	1	1	3	4.5
25	0	0.5	0	2.5
30	0.5	0.5	0	1

Table B.105 – Rainflow data for June 4, 2018

Stress Range Bin (MPa)	Number of Cycles			
	Girder 1	Girder 2	Girder 3	Girder 4
5	956	825.5	889	1062.5
10	113.5	99	98	149
15	30	50.5	36.5	46
20	12	8.5	17.5	28.5
25	4	10	1	13.5
30	4	0.5	0.5	9

Table B.106 – Rainflow data for June 5, 2018

Stress Range Bin (MPa)	Number of Cycles			
	Girder 1	Girder 2	Girder 3	Girder 4
5	997.5	887	943.5	1039
10	103.5	97	131	160
15	29	41	46	72
20	14.5	10.5	31.5	29
25	4.5	6.5	0.5	20
30	6	0.5	0.5	24.5

Table B.107 – Rainflow data for June 6, 2018

Stress Range Bin (MPa)	Number of Cycles			
	Girder 1	Girder 2	Girder 3	Girder 4
5	915.5	803..5	851.5	941
10	81.5	91.5	57.5	128
15	19.5	20.5	38	50.5
20	9.5	7.5	30.5	26
25	4.5	4.5	2.5	24
30	2.5	1	0	11.5

Table B.108 – Rainflow data for June 7, 2018

Stress Range Bin (MPa)	Number of Cycles			
	Girder 1	Girder 2	Girder 3	Girder 4
5	1053	894.5	1062	1099
10	145	137	128.5	159.5
15	29	66	50.5	54
20	17.5	8.5	27	37.5
25	3	9.5	4	24.5
30	4	0.5	0.5	10

Table B.109 – Rainflow data for June 8, 2018

Stress Range Bin (MPa)	Number of Cycles			
	Girder 1	Girder 2	Girder 3	Girder 4
5	979	827	1090.5	1150
10	86	98.5	76	139.5
15	22.5	21	39.5	34.5
20	10	4	21	24
25	2.5	8	1.5	21
30	1.5	0.5	1	5

Table B.110 – Rainflow data for June 9, 2018

Stress Range Bin (MPa)	Number of Cycles			
	Girder 1	Girder 2	Girder 3	Girder 4
5	381	292	405.5	477.5
10	30	18.5	16.5	30
15	8	8.5	9	11.5
20	1.5	3.5	2.5	9.5
25	2.5	2	0.5	3.5
30	0.5	0	0.5	0.5

Table B.111 – Rainflow data for June 10, 2018

Stress Range Bin (MPa)	Number of Cycles			
	Girder 1	Girder 2	Girder 3	Girder 4
5	529.5	401	271	305
10	19.5	15	7.5	11.5
15	3.5	7	7.5	7.5
20	0.5	2	5	4
25	1.5	2	1	3.5
30	2.5	0.5	0.5	3.5

Table B.112 – Rainflow data for June 11, 2018

Stress Range Bin (MPa)	Number of Cycles			
	Girder 1	Girder 2	Girder 3	Girder 4
5	529.5	401	271	305
10	19.5	15	7.5	11.5
15	3.5	7	7.5	7.5
20	0.5	2	5	4
25	1.5	2	1	3.5
30	2.5	0.5	0.5	3.5

Table B.113 – Rainflow data for June 12, 2018

Stress Range Bin (MPa)	Number of Cycles			
	Girder 1	Girder 2	Girder 3	Girder 4
5	968	847.5	855.5	948
10	84.5	97	106	155.5
15	29	28.5	32	65
20	14	11.5	21	22.5
25	6	13	2	21.5
30	4	1	1.5	12.5

Table B.114 – Rainflow data for June 13, 2018

Stress Range Bin (MPa)	Number of Cycles			
	Girder 1	Girder 2	Girder 3	Girder 4
5	956.5	796.5	866.5	980.5
10	74.5	103.5	92	139.5
15	25	26.5	41.5.	55
20	17	10.5	21.5	20.5
25	5.5	20	1.5	21.5
30	5.5	0.5	0.5	5

APPENDIX C - CALIBRATION DATA

The calibration loading data from the top and bottom strain gauges on each girder at Cross Section B are presented in this Appendix. This data was used to characterize the lateral load distribution, dynamic load allowance, degree of composite action, and the symmetry of the northbound and southbound bridge responses. Positive strains on the graphs represent tension, and negative strain represents compression.

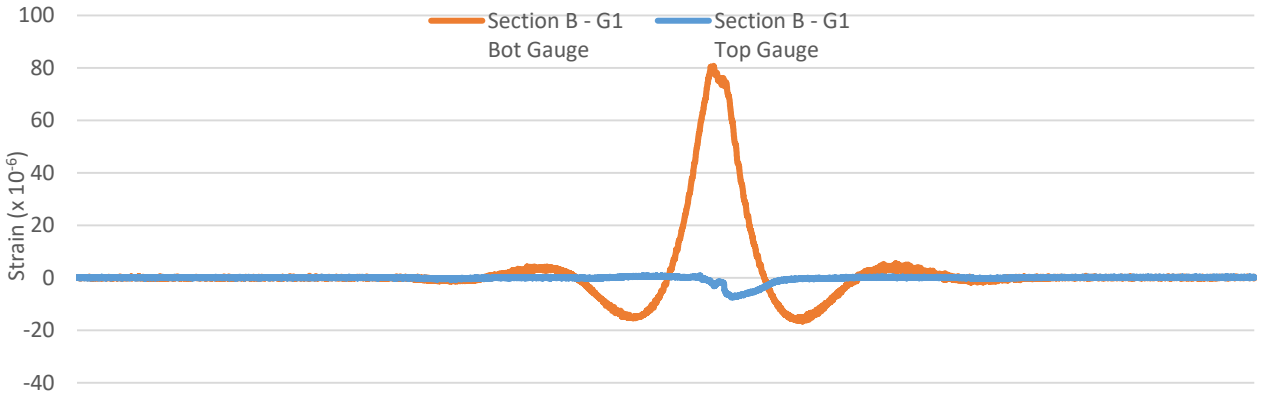

Figure C.1 - Girder 1 strain gauge response to the slow southbound barrier lane load test

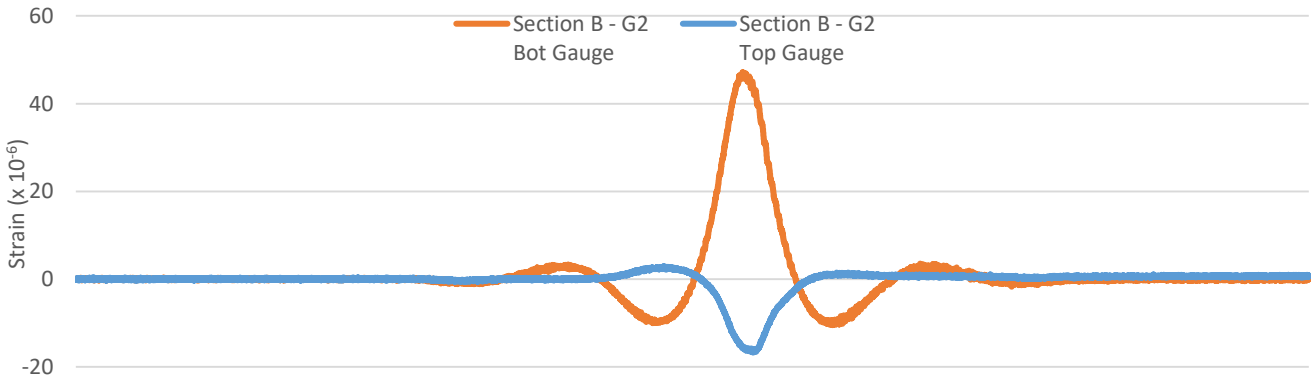

Figure C.2 - Girder 2 strain gauge response to slow southbound barrier lane load test

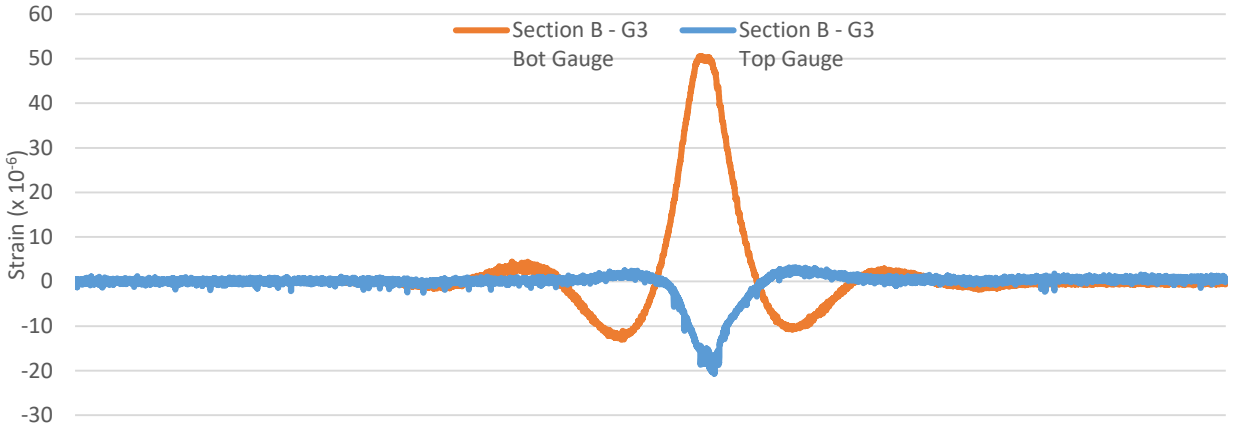

Figure C.3 - Girder 3 strain gauge response to slow northbound barrier lane load test

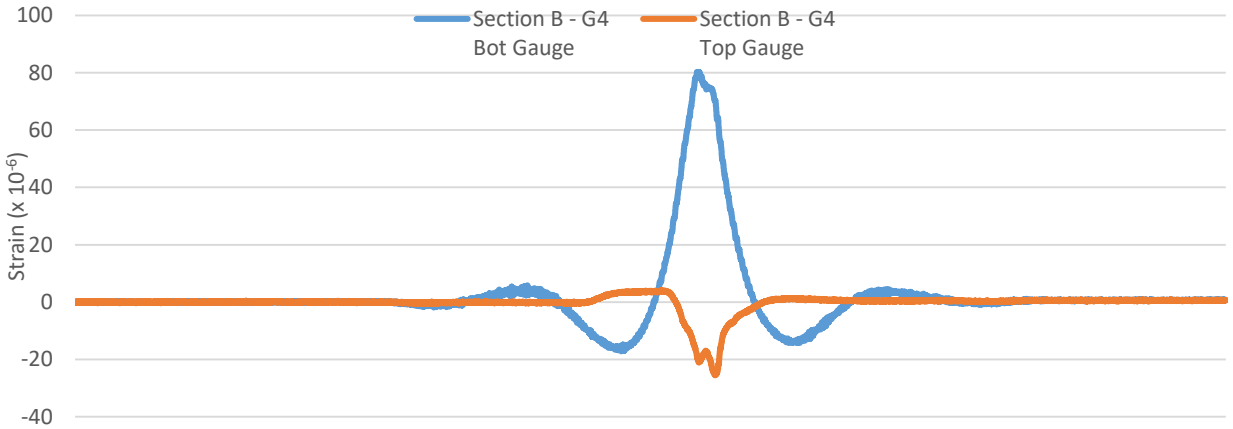

Figure C.4 - Girder 4 strain gauge response to slow northbound barrier lane load test

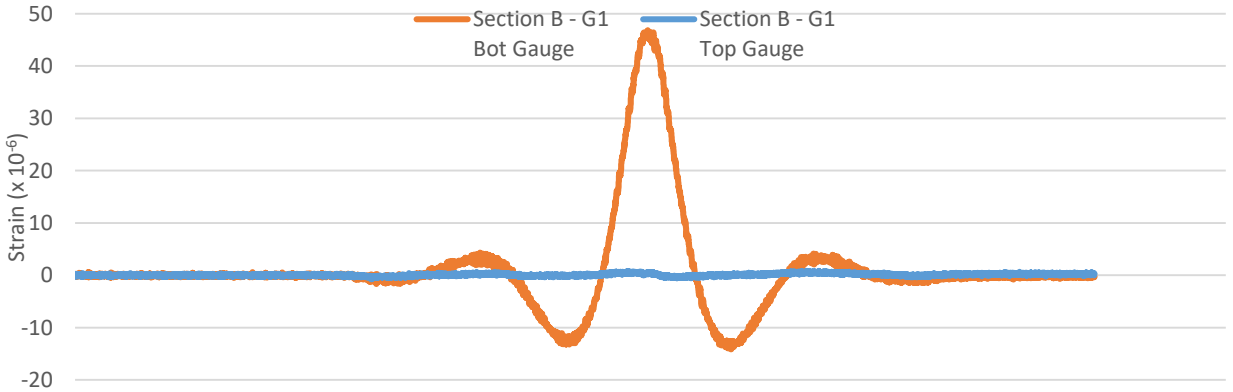

Figure C.5 - Girder 1 strain gauge response to slow southbound median lane load test

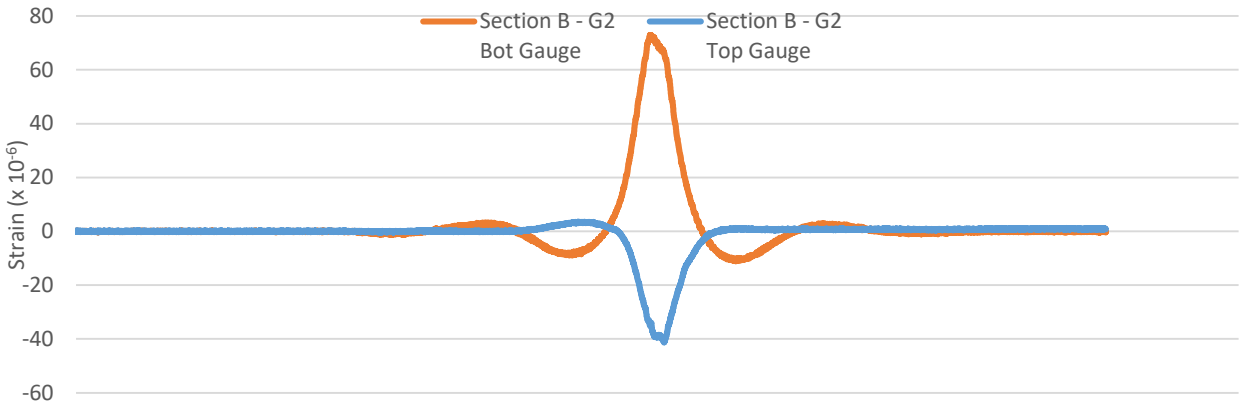

Figure C.6 - Girder 2 strain gauge response to slow southbound median lane load test

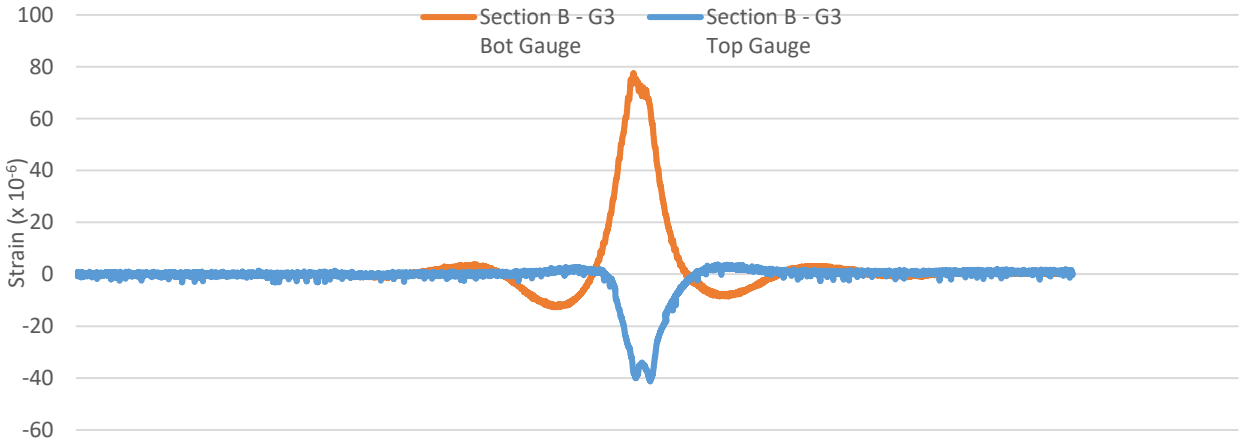

Figure C.7 - Girder 3 strain gauge response to slow northbound median lane load test

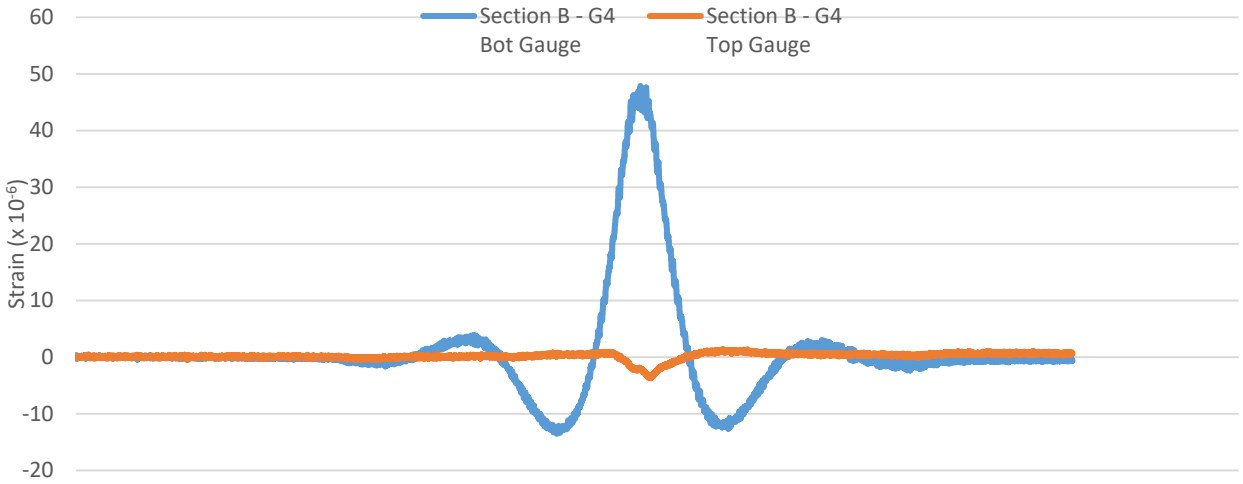

Figure C.8 - Girder 4 strain gauge response to slow northbound median lane load test

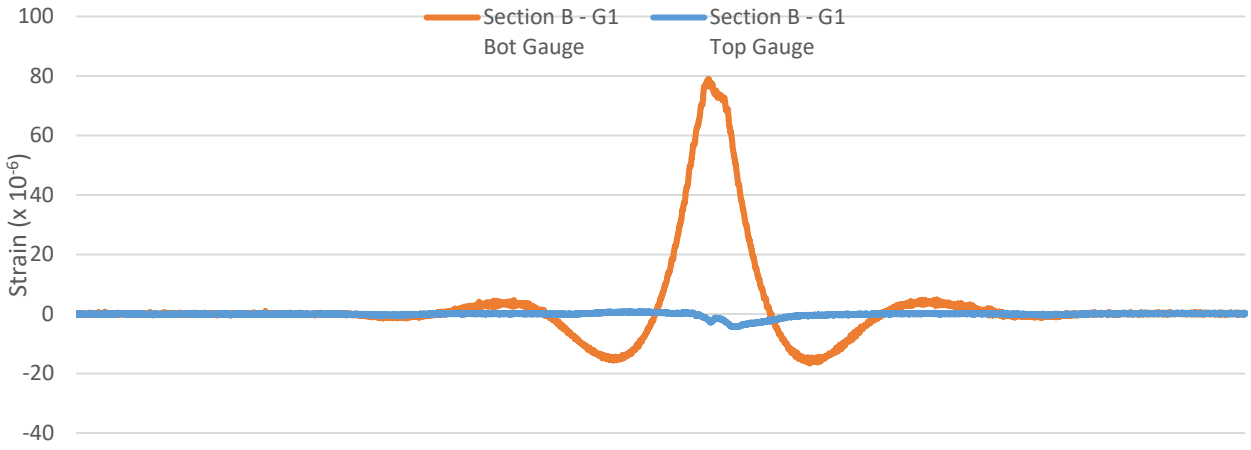

Figure C.9 - Girder 1 strain gauge response to slow southbound barrier lane load test #2

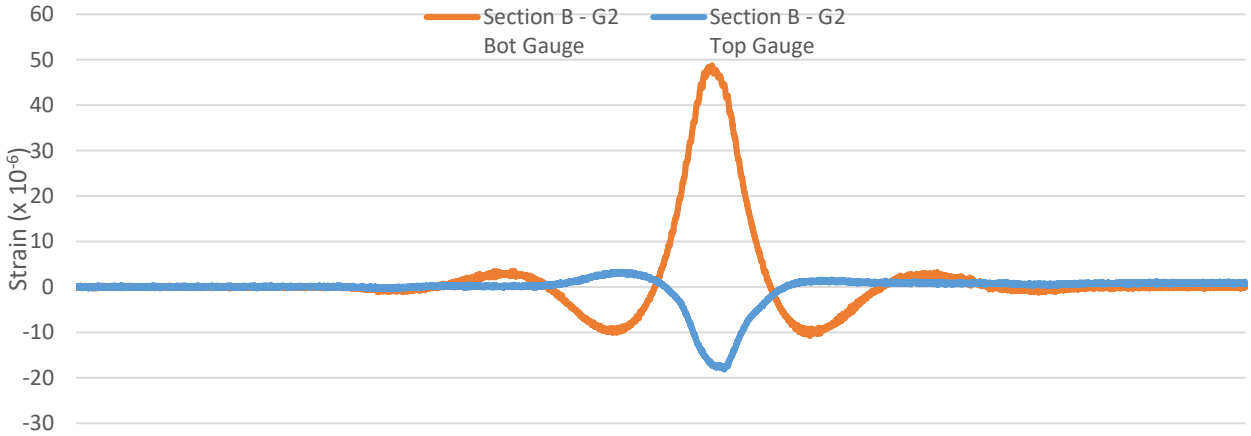

Figure C.10 - Girder 2 strain gauge response to slow southbound barrier lane load test #2

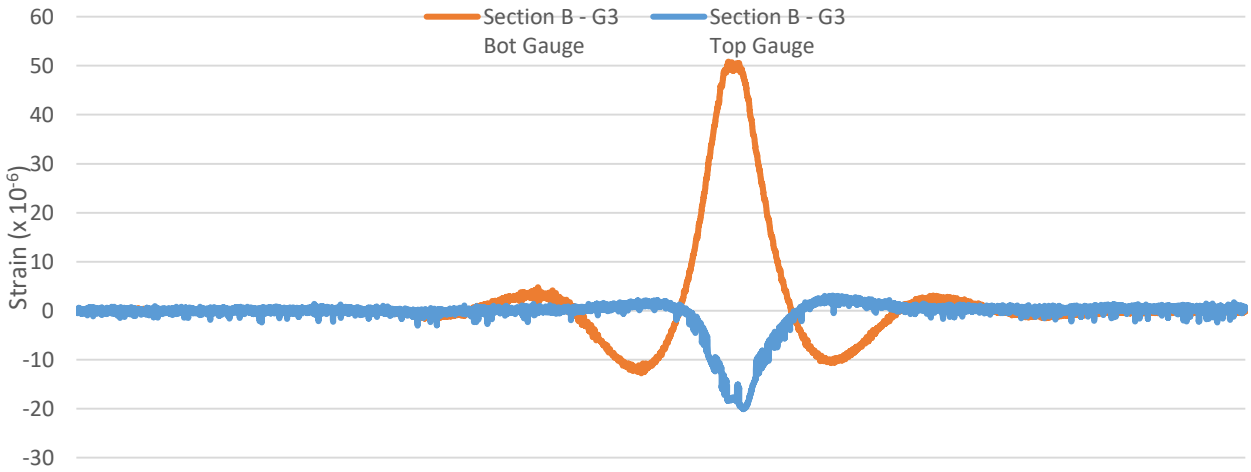

Figure C.11 - Girder 3 strain gauge response to slow northbound barrier lane load test #2

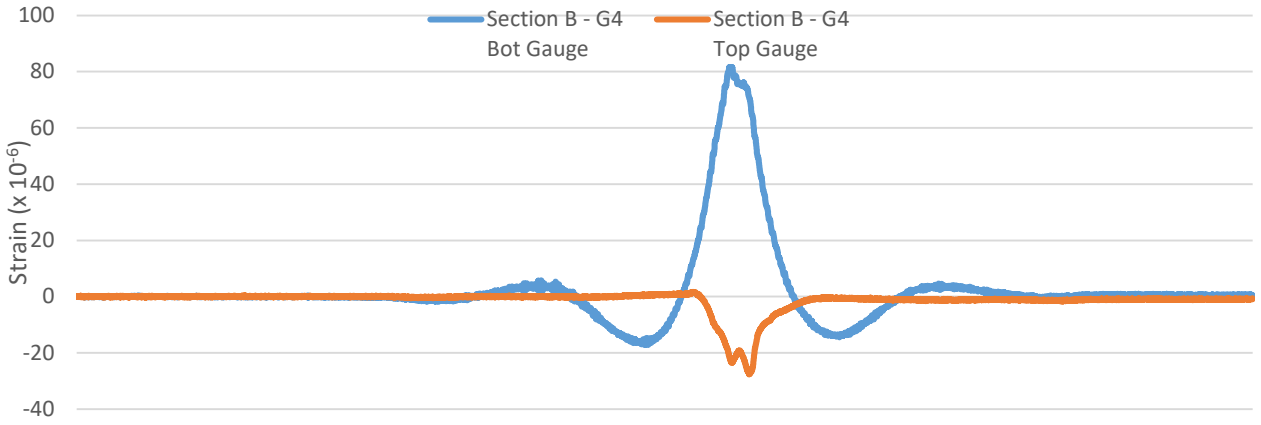

Figure C.12 - Girder 4 strain gauge response to slow northbound barrier lane load test #2

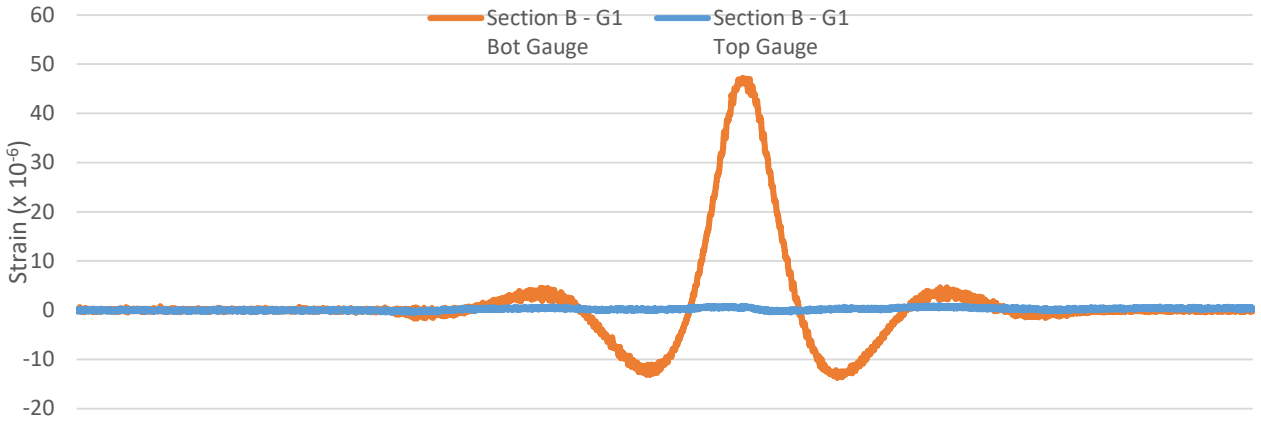

Figure C.13 - Girder 1 strain gauge response to slow southbound median lane load test #2

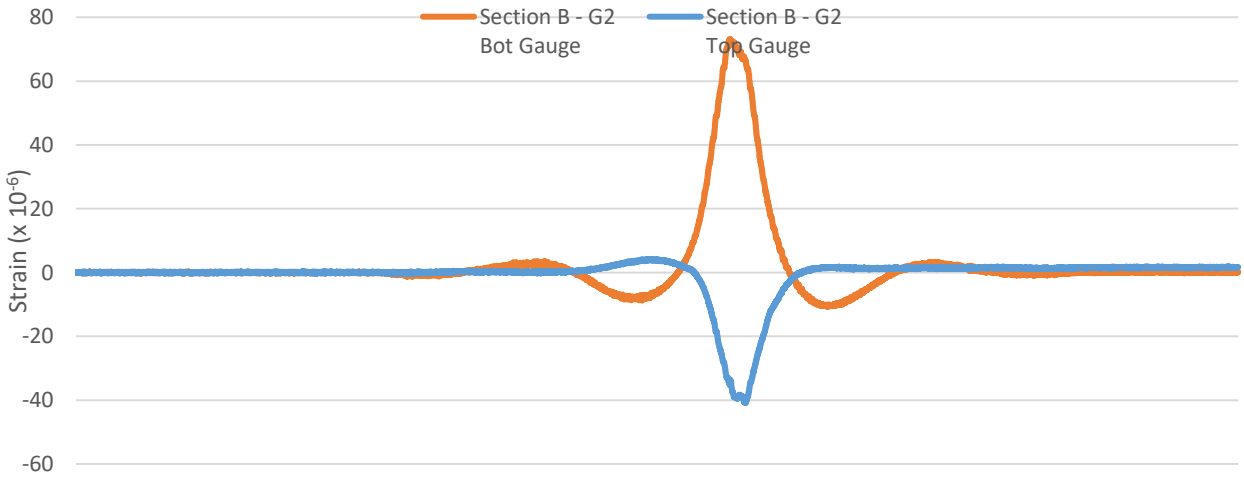

Figure C.14 - Girder 2 strain gauge response to slow southbound median lane load test #2

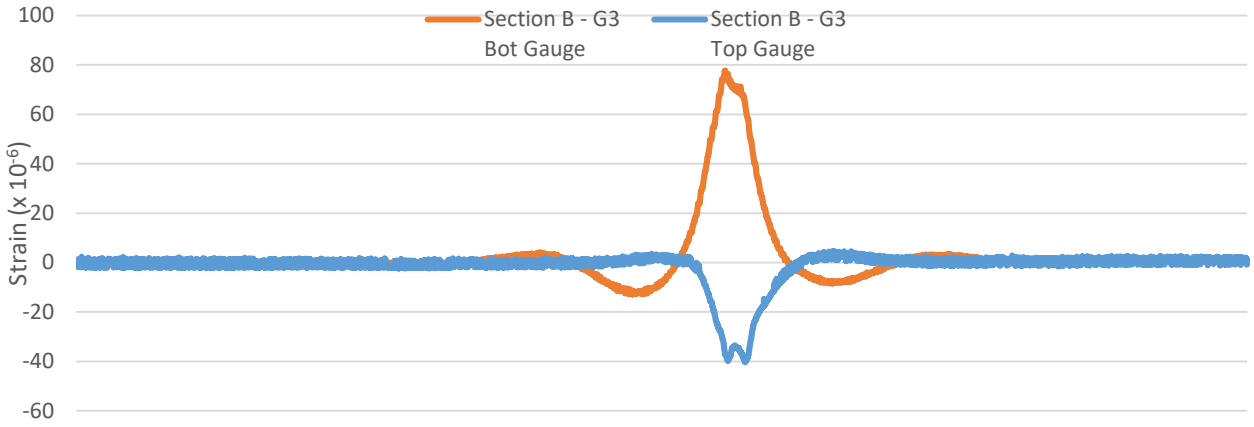

Figure C.15 - Girder 3 strain gauge response to slow northbound median lane load test #2

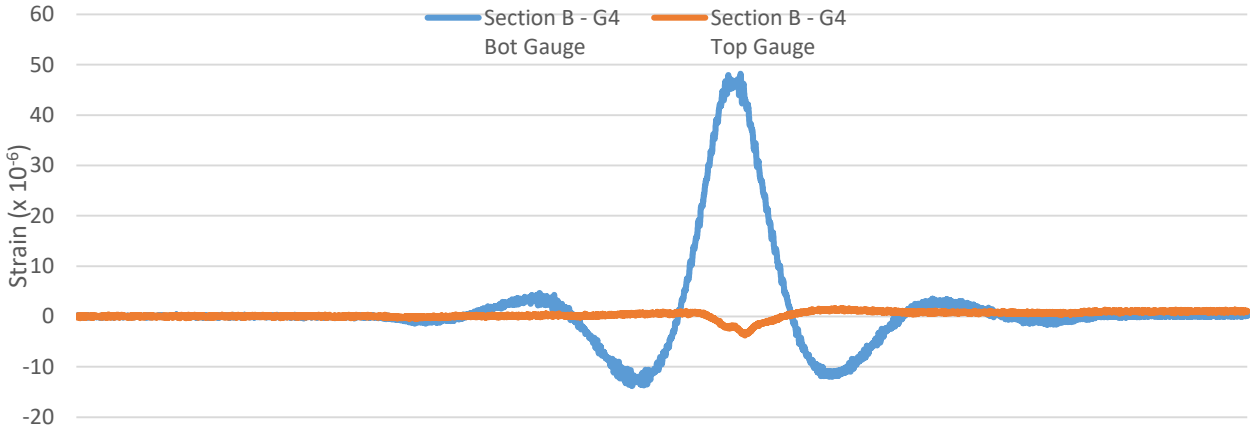

Figure C.16 - Girder 4 strain gauge response to slow northbound median lane load test #2

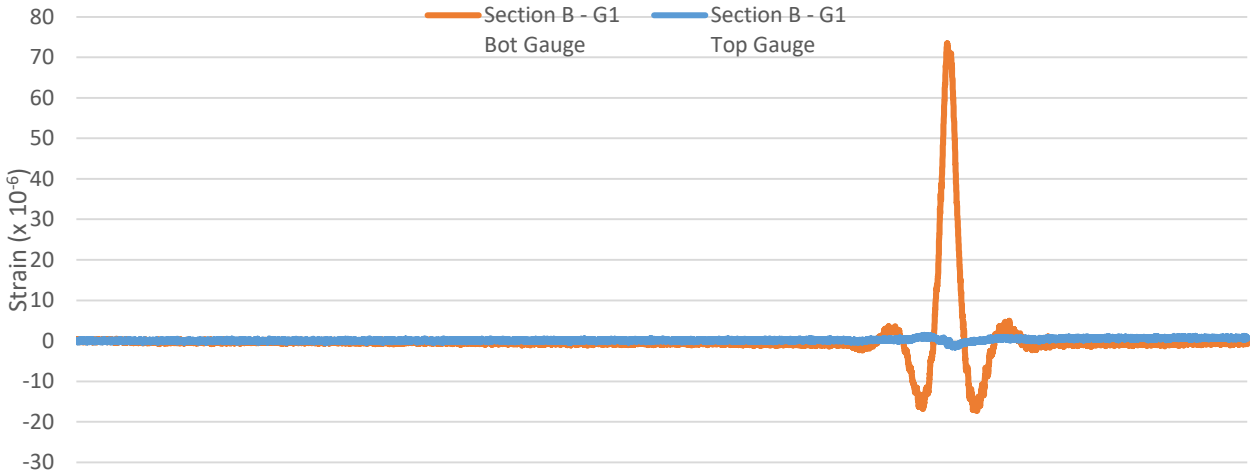

Figure C.17 - Girder 1 strain gauge response to fast southbound barrier lane load test

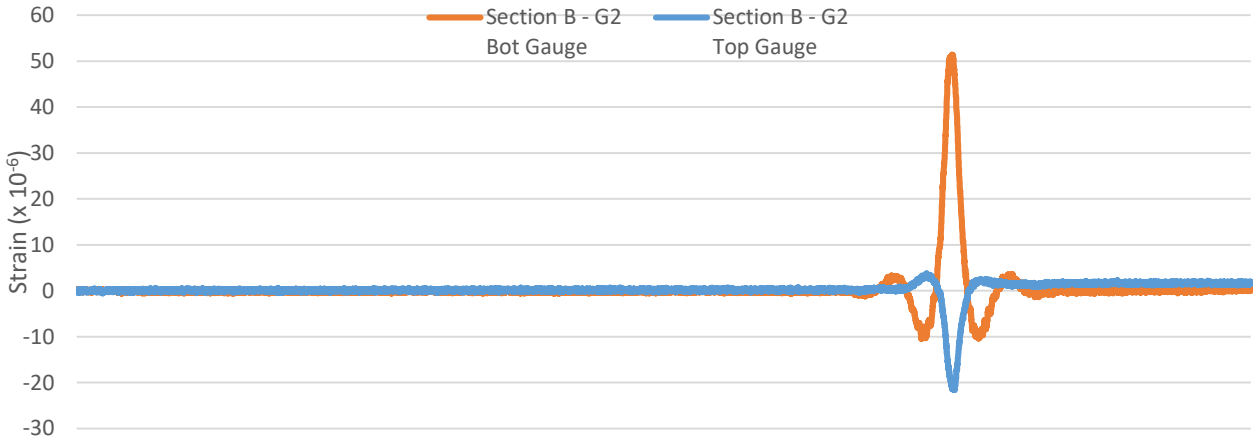

Figure C.18 - Girder 2 strain gauge response to fast southbound barrier lane load test

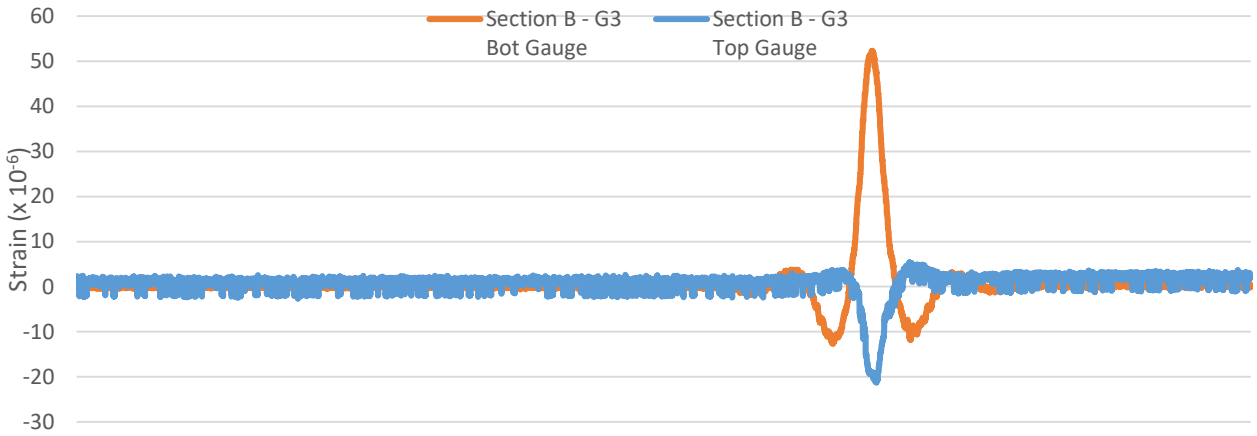

Figure C.19 - Girder 3 strain gauge response to fast northbound barrier lane load test

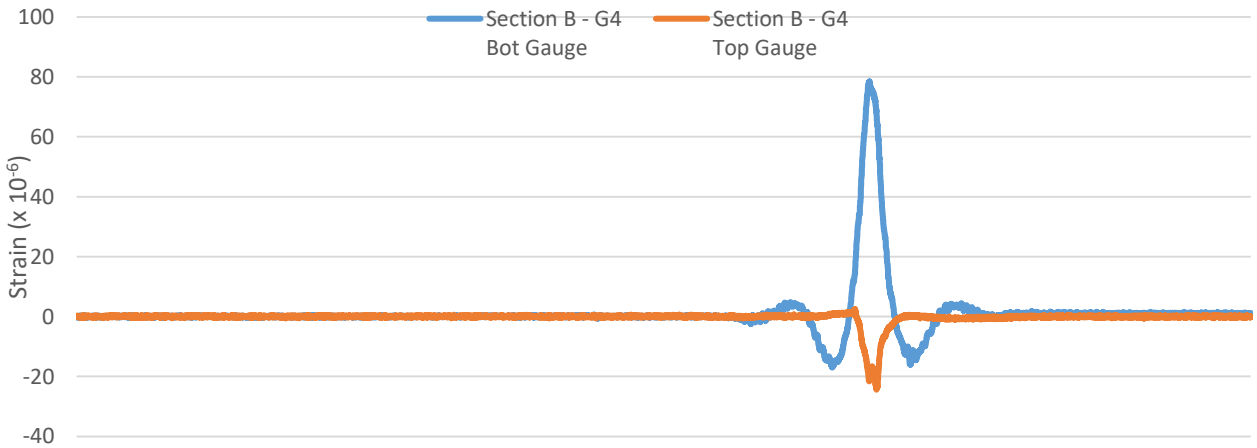

Figure C.20 - Girder 4 strain gauge response to fast northbound barrier lane load test

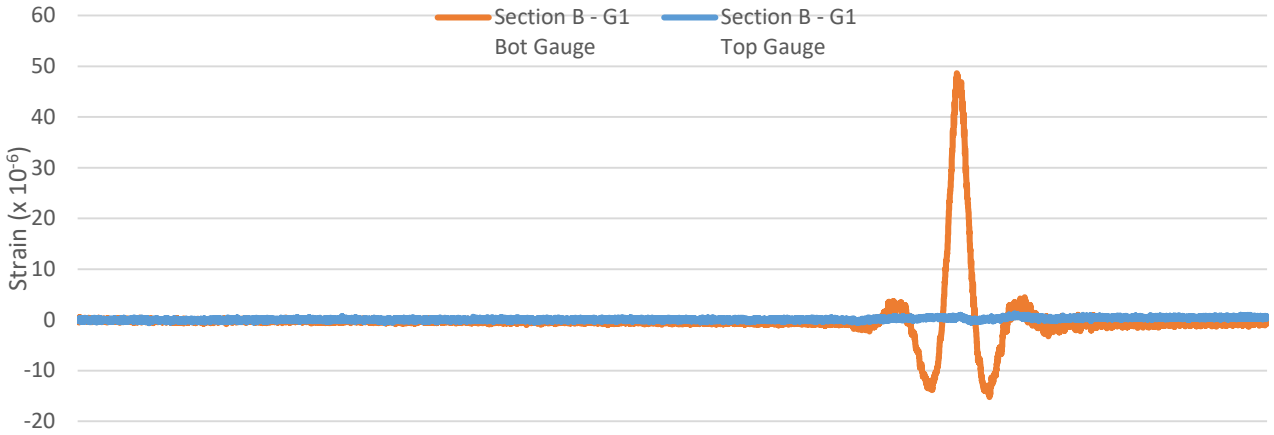

Figure C.21 - Girder 1 strain gauge response to fast southbound median lane load test

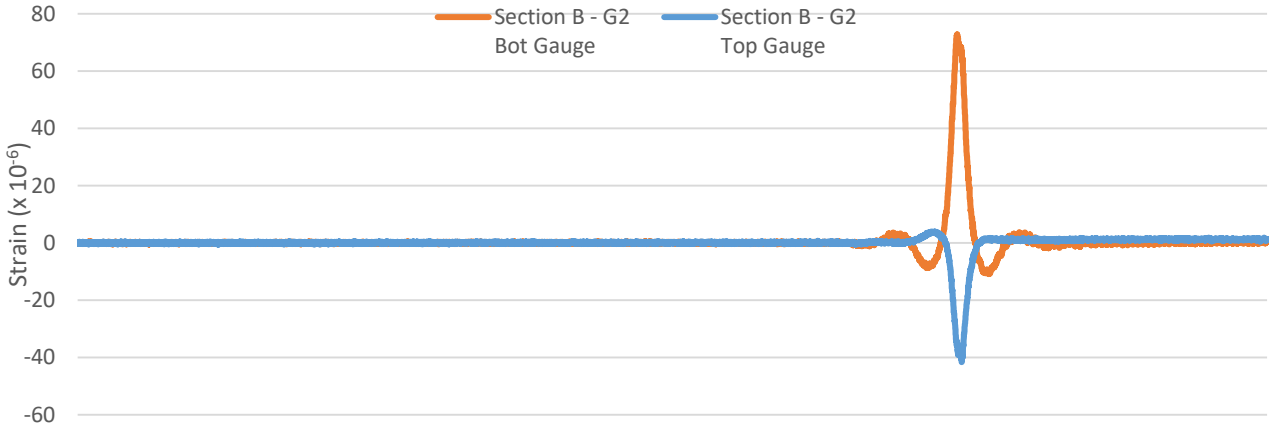

Figure C.22 - Girder 2 strain gauge response to fast southbound median lane load test

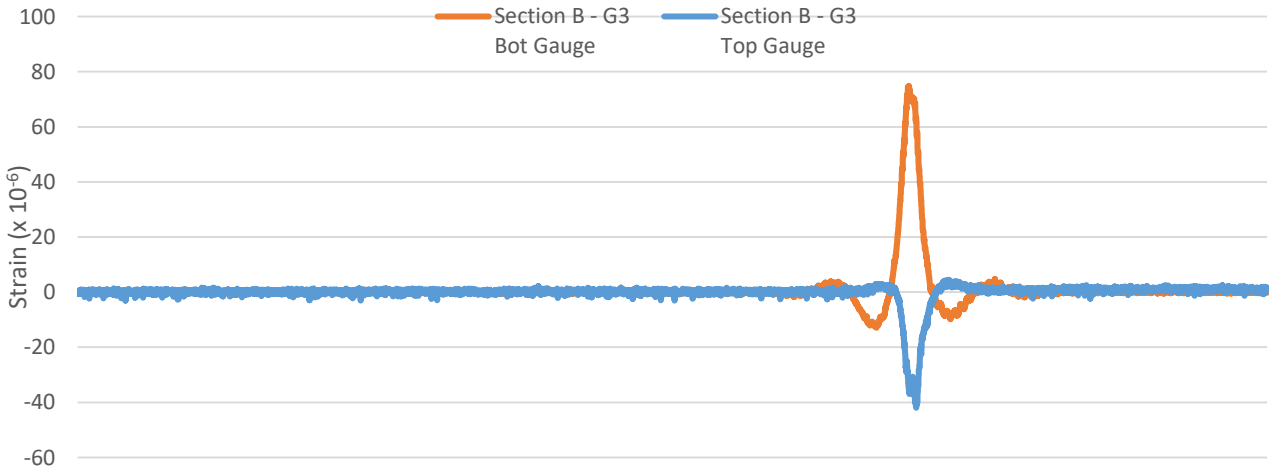

Figure C.23 - Girder 3 strain response to fast northbound median lane load test

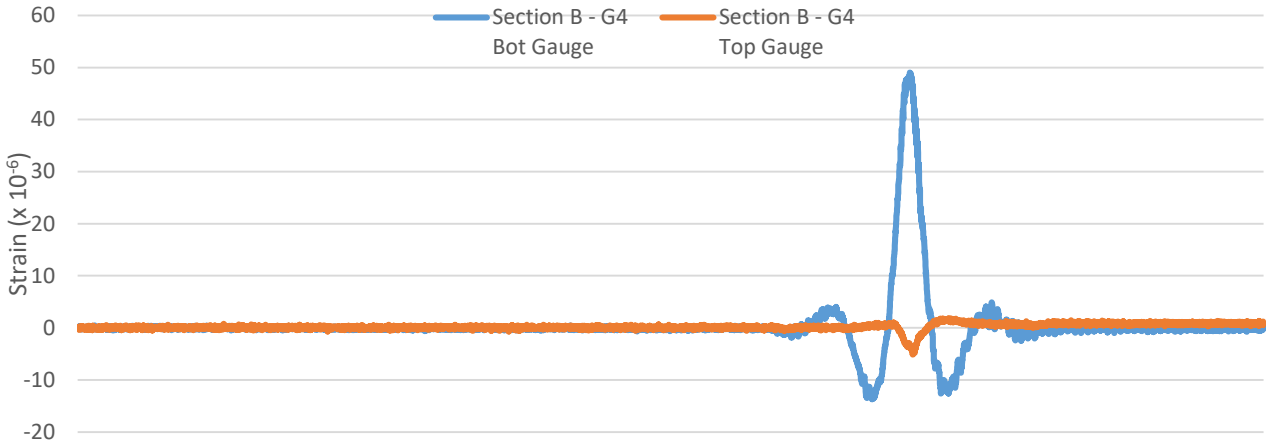

Figure C.24 - Girder 4 strain gauge response to fast northbound median lane load test

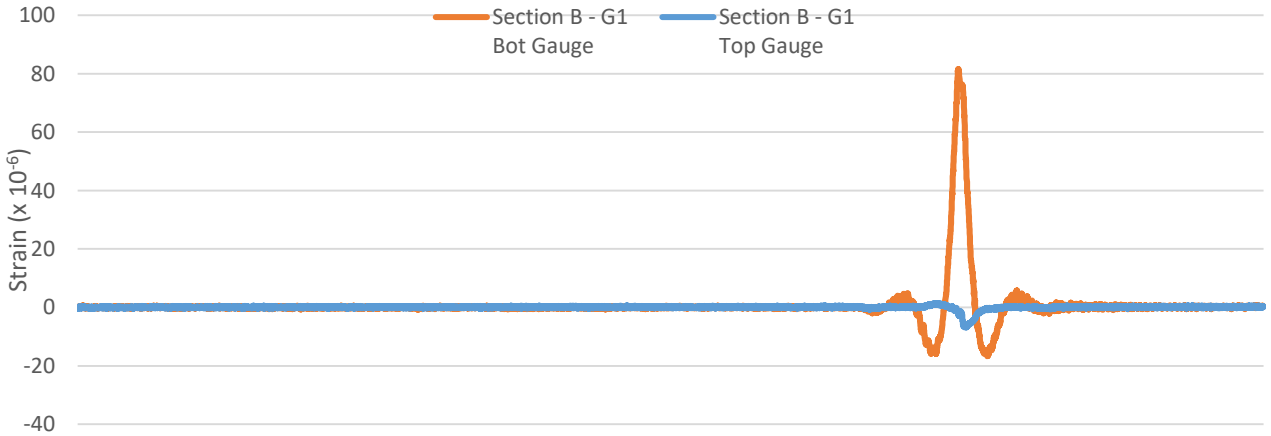

Figure C.25 - Girder 1 strain gauge response to fast southbound barrier lane load test #2

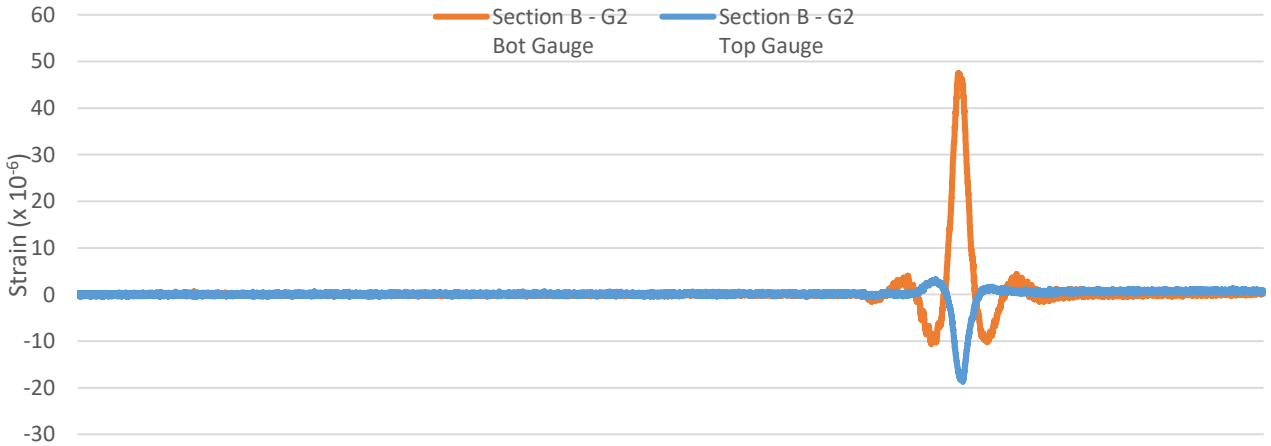

Figure C.26 - Girder 2 strain gauge response to fast southbound barrier lane load test #2

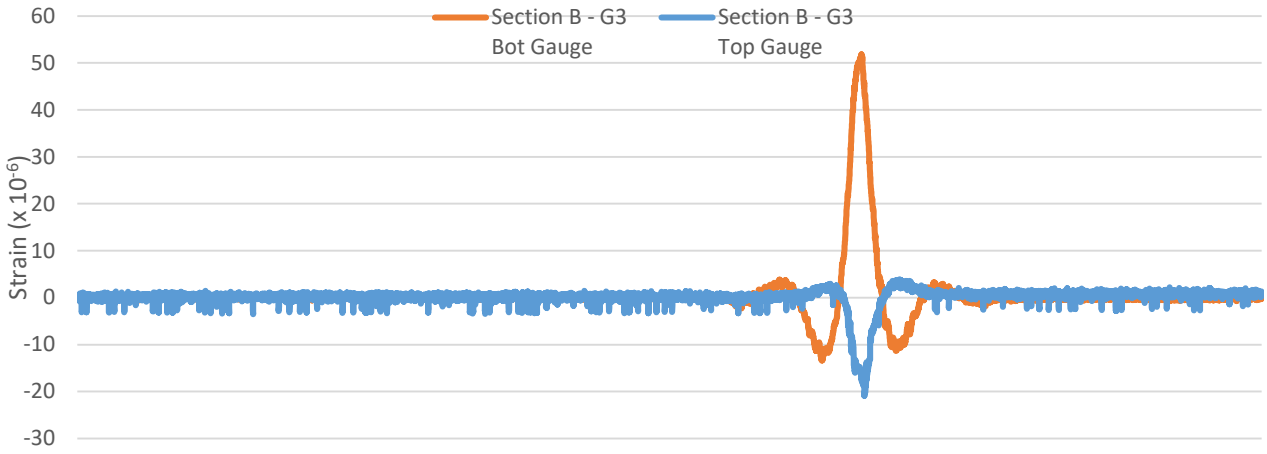

Figure C.27 - Girder 3 strain response to fast northbound barrier lane load test #2

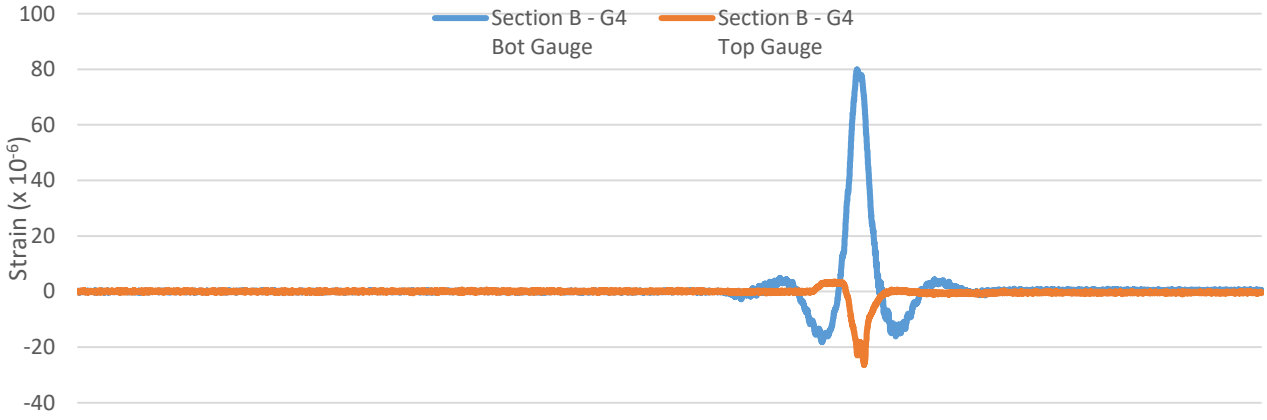

Figure C.28 - Girder 4 strain gauge response to fast northbound barrier lane load test #2

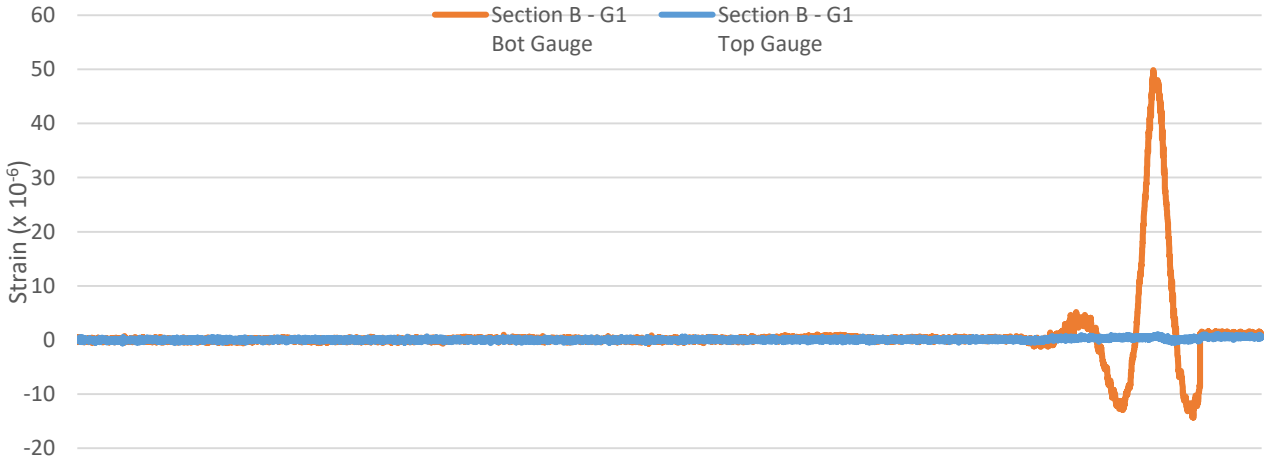

Figure C.29 - Girder 1 strain gauge response to fast southbound median lane load test #2

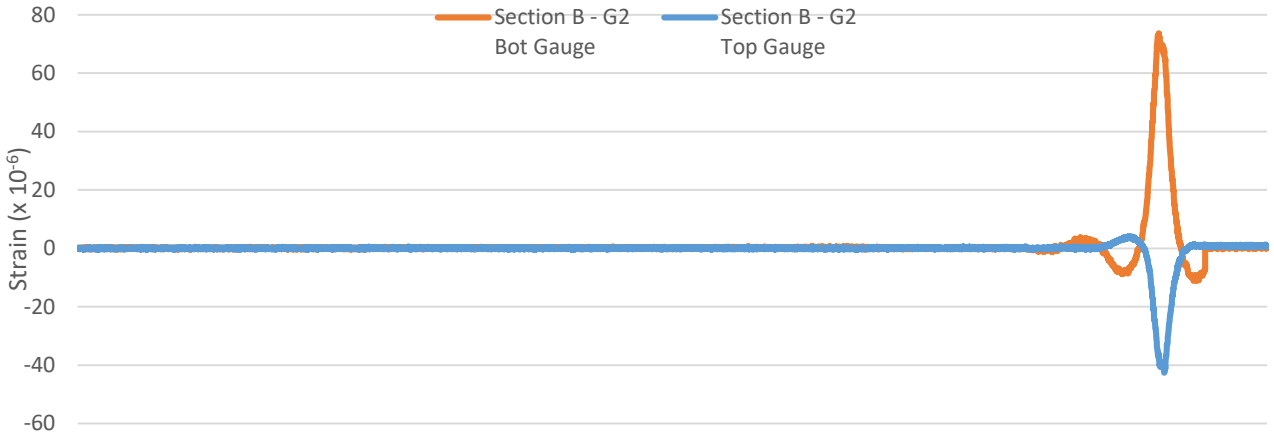

Figure C.30 - Girder 2 strain response to fast southbound median lane load test #2

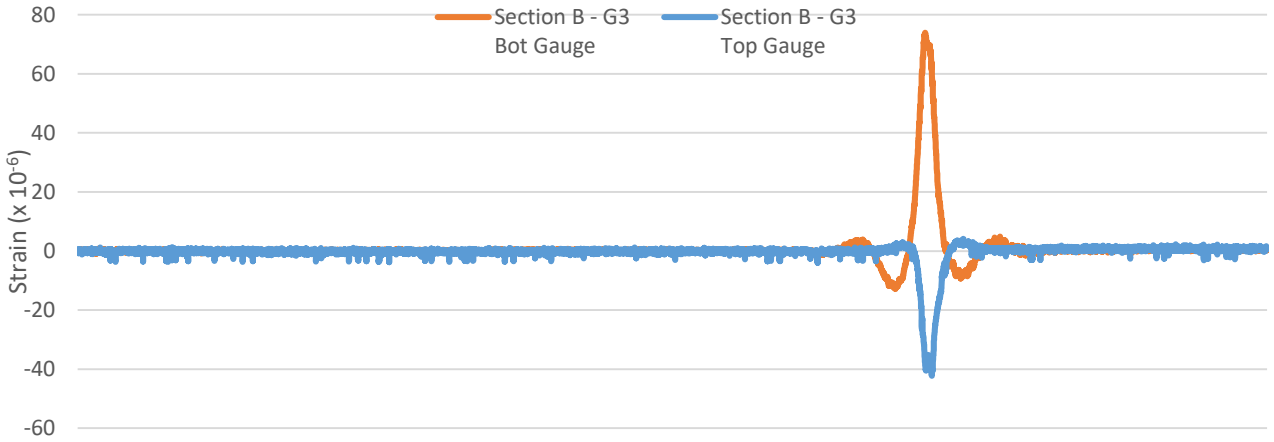

Figure C.31 - Girder 3 strain gauge response to fast northbound median lane load test #2

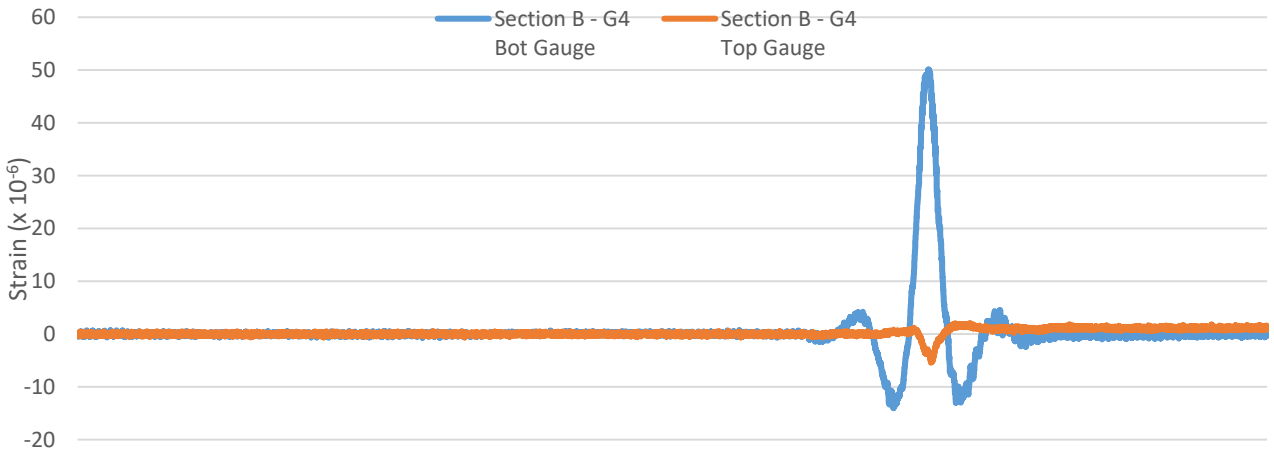

Figure C.32 - Girder 4 strain gauge response to fast northbound median lane load test #2

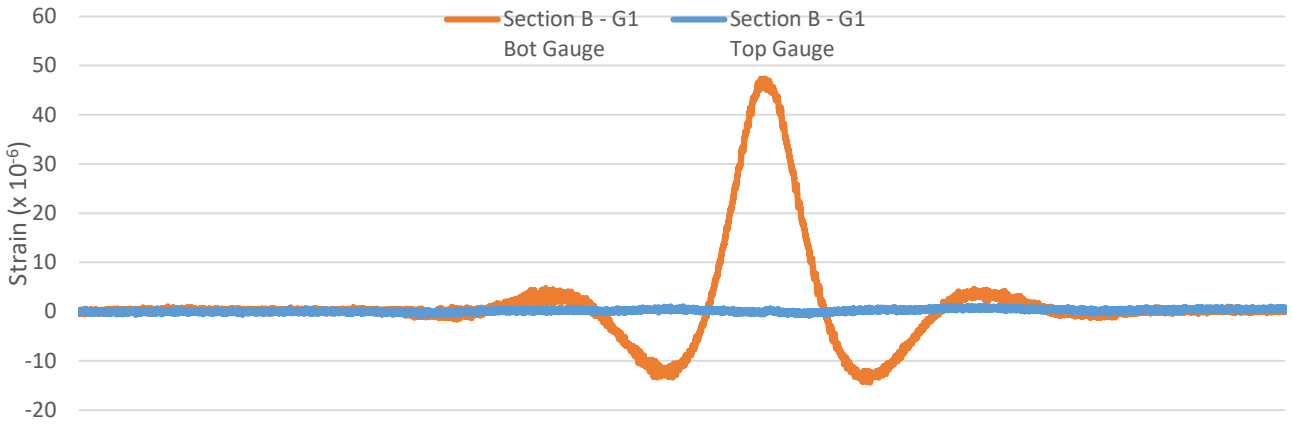

Figure C.33 - Girder 1 strain gauge response to slow southbound median lane load test #3

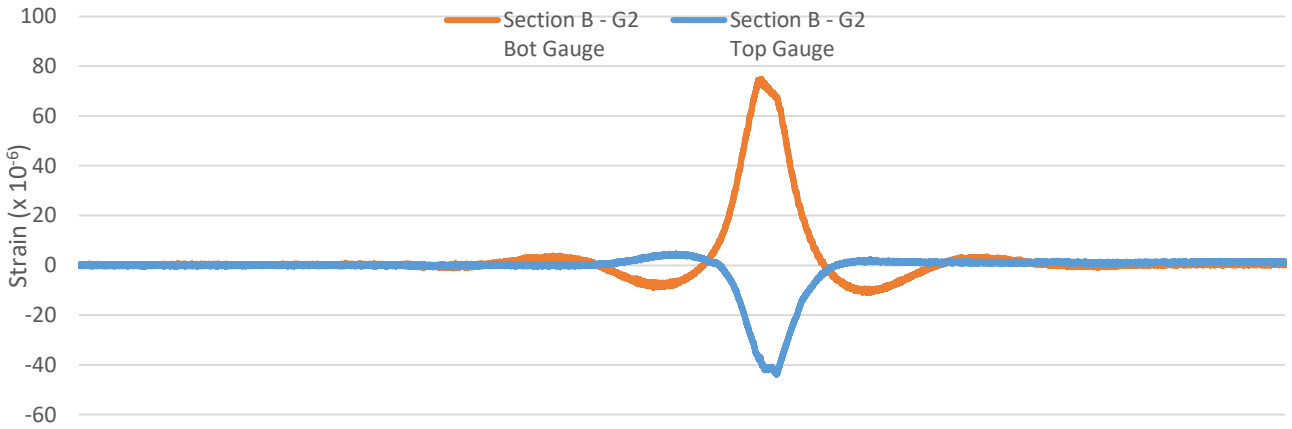

Figure C.34 - Girder 2 strain gauge response to slow southbound median lane load test #3

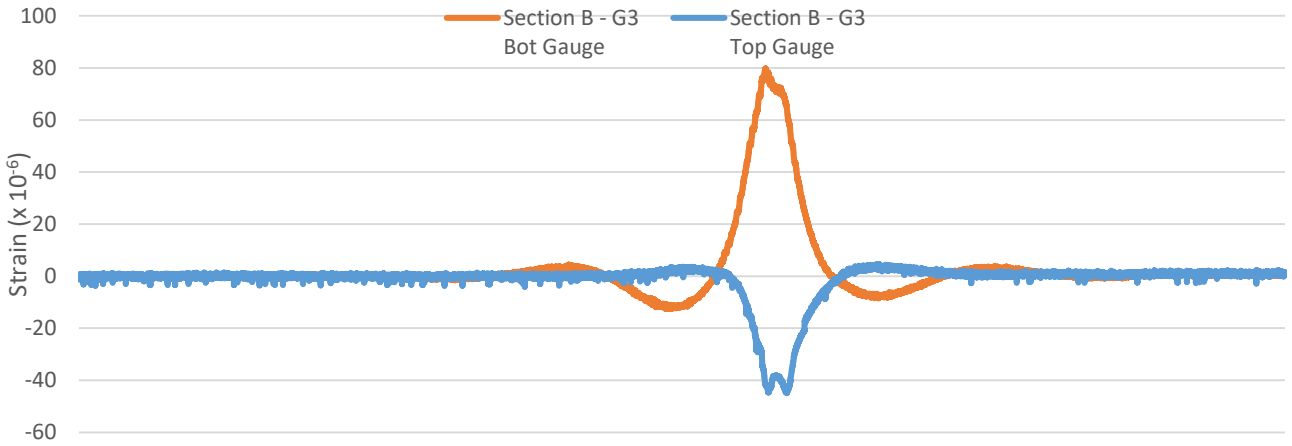

Figure C.35 - Girder 3 strain gauge response to slow northbound median lane load test #3

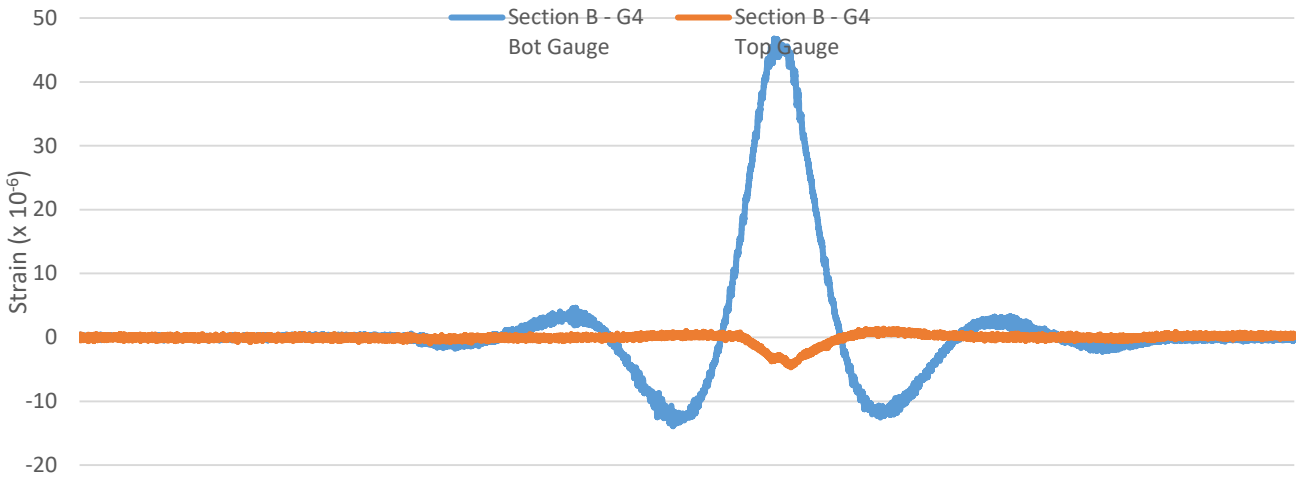

Figure C.36 - Girder 4 strain gauge response to slow northbound median lane load test #3